REPORT DOCUMENTATION PAGE

Form Approved
OMB No. 0704-0188

1. AGENCY USE ONLY (Leave blank)

2. REPORT DATE
23 January 1997

3. REPORT TYPE AND DATES COVERED
Final,

4. TITLE AND SUBTITLE
Shaped Actuators and Sensors for Local Control of Intelligent Structures

5. FUNDING NUMBERS
F49620-93-1-0537

AFOSR-TR-97
0137

6. AUTHOR(S)
Amy Jean McCain
Edward F. Crawley

7. PERFORMING ORGANIZATION NAME(S) AND ADDRESS(ES)
Department of Aeronautics and Astronautics
MIT
Cambridge, MA 02139

9. SPONSORING/MONITORING AGENCY NAME(S) AND ADDRESS(ES)
AFOSR
110 Duncan Avenue, Suite B115
Bolling AFB, DC 220332-8080

NA

10. SPONSORING/MONITORING AGENCY REPORT NUMBER
93-1-0537

11. SUPPLEMENTARY NOTES

12a. DISTRIBUTION/AVAILABILITY STATEMENT
Approved for Public Release; Distribution Unlimited

12b. DISTRIBUTION CODE

13. ABSTRACT The properties of the actuator to sensor transfer functions for various shaped strain actuator-sensor pairs on a Bernoulli-Euler beam are investigated. Analytical expressions for these transfer functions and their associated dereverberated transfer functions are derived. It is shown that the actuator-sensor pair can be designed such that its derevercerated transfer function will have a desirable corner frequency and high frequency rolloff rate.

The analytical and dereverberated transfer functions of noncollocated actuator-sensor pairs are compared to those of the collocated pairs.

Finite element models are constructed which add damping, finite actuator thickness, and finite beam and actuator widths to the model. The actuator to sensor transfer functions are calculated to these models, and the effects of the added factors are determined. It is shown that the transfer bending modes of the three dimensional beam delay the rolloff of the actuator to sensor frequency transfer function by at least two decades. Finally, experimental data confirms the results of the three dimensional finite element model.

14. SUBJECT TERMS
Actuators, collocated pairs, finite element model, rolloff characteristics, Shaped actuators, sensors, transfer functions

15. NUMBER OF PAGES
128

16. PRICE CODE

17. SECURITY CLASSIFICATION OF REPORT	18. SECURITY CLASSIFICATION OF THIS PAGE	19. SECURITY CLASSIFICATION OF ABSTRACT	20. LIMITATION OF ABSTRACT
Unclaasified	Unclassified	Unclassified	Unclassified

NSN 7540-01-280-5500

Standard Form 298 (Rev 2-89)
Prescribed by ANSI Std Z39-18

DTIC QUALITY INSPECTED 1

19970602 026

Shaped Actuators and Sensors for Local Control of Intelligent Structures

Amy Jean McCain

Edward F. Crawley

Abstract

The properties of the actuator to sensor transfer functions for various shaped strain actuator-sensor pairs on a Bernoulli-Euler beam are investigated. Analytical expressions for these transfer functions and their associated dereverberated transfer functions are derived. It is shown that the actuator-sensor pair can be designed such that its dereverberated transfer function will have a desirable corner frequency and high frequency rolloff rate.

The analytical and dereverberated transfer functions of noncollocated actuator-sensor pairs are compared to those of the collocated pairs. General rules are found which determine the frequency at which the transfer function no longer has an interlaced pole-zero pattern.

Finite element models are constructed which add damping, finite actuator thickness, and finite beam and actuator widths to the model. The actuator to sensor transfer functions are calculated for these models, and the effects of the added factors are determined. It is shown that the transverse bending modes of the three dimensional beam delay the rolloff of the actuator to sensor frequency transfer function by at least two decades. Finally, experimental data confirms the results of the three dimensional finite element model.

Table of Contents

List of Figures

List of Tables

Chapter 1

Introduction

Modern controlled structures are being designed for high performance, precise applications requiring pointing accuracy and vibration suppression. These specifications typically require control systems, which often include many sensors and actuators, to meet these performance objectives.

Aubrun [3], and Hall, et al. [12] have discussed the use of hierarchic control in flexible structures. This included a global control loop, which is a multiple input, multiple output (MIMO) system, whose transfer function includes the overall performance objective. The information in the global control loop is obtained from several single input, single output (SISO) local control loops. It is generally true that if damping can be added to the local control loop, the robustness of the global control loop will be improved.

This work focuses on the design of the strain actuator to strain sensor transfer function of the local control loop. Collocated and dual actuator-sensor pairs will produce a transfer function with an alternating pole-zero pattern and no associated phase loss. Damping can always be added to the plant transfer function with rate feedback. If rate feedback or any positive real compensator is used on the transfer function of a collocated and dual actuator-sensor pair, stability is guaranteed [5].

It is desirable to have a transfer function with good observability and controllability of the modes which need to be damped. This implies the frequency transfer function should rolloff with a slope of at least -10 dB/decade. It is also beneficial for the plant transfer function to roll off with a slope of at least -20 dB/decade above the bandwidth of damping. Then the loop transfer function will not roll up in the frequency range in which the transfer function must crossover.

Much work has been done recently to reduce the vibrations of various structures, including plates [20], two dimensional boxbeams [6], trusses [14], [15], and cylinders [13], using piezoelectric strain actuators and sensors. Nearly all of the analyses in this area improve vibration suppression by optimizing structural placement of the sensor or actuator or by improving the controller. Little work has been done regarding the distributed shape of the actuator and sensor. Clark [7] has investigated the use of distributed modal sensors on plates. Unfortunately, this type of sensor requires a sensor that is the length of the structure, and its effectiveness is limited by the fact that the sensor is shaped to match one particular mode of the structure. In 1987, Crawley and de Luis [9] showed that the rectangular piezoelectric strain actuator to point strain transfer function exhibits the undesirable property of no rolloff, limiting its usefulness. However, Andersson [1] later showed that various shaped strain sensors exhibit rolloff with no more phase lag than that of a point sensor. This leads to a study of shaped actuator used in conjunction with shaped sensors.

This work investigates the properties of the transfer functions for various shaped strain actuator-sensor pairs. The effect of the actuator and sensor shape upon the transfer function's rate and frequency of rolloff is determined. Also, the feasibility of implementing these actuator-sensor pairs for local control is examined.

The wave solution technique has been shown to lend physical insight into transfer

function equations [18]. In Chapter 2, this technique is used to derive the analytical transfer functions for various collocated shaped actuator-sensor pairs on infinite, semi-infinite, and finite Bernoulli-Euler beams. In 1985, de Luis[10] showed that the input of the rectangular actuator could be modelled as a coupled moment input at the ends of the actuator. Andersson [2] later demonstrated that output of the rectangular sensor could be modelled as the difference of the slopes at the ends of the sensor. Chapter 2 extends these arguments for the modelling of other shaped actuator-sensor pairs. The dereverberated transfer functions associated with these analytical transfer functions are then determined. This allows for an estimation of the analytical transfer function without generating the complete wave model [16].

The analysis of Chapter 3 uses the tools in Chapter 2 to investigate the effects of noncollocation upon various actuator to sensor transfer functions. Transfer function derivation examples are shown for various actuator-sensor pairs on infinite, semi-infinite, and finite Bernoulli-Euler beams.

Finally, in Chapter 4 finite element models are used to model the realistic effects of damping, finite actuator thickness, and finite beam and actuator width. Piezoceramic actuators are modelled as coupled field elements with the properties of PZT-5A, including the constitutive relations as discussed by Hagood, et.al. [11]. The finite width of the actuator and beam are placed in a finite element model to determine if the width dimension will cause significant differences from the Bernoulli-Euler beam transfer function, as suggested by Sullivan, Hubbard, and Burke [19].

Chapter 2

Analytical Models for Collocated Actuator-Sensor Pairs

This chapter focuses on transfer functions of point and shaped collocated actuator-sensor pairs on a Bernoulli-Euler beam. These are derived using wave and modal residue solutions, and an effort is made to understand the physics represented in these equations. The dereverberated behavior of the transfer functions is discussed, and the effect of the distributed actuator-sensor pairs upon the dereverberated transfer functions and the rolloff characteristics of the plant transfer function is shown. Various beam end conditions are considered and their dereverberated behaviors are compared. Finally, the implications of this knowledge upon actuator-sensor pair design are brought forth.

2.1 Modelling of Point and Shaped Actuators and Sensors

This chapter compares the rolloff characteristics for the transfer functions of point and distributed actuator-sensor pairs. The point actuator is modelled as a point

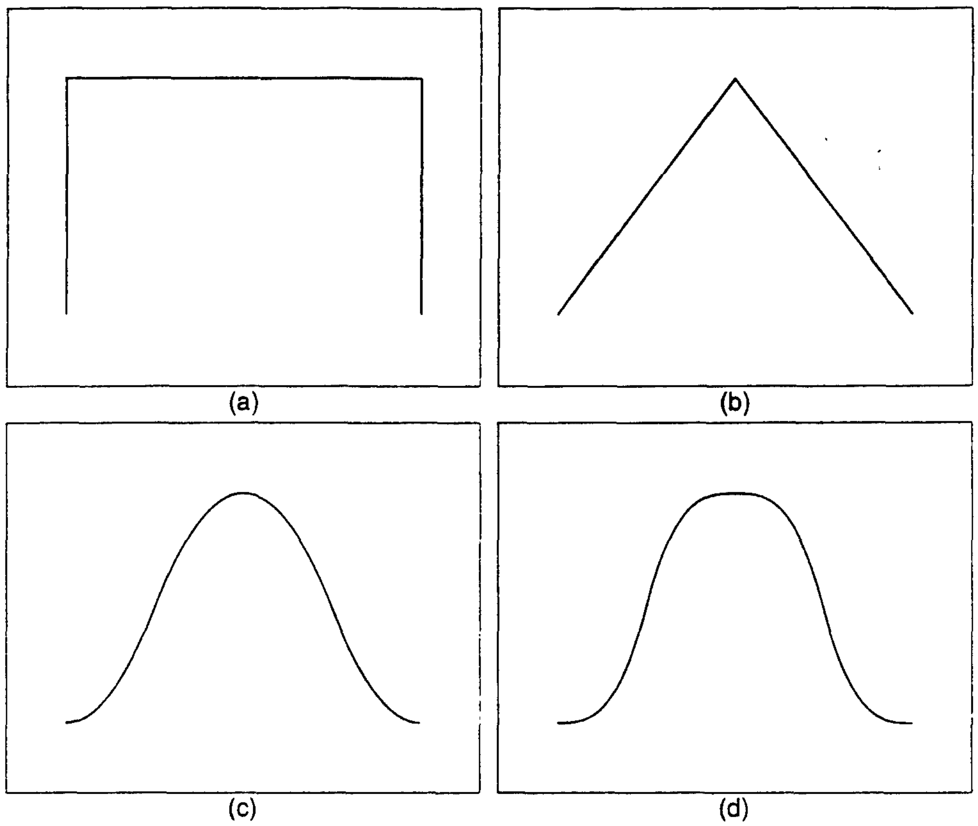

Figure 2.1: Spatial Shapes of Distributed Actuators and Sensors: (a) Rectangular, (b) Triangular, (c) Quadratic, (d) Cubic

force at the appropriate coordinate. Several different shapes of distributed actuators and sensors are modelled, including rectangular, triangular, quadratic, and cubic. A spatial representation of these shapes is shown in Figure 2.1.

Assuming the horizontal coordinate, x, is measured from the center of the actuator or sensor and l_a is the length of the actuator or sensor, the mathematical

representation for the quadratic shape function is

$$q = \begin{cases} \left(x + \frac{l_a}{2}\right)^2, & -\frac{l_a}{2} \leq x \leq -\frac{l_a}{4} \\ \frac{l_a^2}{8} - x^2, & -\frac{l_a}{4} \leq x \leq \frac{l_a}{4} \\ \left(x - \frac{l_a}{2}\right)^2, & \frac{l_a}{4} \leq x \leq \frac{l_a}{2} \end{cases} \tag{2.1}$$

The mathematical representation for the cubic shape function, under the same assumptions, is

$$c = \begin{cases} \left(x + \frac{l_a}{2}\right)^3, & -\frac{l_a}{2} \leq x \leq -\frac{l_a}{4} \\ \frac{l_a^3}{32} + x^3, & -\frac{l_a}{4} \leq x \leq 0 \\ \frac{l_a^3}{32} - x^3, & 0 \leq x \leq \frac{l_a}{4} \\ -\left(x - \frac{l_a}{2}\right)^3, & \frac{l_a}{4} \leq x \leq \frac{l_a}{2} \end{cases} \tag{2.2}$$

These distributed actuators create an internal moment in the beam which corresponds to their shape. This moment is defined by the equation

$$M_\Lambda = \int_z E(z)\Lambda(z)b(z)\, z\, dz \tag{2.3}$$

where M_Λ is the internal moment, z is the thickness of the beam, b is the width of the beam, E is the stiffness of the beam, and Λ is the actuation strain [8]. If the actuation strain, Λ, or the width of the actuator, b, are proportional to the prescribed shape, then so is the internal moment, M_Λ.

This internal moment can be modelled by force or moment inputs. The modelling of the distributed shaped actuators is shown in Figure 2.2, where l_a is the length of

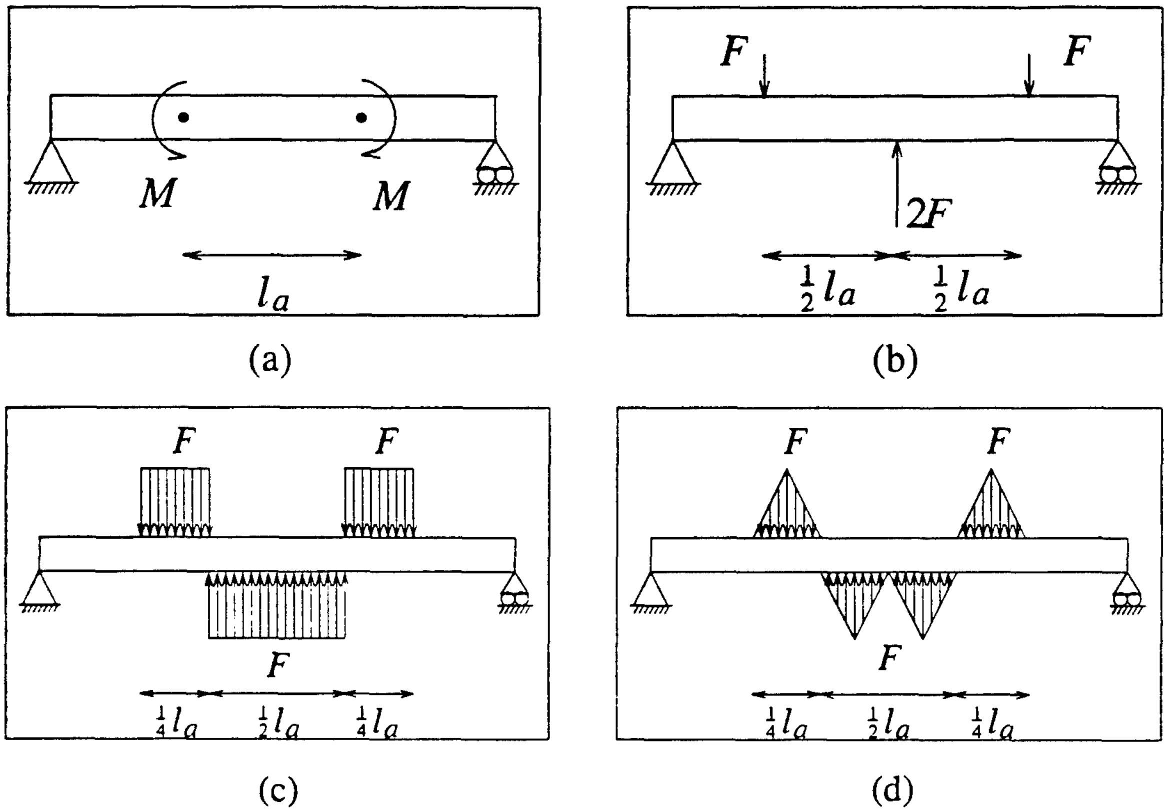

Figure 2.2: Applied Forces and Moments Modelling Distributed Actuators: (a) Rectangular, (b) Triangular, (c) Quadratic, (d) Cubic

the distributed actuators. The rectangular actuator is modelled by a coupled moment input at the geometric ends of the actuator. This is possible since the moment diagram of a beam with a coupled moment input is a rectangular shape. The triangular actuator is modelled by three forces: a force of magnitude F at the geometric ends and a force in the opposite direction of magnitude $2F$ at the geometric center of the actuator. The moment diagram of a beam with these three forces is a triangular shape, which replicates the actuator input. The quadratic and cubic actuators are modelled by the applied distributed forces shown in Figure 2.2(c) and (d). The moment diagrams of these beams shown are the quadratic and cubic shapes, respectively.

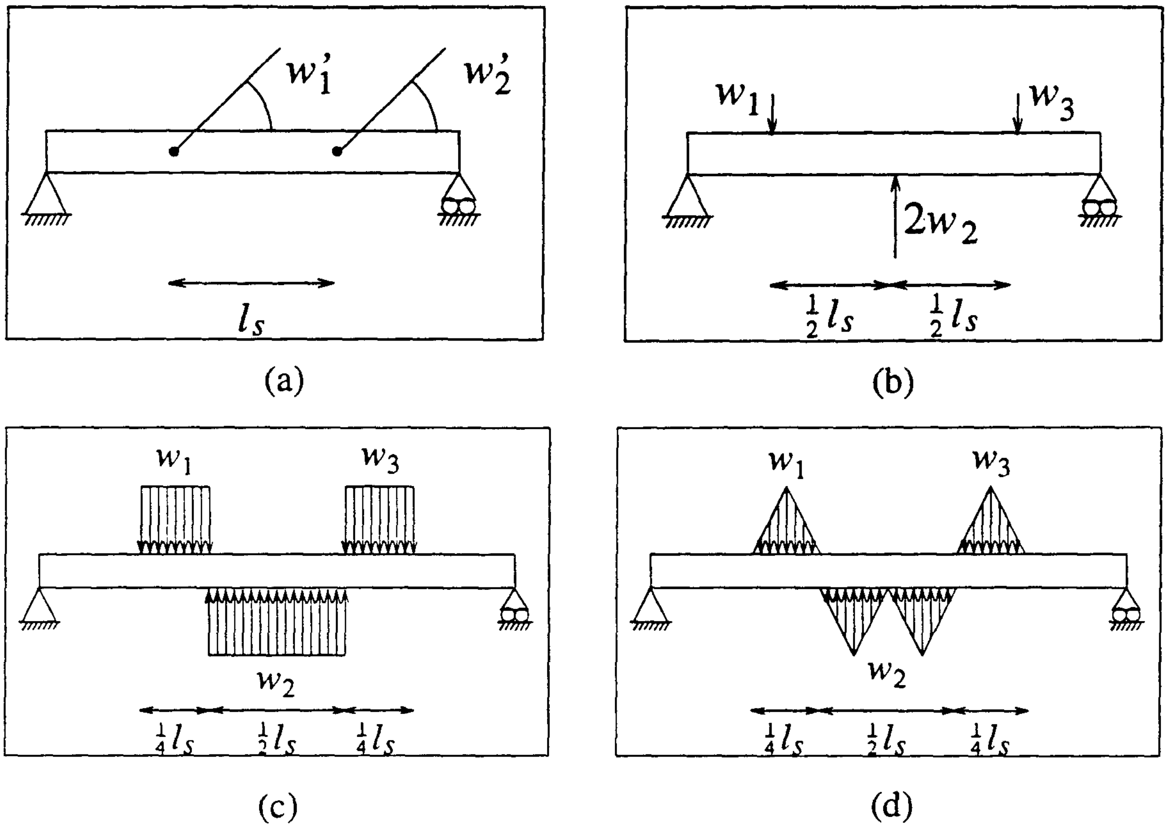

Figure 2.3: Displacement and Slope Measurements Modelling Distributed Sensors: (a) Rectangular, (b) Triangular, (c) Quadratic, (d) Cubic

These sensors measure the distributed strain of the structure, defined by the equation

$$y = \int_{-l_s/2}^{l_s/2} f(x)\epsilon(x)dx \tag{2.4}$$

where y is the sensor output, $\epsilon(x)$ is the longitudinal strain along the structure, and l_s is the length of the sensor. The weighting function $f(x)$ is implemented by varying the spatial sensitivity of the sensor [2].

The output of the sensors can be modelled by displacement or slope measurements. Each sensor is dual to its respective actuator, so the sensor measurements must be

dual to the actuator inputs. The point actuator is modelled as a force input, and a displacement measurement is dual to a force input. Therefore, the point sensor is modelled as a displacement measurement at the appropriate coordinate.

The rectangular actuator is modelled as two moment inputs applied in opposite directions. Since the slope measurement is dual to a moment input, the rectangular sensor can be modelled by two slope measurement of opposite directions, or the difference of the slope measurements at the geometric ends of the sensor. Figure 2.3 shows the modelling of the rectangular sensor and the other shaped sensors, where l_s is the length of the distributed sensors.

In the case of collocated actuator-sensor pairs, $l_s = l_a$. Since displacement is dual to force, the triangular sensor is modelled by 3 displacement measurements: the sum of the displacements at the geometric ends of the sensor minus twice the displacement at the geometric center of the sensor.

Since the quadratic and cubic sensors are dual to the quadratic and cubic actuators, they can be modelled using a sum of displacements integrated over the appropriate portion of the sensor length, i.e. a distributed displacement measurement, as in Figure 2.3(c) and (d). The equation for the quadratic sensor output, assuming the coordinate, $x = 0$, is at the center of the sensor, is

$$y_q = -\int_{-\frac{1}{2}l_s}^{-\frac{1}{4}l_s} w(x)dx + \int_{-\frac{1}{4}l_s}^{\frac{1}{4}l_s} w(x)dx - \int_{\frac{1}{4}l_s}^{\frac{1}{2}l_s} w(x)dx \tag{2.5}$$

The output of the cubic sensor is also an integrated displacement measurement as well, and is expressed as

$$\begin{aligned} y_c \; = \; & \int_{-\frac{1}{2}l_s}^{-\frac{3}{8}l_s} \frac{8}{l_s}\left(x+\frac{1}{2}l_s\right) w(x)dx - \int_{-\frac{3}{8}l_s}^{-\frac{1}{8}l_s} \frac{8}{l_s}\left(x+\frac{1}{4}l_s\right) w(x)dx + \int_{-\frac{1}{8}l_s}^{0} \frac{8x}{l_s}\, w(x)dx \\ - \; & \int_{0}^{\frac{1}{8}l_s} \frac{8x}{l_s}\, w(x)dx + \int_{\frac{1}{8}l_s}^{\frac{3}{8}l_s} \frac{8}{l_s}\left(x-\frac{1}{4}l_s\right) w(x)dx - \int_{\frac{3}{8}l_s}^{\frac{1}{2}l_s} \frac{8}{l_s}\left(x-\frac{1}{2}l_s\right) w(x)dx \quad (2.6) \end{aligned}$$

2.2 Wave Solution for Simple Transfer Functions

In order to obtain insight into the physical significance of the actuator to sensor transfer functions, a few mathematically simple examples are solved. First, these include a point force actuator-sensor pair on an infinite, semi-infinite, and finite free-free beam, as well as a moment actuator-sensor pair on an infinite, semi-infinite, and finite free-free beam. The free-free end conditions are chosen for their similarity to the infinite and semi-infinite beams. To obtain an understanding of the effects of a distributed and shaped actuator-sensor pair, a rectangular actuator-sensor pair on an infinite beam and a triangular actuator-sensor pair on an infinite beam are also considered.

To determine the analytical form of the transfer functions for point and shaped collocated actuator-sensor pairs on a Bernoulli-Euler beam, the partial differential equation for a beam is solved

$$EIw''''(x,t) + m\ddot{w}(x,t) = f(x,t) \tag{2.7}$$

where $w(x,t)$ is the displacement of the beam, EI is constant flexural stiffness, m is constant mass per unit length, and $f(x,t)$ is a forcing function.

Assuming a sinusoidal input, the wave solution is of the form

$$\begin{aligned} w(x,t) = {} & A_1 \sin(\omega t - kx) + B_1 \cos(\omega t - kx) + C_1 e^{-kx} \sin(\omega t) + D_1 e^{-kx} \cos(\omega t) \\ & + A_2 \sin(\omega t + kx) + B_2 \cos(\omega t + kx) + C_2 e^{kx} \sin(\omega t) + D_2 e^{kx} \cos(\omega t) \quad (2.8) \end{aligned}$$

where ω is the forcing frequency, and k is the wavenumber where $k^4 = \frac{m\omega^2}{EI}$ [17]. The $\sin(kx)$ and $\cos(kx)$ terms represent the spatial leftward travelling waves, and the $\sin(-kx)$ and $\cos(-kx)$ terms represent the spatial rightward travelling waves. The e^{kx} terms represent the spatial leftward evanescent waves, and the e^{-kx} terms represent the spatial rightward evanescent waves.

2.2.1 Point Actuator and Sensor

The behavior of a point actuator-sensor pair on an infinite, semi-infinite, and finite free-free beam is determined. A point force and a point displacement measurement are used to model the point actuator-sensor pair; Figure 2.4 shows these three cases. The forcing function $F(x,t)$ is assumed to be of the form $f_0 \sin(\omega t)$. Also, $F = u_p$, where u_p is the input of the point actuator. The beam is broken into two at the point of actuation, as in Figure 2.5, and the boundary conditions are matched at that point.

$$w(0^+,t) = w(0^-,t) \quad (2.9)$$

$$w'(0^+,t) = w'(0^-,t) \quad (2.10)$$

$$w''(0^+,t) = w''(0^-,t) \quad (2.11)$$

$$w'''(0^+,t) = w('''0^-,t) - \frac{F}{EI} \quad (2.12)$$

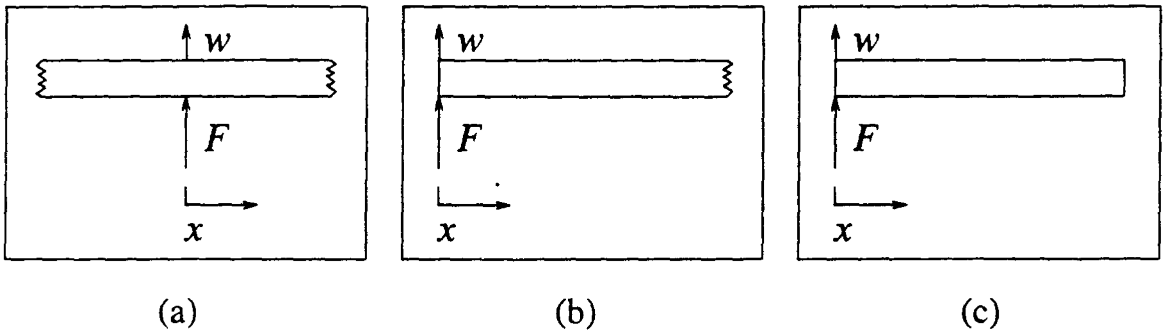

Figure 2.4: Point Actuator-Sensor Pairs on (a) Infinite, (b) Semi-infinite (c) Finite Beam

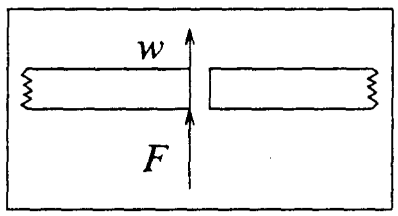

Figure 2.5: Infinite Beam Broken into Two Beams at the Point of Actuation

The appropriate end conditions are set and a harmonic balance is performed for each portion of the beam. These equations are then solved and the force to displacement transfer function is determined.

The displacement of the infinite beam is

$$w_i(x,t) = \begin{cases} \frac{f_0}{4EIk^3}\left[\cos(\omega t + kx) + e^{kx}\sin(\omega t)\right], & x \le 0 \\ -\frac{f_0}{4EIk^3}\left[\cos(\omega t - kx) + e^{-kx}\sin(\omega t)\right], & x \ge 0 \end{cases} \tag{2.13}$$

The slope and curvature at any point on the beam can be found by simply taking the appropriate number of derivatives of Equation 2.13.

The sensor output for the infinite case is

$$y_{pi} = w(0,t)$$

$$y_{\mathrm{pi}} = \frac{f_0}{4EIk^3}\left[\cos(\omega t) + \sin(\omega t)\right] \tag{2.14}$$

where y_{pi} is the output of a point sensor on an infinite beam.

The transfer function of this actuator-sensor pair is defined as

$$\begin{aligned} \frac{y_{\mathrm{pi}}}{u_{\mathrm{p}}} &= \frac{w(0,t)}{F} \\ \frac{y_{\mathrm{pi}}}{u_{\mathrm{p}}} &= \frac{\cos(\omega t) + \sin(\omega t)}{4EIk^3 \sin(\omega t)} \end{aligned} \tag{2.15}$$

Since no end conditions exist on the infinite beam, the transfer function can have phase other than 0° or 180°. The transfer function of a collocated actuator to sensor on a finite beam only has phase of 0° or 180°.

The magnitude of Equation 2.15 can be found by simplifying

$$\begin{aligned} \cos(\omega t) + \sin(\omega t) &= A\sin(\omega t + \phi) \\ &= A(\sin(\omega t)\cos(\phi) + \cos(\omega t)\sin(\phi)) \end{aligned}$$

Performing a harmonic balance

$$\begin{aligned} A\cos(\phi) &= 1 \\ A\sin(\phi) &= 1 \\ \phi &= 45^\circ, 225^\circ \\ A &= \sqrt{2}, -\sqrt{2} \end{aligned}$$

Therefore, the transfer function magnitude is

$$\left|\frac{y_{\mathrm{pi}}}{u_{\mathrm{p}}}\right| = \frac{\sqrt{2}}{4EIk^3} \tag{2.16}$$

While the magnitude and phase of the transfer function can be calculated, it is apparent that more physical insights come from the sensor output, Equation 2.14. Therefore, for infinite and semi-infinite cases, only the sensor output will be evaluated.

The infinite beam has the simplest solution due to its innate symmetry and the lack of reflecting waves. The sensor output clearly shows no delays due to the propagation of travelling waves and no decay in the response due to evanescent waves at the coordinate of the collocated actuator-sensor pair. From Equation 2.14 and Equation 2.16, it is apparent that the transfer function has a slope of k^{-3} at all frequencies.

The sensor output for the semi-infinite beam in Figure 2.4(a) can be derived as in the case of the infinite beam. This output is

$$\begin{aligned} y_{\mathrm{ps}} &= w(0,t) \\ y_{\mathrm{ps}} &= -\frac{f_0}{EIk^3}\left[\sin(\omega t) + \cos(\omega t)\right] \end{aligned} \tag{2.17}$$

where y_{ps} is the output of a point sensor on a semi-infinite beam.

Since the input of the semi-infinite beam is at the left (finite) end, evanescent and travelling waves emanate only from the left end, and no reflecting waves exist. Equation 2.17 is proportional to the output of the infinite beam sensor, Equation 2.14, and again there are no artifacts of any spatial waves in the sensor output.

The actuator to sensor transfer function for the finite beam is

$$\begin{aligned}\frac{y_{\mathrm{pf}}}{u_{\mathrm{p}}} &= \frac{w(0,t)}{F}\\ \frac{y_{\mathrm{pf}}}{u_{\mathrm{p}}} &= -\frac{e^{kl}(\sin(kl)-\cos(kl))+e^{-kl}(\sin(kl)+\cos(kl))}{EIk^3[\cos(kl)(e^{kl}+e^{-kl})-2]}\end{aligned} \tag{2.18}$$

where y_{pf} is the output of a point sensor on a finite beam, and l is the beam length.

The finite beam has a more complicated solution because the beam reflects waves at both ends. Since the length is finite, there are no time dependent terms and the effect of travelling waves and evanescent waves is understood directly from the transfer function. The explicit k^{-3} in Equation 2.18 determines the slope of the high frequency transfer function.

2.2.2 Moment Actuator and Slope Sensor

Here, the behavior for a moment actuator and slope sensor pair on an infinite, semi-infinite, and finite free-free beam is determined. The free-free end conditions are chosen for the finite beam due to the similarity of the modeshapes to the displacement profiles of the infinite and semi-infinite beams. A moment input and slope measurement are used to model the moment actuator-sensor pair. The three cases are shown in Figure 2.6. The forcing function $M(x,t)$ is assumed to be of the form $m_0\sin(\omega t)$. Also, $M = u_{\mathrm{m}}$, where u_{m} is the input of the moment actuator. The sensor output for the infinite and semi-infinite cases and the actuator-sensor transfer function for the finite case are determined in the same manner as for the point actuator-sensor pair.

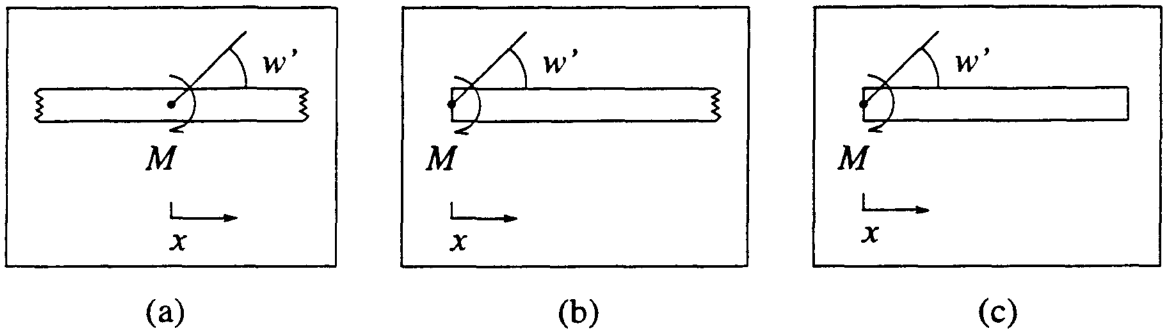

Figure 2.6: Moment Actuator and Slope Sensor on (a) Infinite, (b) Semi-infinite, (c) Finite beam

The displacement of the infinite beam due to the moment actuator is

$$w(x,t) = \begin{cases} \frac{m_0}{4EIk^2}\left[\sin(\omega t + kx) - e^{kx}\sin(\omega t)\right], & x \leq 0 \\ \frac{m_0}{4EIk^2}\left[-\sin(\omega t - kx) + e^{-kx}\sin(\omega t)\right], & x \geq 0 \end{cases} \tag{2.19}$$

Taking the derivative to determine the slope, the sensor output for the infinite beam case is

$$\begin{aligned} y_{\text{mi}} &= w'(0,t) \\ y_{\text{mi}} &= \frac{m_0}{4EIk}\left[-\cos(\omega t) + \sin(\omega t)\right] \end{aligned} \tag{2.20}$$

where y_{mi} is the sensor output due to the moment input on an infinite beam.

Again, the infinite beam has the simplest solution due to symmetry and the lack of reflecting waves. The sensor output again shows influence from the travelling waves or evanescent waves at the actuator-sensor coordinate, and it explicitly shows the rolloff is proportional to k^{-1}.

The sensor output, i.e. slope, for the semi-infinite beam:

$$
\begin{aligned}
y_{\mathrm{ms}} &= w'(0,t) \\
y_{\mathrm{ms}} &= \frac{m_0}{EIk}\left[\cos(\omega t) - \sin(\omega t)\right]
\end{aligned}
\tag{2.21}
$$

As before, evanescent and travelling waves emanate only from the left end, and no reflecting waves exist. The semi-infinite solution is very similar to the infinite solution, with no spatial dependence at all. The rolloff is again proportional to k^{-1}.

The actuator to sensor transfer function for the finite beam:

$$
\begin{aligned}
\frac{y_{\mathrm{mf}}}{u_{\mathrm{m}}} &= \frac{w'(0,t)}{M} \\
\frac{y_{\mathrm{mf}}}{u_{\mathrm{m}}} &= -\frac{e^{2kl}(\sin(kl)+\cos(kl))+\sin(kl)-\cos(kl)}{EIk[\cos(kl)(e^{2kl}+1)-2e^{kl}]}
\end{aligned}
\tag{2.22}
$$

where y_{mf} is the output of the moment sensor on a finite beam, u_{m} is the moment input, and l is the beam length.

The finite beam exhibits a more complicated solution due to the waves reflecting at both ends. Since the length is finite, the existence of travelling waves and evanescent waves is understood directly from the transfer function, and the high frequency rolloff is proportional to k^{-1}.

2.2.3 Rectangular Actuator and Sensor

To demonstrate the complexity of solutions associated with shaped actuators and sensors, the sensor output for a rectangular actuator-sensor pair on an infinite beam is determined. Figure 2.7(a) shows the coupled moment and difference of slopes

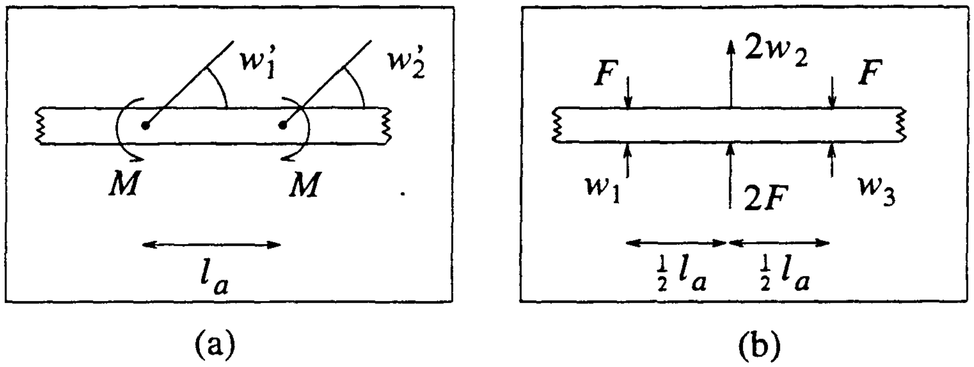

Figure 2.7: Infinite Beams with (a) Rectangular and (b) Triangular Actuator-Sensor Pairs

measurements used to model the rectangular actuator-sensor pair. Since the actuator and sensor are collocated, l_a is the length of the actuator and the length of the sensor. The same solution algorithm is followed as in previous sections, and the sensor output is used to obtain insight into the case of the infinite beam.

The sensor output for the infinite beam:

$$y_{\mathrm{ri}} = w_1' - w_2' \tag{2.23}$$

$$\begin{aligned} y_{\mathrm{ri}} = \frac{m_0}{EIk}\Bigg[& -\sin\left(\frac{kl_a}{2}\right)\sin\left(\omega t + \frac{kl_a}{2}\right) + \sin\left(\frac{kl_a}{2}\right)\sin\left(\omega t - \frac{kl_a}{2}\right) \\ & - \cos\left(\frac{kl_a}{2}\right)\cos\left(\omega t + \frac{kl_a}{2}\right) + \cos\left(\frac{kl_a}{2}\right)\cos\left(\omega t - \frac{kl_a}{2}\right) \\ & - e^{-kl_a}\sin(\omega t) + \sin(\omega t)\Bigg] \end{aligned} \tag{2.24}$$

where y_{ri} is the output of the rectangular sensor on an infinite beam. Unlike the point and moment actuator-sensor pairs, Equation 2.24 shows the influence of travelling and evanescent waves in the solution for the rectangular actuator-sensor pair on an infinite beam. This is due to the spatial distribution of the actuator-sensor pair. Also, the

high frequency rolloff is explicitly proportional to k^{-1}.

2.2.4 Triangular Actuator and Sensor

Here, the sensor output for a triangular actuator-sensor pair on an infinite beam is determined. Figure 2.7(b) shows the three force input and sum of displacements measurements used to model the triangular actuator-sensor pair on an infinite beam. The solution algorithm is the same as in previous sections, and again, the sensor output is used to obtain insight into the case of the infinite beam.

The triangular sensor output for the infinite beam is

$$y_{\text{ti}} = 2w_2 - w_1 - w_3 \tag{2.25}$$

$$\begin{aligned} y_{\text{ti}} = -\frac{f_0}{2EIk^3} \Bigg[& \sin\left(\frac{kl_a}{2}\right)\sin\left(\omega t + \frac{kl_a}{2}\right) + \cos\left(\frac{kl_a}{2}\right)\cos\left(\omega t + \frac{kl_a}{2}\right) \\ & + \sin\left(\frac{kl_a}{2}\right)\sin\left(\omega t - \frac{kl_a}{2}\right) \\ & + \left(2 + \cos\left(\frac{kl_a}{2}\right)\right)\cos\left(\omega t - \frac{kl_a}{2}\right) + e^{-kl_a}\sin(\omega t) \\ & - \left(2\sin\left(\frac{kl_a}{2}\right) - 1\right)\sin(\omega t) - \left(2\cos\left(\frac{kl_a}{2}\right) - 2\right)\cos(\omega t)\Bigg] \end{aligned} \tag{2.26}$$

where y_{ti} is the output of the triangular sensor on an infinite beam, and l_a is the length of the actuator-sensor pair.

Equation 2.26 shows how increased complexity of the actuator-sensor shape increases the complexity of the solution. However, the travelling and evanescent wave

terms can still be seen, and the rolloff is proportional to k^{-3}.

2.3 Asymptotic Solution for Point and Shaped Actuator-Sensor Pairs

Using the wave solution method in Section 2.2, the analytical transfer function for various point and shaped actuator-sensor pairs can be found. Each of these transfer functions has a dereverberated transfer function associated with it which determines the general behavior of the transfer function. If the dereverberated transfer function is known, then an estimate of the crossover frequency and rate of rolloff of the transfer function can be found. Thus, the ability to alter the rolloff characteristics of the dereverberated transfer function implies an ability to alter the rolloff characteristics of the transfer function. This section determines the dereverberated transfer function for point and shaped actuator-sensor pairs, demonstrating how different actuator-sensor shapes affect the actuator to sensor transfer function.

2.3.1 Methodology

The methodology for determining the dereverberated transfer function is explained using examples of transfer functions for point and shaped actuator-sensor pairs on a pinned-pinned beam. The pinned-pinned end conditions are chosen due to the simplicity of the associated modeshapes.

A point actuator-sensor pair at the center of a pinned-pinned beam of length l is

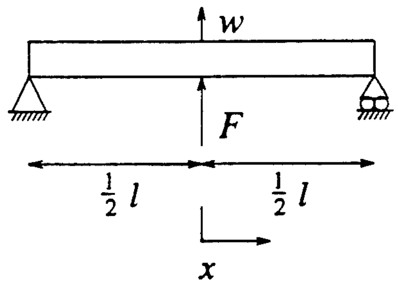

Figure 2.8: Pinned-Pinned Beam with Point Actuator-Sensor Pair

shown in Figure 2.8. The analytical actuator input and sensor output are defined as

$$u_{\mathrm{P}} = F = f_0 \sin(\omega t) \tag{2.27}$$

$$y_{\mathrm{P}} = w(0,t) \tag{2.28}$$

The analytical actuator to sensor transfer function is

$$\frac{y_{\mathrm{P}}}{u_{\mathrm{P}}} = -\frac{e^{\frac{kl}{2}}(\sin(\frac{kl}{2}) - \cos(\frac{kl}{2})) + e^{\frac{-kl}{2}}(\sin(\frac{kl}{2}) + \cos(\frac{kl}{2}))}{4EIk^3\cos(\frac{kl}{2})(e^{\frac{kl}{2}} + e^{\frac{-kl}{2}})} \tag{2.29}$$

The dereverberated transfer function is composed of two asymptotes. The low frequency asymptote, which is the limit as $k \to 0$, and the high frequency asymptote, which is the limit as $k \to \infty$. The low frequency asymptote is found by expanding the transfer function into a series.

$$\lim_{k\to 0} \frac{y_{\mathrm{P}}}{u_{\mathrm{P}}} = -\frac{l^3}{48EI} - \frac{17l^7}{80640EI}k^4 - \frac{691l^{11}}{319334400EI}k^8 - \mathcal{O}k^{12} \tag{2.30}$$

The first term of this series is the remaining term when $k \to 0$; this is the low asymptote.

$$\mathcal{T}_{\mathrm{PLow}} = \frac{-l^3}{48EI} \tag{2.31}$$

The high frequency asymptote is found by taking the limit as $k \to \infty$. The mathe-

matical limit of Equation 2.29 as $k \to \infty$ is

$$\lim_{k\to\infty} \frac{y_p}{u_p} = \frac{\sin(\frac{kl}{2}) - \cos(\frac{kl}{2})}{4EIk^3 \cos(\frac{kl}{2})} \qquad (2.32)$$

The limit of the sinusoidal terms as $k \to \infty$ is between -1 and 1. To determine the high frequency asymptote, either -1 or 1 is substituted for $\sin(\frac{kl}{2})$ and $\cos(\frac{kl}{2})$ in Equation 2.32. When $\sin(\frac{kl}{2}) = 1$ and $\cos(\frac{kl}{2}) = 1$, or when $\sin(\frac{kl}{2}) = -1$ and $\cos(\frac{kl}{2}) = -1$,

$$\lim_{k\to\infty} \frac{y_p}{u_p} = 0 \qquad (2.33)$$

When $\sin(\frac{kl}{2}) = -1$ and $\cos(\frac{kl}{2}) = 1$, or when $\sin(\frac{kl}{2}) = 1$ and $\cos(\frac{kl}{2}) = -1$,

$$\lim_{k\to\infty} \frac{y_p}{u_p} = -\frac{1}{2EIk^3} \qquad (2.34)$$

Only one of these solutions will fit the centerline of the high frequency transfer function; this is the high frequency asymptote. Thus,

$$\mathcal{T}_{\mathrm{PHigh}} = -\frac{1}{2EIk^3} \qquad (2.35)$$

Figure 2.9 shows the two asymptotes of this dereverberated transfer function overlaid by the analytical transfer function of Equation 2.29, where $EI = 1, l = 1$. The low frequency asymptote matches the static behavior, and the high frequency asymptote fits nicely down the middle of the high frequency transfer function. The intercept of these two asymptotes is an estimate for the corner frequency of the transfer function.

Table 2.1 shows the different values of $\mathcal{T}_{\mathrm{PLow}}$ and $\mathcal{T}_{\mathrm{PHigh}}$ when the collocated actuator-sensor pair is placed at different locations of the beam. This shows that as the actuator-sensor pair moves to different points on the beam, the low asymptote

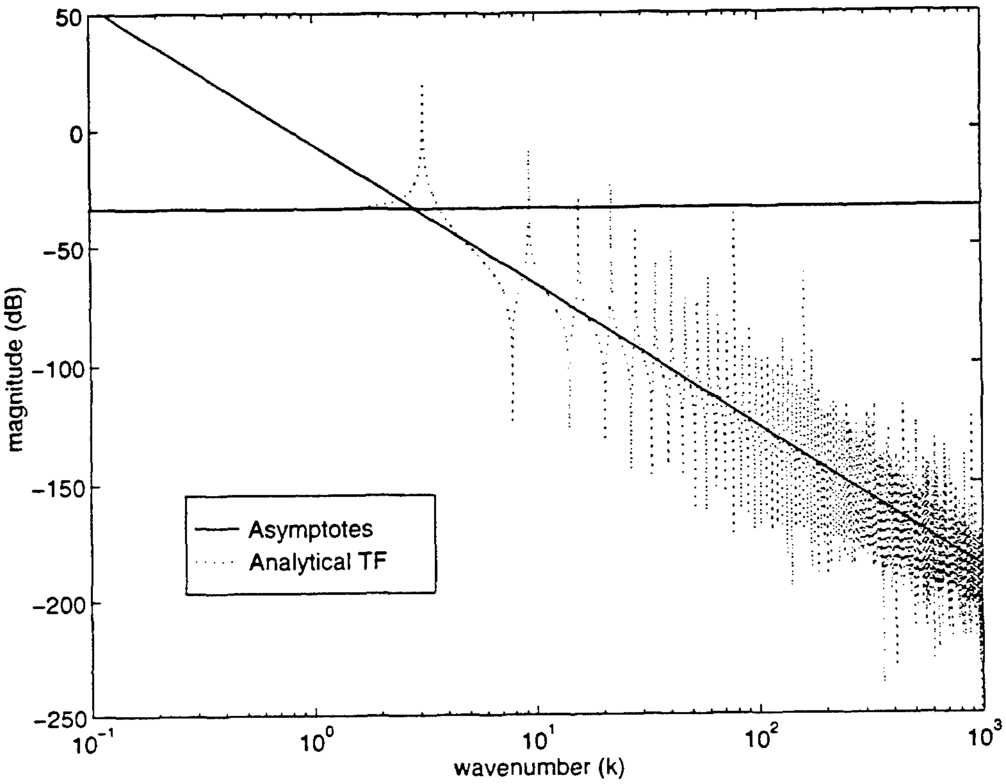

Figure 2.9: Transfer Function for Point Actuator-Sensor Pair Centered on a Pinned-Pinned Beam

Table 2.1: Low and High Frequency Asymptotes for Point Actuator-Sensor Pair at Different Locations on a Pinned-Pinned Beam

Position	$\mathcal{T}_{\text{PLow}}$	$\mathcal{T}_{\text{PHigh}}$
$\frac{l}{2}$	$\frac{l^3}{48EI}$	$\frac{1}{2EIk^3}$
$\frac{l}{3}$	$\frac{4l^3}{243EI}$	$\frac{1}{2EIk^3}$
$\frac{l}{4}$	$\frac{3l^3}{256EI}$	$\frac{1}{2EIk^3}$
$\frac{l}{8}$	$\frac{49l^3}{12288EI}$	$\frac{1}{2EIk^3}$
$\frac{l}{10}$	$\frac{27l^3}{10000EI}$	$\frac{1}{2EIk^3}$

decreases. This is due to the increased local static stiffness of the beam as the point actuator and sensor are moved closer to the pinned end. However, as the actuator-sensor pair are moved along the beam, the high asymptote remains the same as in Equation 2.35. At very high frequencies, the actuator-sensor pair will not change due to its proximity to beam end conditions. Thus, the intercept point is at a minimum when the forcing is at the middle of the beam, but there is no maximum. Also note that the high frequency rolloff is proportional to k^{-3}, which is written explicitly in the denominator of the analytical transfer function, Equation 2.29.

A rectangular actuator-sensor pair centered on a pinned-pinned beam of length l and actuator-sensor length l_a is shown in Figure 2.10(a). The same method is used to determine the dereverberated transfer function of this system. The analytical actuator to sensor transfer function is

$$\frac{y_r}{u_r} = \frac{\mathcal{N}}{EIk\cos(\frac{kl}{2})(e^{\frac{kl}{2}} + e^{\frac{-kl}{2}})} \tag{2.36}$$

where $\mathcal{N}$ is a complicated function of $e^{\frac{kl}{2}}$, $e^{\frac{-kl}{2}}$, $e^{\frac{kl_a}{2}}$, $e^{\frac{-kl_a}{2}}$, $\cos(\frac{kl}{2})$, $\sin(\frac{kl}{2})$, $\cos(\frac{kl_a}{2})$, and $\sin(\frac{kl_a}{2})$. The complete analytical transfer function is listed in Appendix A.

The asymptotes of the dereverberated transfer function for the collocated rectangular pair are

$$\mathcal{T}_{\mathrm{RLow}} = \frac{l_a}{EI} \tag{2.37}$$

$$\mathcal{T}_{\mathrm{RHigh}} = \frac{1}{2EIk} \tag{2.38}$$

From Equation 2.38, the high frequency rolloff is a function of k^{-1}, which is written explicitly in the analytical transfer function, Equation 2.36.

Figure 2.11 shows the two asymptotes overlaid by the analytical transfer function

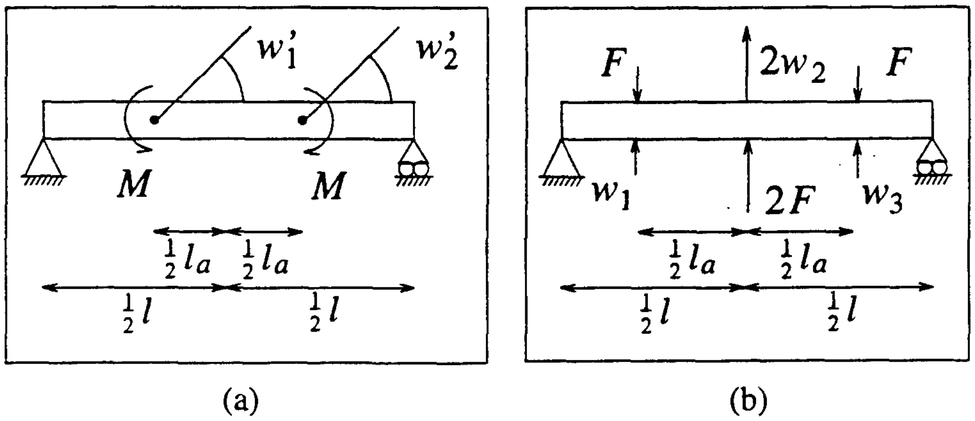

Figure 2.10: Pinned-Pinned Beams with Collocated Actuator-Sensor Pairs (a) Rectangular (b) Triangular

in Equation 2.36, where $EI = 1, l = 1$, and $l_a = \frac{1}{15}$. As the actuator-sensor pair moves to different locations on the beam, the analytical value of the asymptotes remain the same as in Equation 2.37 and Equation 2.38. However, as the size of the actuator and sensor decreases, the numerical value of the low asymptote decreases, increasing the intercept wavenumber. So, although the analytical value of the intercept point is constant, the numerical value decreases with decreasing actuator-sensor length. This implies that the minimum intercept occurs when the rectangular actuator and sensor cover the entire beam. This concurs with physical intuition since the sensor rolls off at the largest wavelength modes, which are the lowest frequency modes. However, it should be noted that when the actuator length is as low as 6.7% of the beam length, the intercept is still near the second pole of the transfer function.

A triangular actuator-sensor pair centered on a pinned-pinned beam of length l and actuator-sensor length l_a is shown in Figure 2.10(b). The dereverberated transfer function is determined in the same manner as the previous cases. The analytical

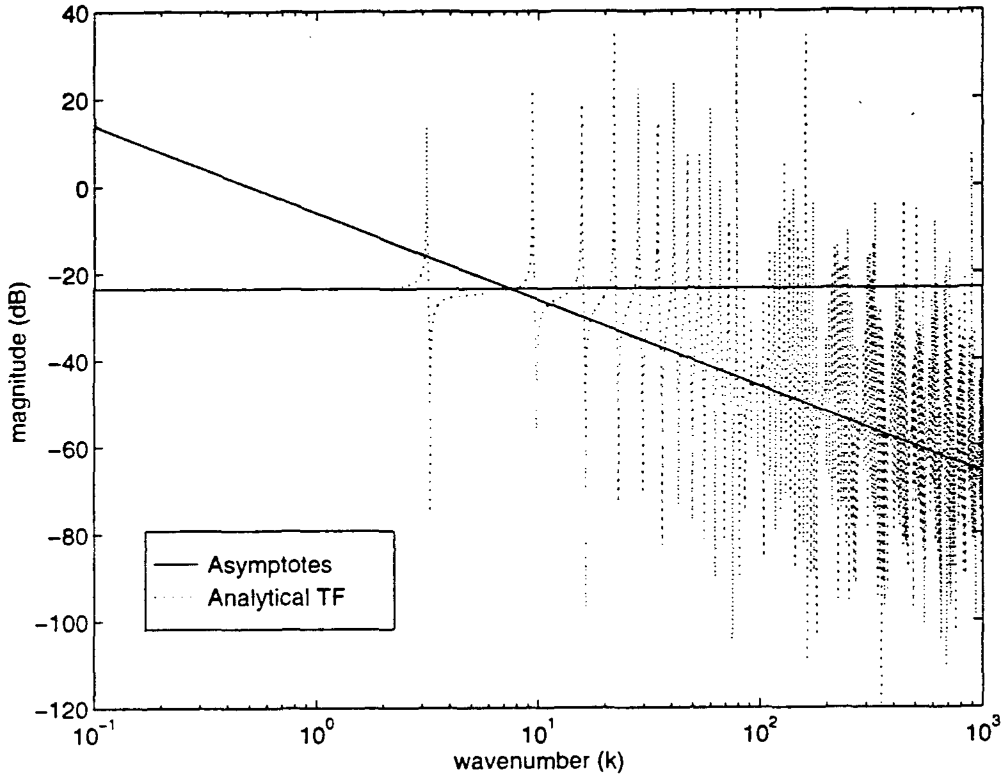

Figure 2.11: Transfer Function for Rectangular Actuator-Sensor Pair on a Pinned-Pinned Beam, $l_a = 6.67\% l$

actuator to sensor transfer function is

$$\frac{y_t}{u_t} = \frac{\mathcal{N}}{EIk^3\cos(\frac{kl}{2})(e^{\frac{kl}{2}} + e^{\frac{-kl}{2}})} \tag{2.39}$$

where $\mathcal{N}$ is a function of $e^{\frac{kl}{2}}$, $e^{\frac{-kl}{2}}$, $e^{\frac{kl_a}{2}}$, $e^{\frac{-kl_a}{2}}$, $\cos(\frac{kl}{2})$, $\sin(\frac{kl}{2})$, $\cos(\frac{kl_a}{2})$, and $\sin(\frac{kl_a}{2})$, and is more complicated than the rectangular analytical transfer function. The complete analytical transfer function can be found in Appendix A.

The asymptotes of the dereverberated transfer function for the triangular actuator-

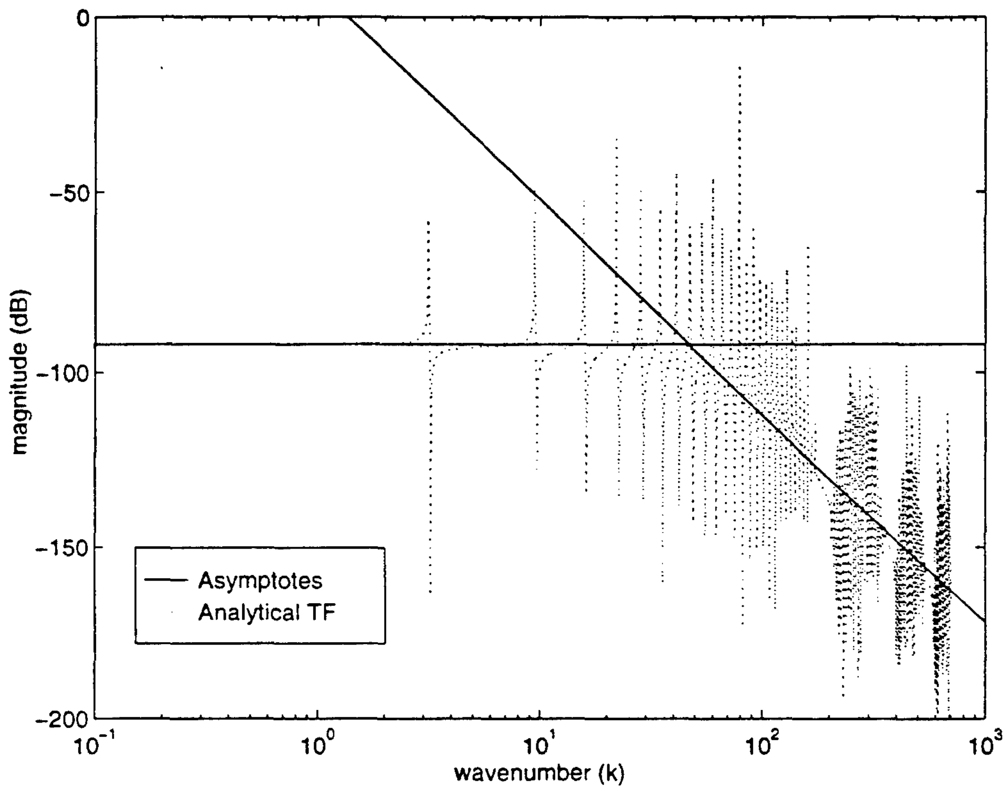

Figure 2.12: Transfer Function for Triangular Actuator-Sensor Pair on a Pinned-Pinned Beam, $l_a = 6.67\% l$

sensor pair are

$$\mathcal{T}_{\text{TLow}} = \frac{l_a^3}{12EI} \tag{2.40}$$

$$\mathcal{T}_{\text{THigh}} = \frac{5}{2EIk^3} \tag{2.41}$$

The high frequency rolloff of the triangular actuator to sensor transfer function is a function of k^{-3}. This is written explicitly in the analytical transfer function, Equation 2.39.

Figure 2.12 shows the analytical transfer function of Equation 2.39 overlaid by the two dereverberated asymptotes where $EI = 1, l = 1$, and $l_a = \frac{1}{15}$. As in the rectangu-

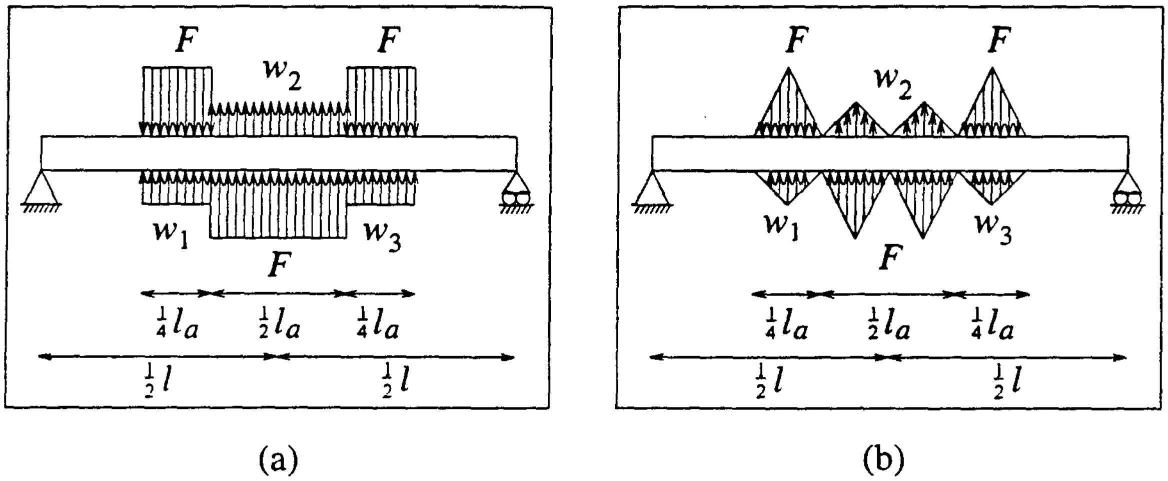

Figure 2.13: Pinned-Pinned Beams with Collocated Actuator-Sensor Pairs (a) Quadratic (b) Cubic

lar case, when the triangular actuator-sensor pair moves to different locations on the beam, the analytical value of the asymptotes remains the same. Also, as the size of the actuator and sensor decreases, the value of the low asymptote decreases, increasing the intercept wavenumber. Therefore, the numerical value of the low frequency asymptote decreases with decreasing actuator-sensor length.

As in the rectangular case, the minimum intercept occurs when the distributed actuator and sensor cover the entire beam. However, since the low frequency asymptote of the triangular sensor is a function of l^3 instead of l, the intercept of the asymptotes is much higher in frequency for a triangular actuator-sensor pair than the rectangular actuator-sensor pair. For example, when the rectangular actuator-sensor pair covers 6.7% the entire beam, as in the Figure 2.11, the intercept occurs near the second pole. However, when the triangular pair covers the same length, as in the Figure 2.12, the intercept is near the eighth pole of the transfer function, a difference of nearly 40 in k.

A quadratic actuator-sensor pair centered on a pinned-pinned beam of length l

and actuator-sensor length l_a is shown in Figure 2.13(a). The analytical actuator to sensor transfer function is

$$\frac{y_{\rm q}}{u_{\rm q}} = \frac{\mathcal{N} - 2kl_a \cos(\frac{kl}{2})(e^{kl} - 1)}{EIk^5 \cos(\frac{kl}{2})(e^{kl} + 1)} \tag{2.42}$$

where $\mathcal{N}$ is a function of exponential and sinusoidal terms more complicated than the triangular analytical transfer function. The complete transfer function for this case is also found in Appendix A.

The asymptotes of the dereverberated transfer function are determined using the same method as in previous cases. These asymptotes are

$$\mathcal{T}_{\rm QLow} = \frac{23l_a^5}{15360EI} \tag{2.43}$$

$$\mathcal{T}_{\rm QHigh} = \frac{l_a}{EIk^4} \tag{2.44}$$

The high frequency rolloff of the quadratic is a function of k^{-4}. However, this is not written explicitly in the denominator of the analytical transfer function. Instead, the denominator is a function of k^5 and the numerator is a function of k, which mathematically limits the rolloff to a function of k^{-4}.

This conclusion can be reached by considering the phase of the actuator to sensor transfer function. In the collocated case, the phase will always be between 0° and −180°. In the worst case, −180° of phase, the system rolls off as a function of k^{-4}. Therefore, as long as the actuator-sensor pair are collocated, the dereverberated transfer function cannot rolloff faster than k^{-4}.

Figure 2.14 shows the analytical transfer function of Equation 2.42 and the two dereverberated asymptotes, where $EI = 1, l = 1$, and $l_a = \frac{1}{15}$. As in the rectangular and triangular cases, when the quadratic actuator-sensor pair moves to different lo-

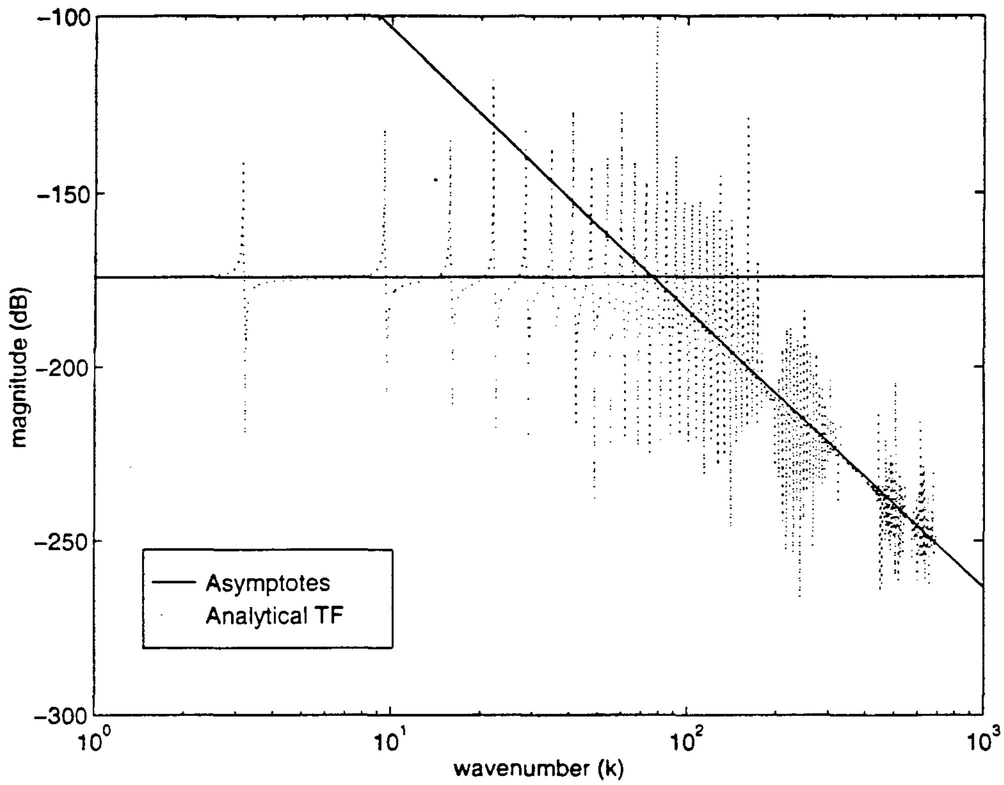

Figure 2.14: Transfer Function for Quadratic Actuator-Sensor Pair on a Pinned-Pinned Beam

cations on the beam, the analytical value of the asymptotes remains the same. The characteristics of the intercept frequency are the same as in the rectangular and triangular cases as well. The numerical value of the low frequency asymptote decreases with decreasing actuator-sensor length. Once again, the minimum intercept occurs when the distributed actuator and sensor cover the entire beam. However, in the quadratic case the low frequency asymptote is a function of l^5. As a result, the intercept of the asymptotes of a quadratic pair is higher in frequency than that of a triangular or rectangular actuator-sensor pair of the same length. As seen in Figure 2.14, the intercept of the asymptotes is near the 13th pole which is much higher than the triangular and rectangular transfer functions.

A cubic actuator-sensor pair centered on a pinned-pinned beam of length l and actuator-sensor length l_a is shown in Figure 2.13(b). The analytical actuator to sensor transfer function is

$$\frac{y_c}{u_c} = \frac{\mathcal{N} + k^3 l_a^3 \cos(\frac{kl}{2})(e^{kl}+1)}{EIk^7 \cos(\frac{kl}{2})(e^{kl}+1)} \tag{2.45}$$

where $\mathcal{N}$ is a function of exponential and sinusoidal terms more complicated than the quadratic analytical transfer function. The complete analytical transfer function is listed in Appendix A.

The asymptotes for the cubic case are:

$$\mathcal{T}_{\text{CLow}} = \frac{4021 l_a^7}{660602880EI} \tag{2.46}$$

$$\mathcal{T}_{\text{CHigh}} = \frac{l_a^3}{192EIk^4} \tag{2.47}$$

The high frequency rolloff of the cubic is a function of k^{-4}. However, as in the quadratic case this is not written explicitly in the denominator of the analytical transfer function. Instead, the denominator is a function of k^7 and the numerator is a function of k^3, which mathematically limits the rolloff to a function of k^{-4}. Again, this result concurs with the natural physical limits of the system.

Figure 2.15 shows the two dereverberated asymptotes and the analytical transfer function in Equation 2.45, where $EI = 1, l = 1$, and $l_a = \frac{1}{15}$. The intercept of the asymptotes of this transfer function is near the 13th pole of the system. As in previous cases, the analytical value of the asymptotes remains the same, when the cubic actuator-sensor pair moves to different locations on the beam. Also, the numerical value of the low frequency asymptote decreases with decreasing actuator-sensor length. The minimum intercept occurs when the distributed actuator and sensor cover the entire beam. In the cubic case, the low frequency asymptote is a

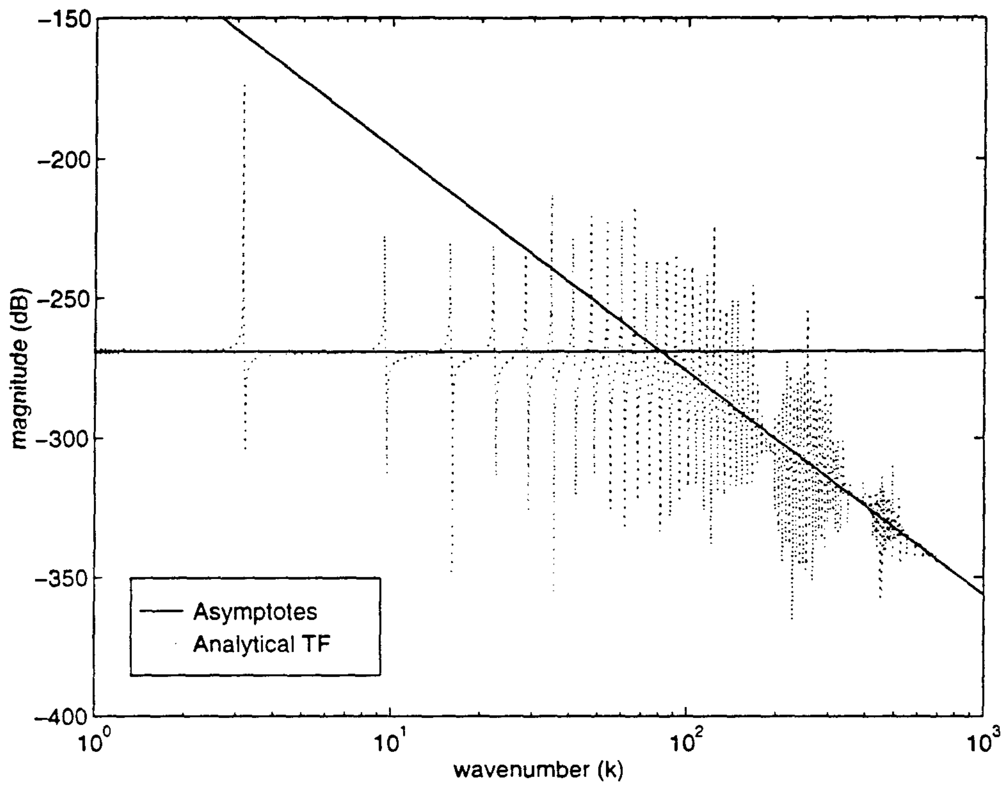

Figure 2.15: Transfer Function for Cubic Actuator-Sensor Pair on a Pinned-Pinned Beam

function of l^7. However, since the high frequency asymptote is a function of l^3, the intercept for the cubic dereverberated transfer function is nearly the same as the intercept for the quadratic case. This is due to the rolloff limitation of k^{-4} which is naturally set for the system.

These examples show that any shape more complex than a quadratic will not contribute additional rolloff to the system, since the rolloff is physically limited to k^{-4}. Additionally, the manufacturing of a shape more complex than the triangular is very difficult, further limiting the benefits of using these shapes. Therefore, there will be no further investigation of shapes more complex than triangular.

2.3.2 Correlation of Asymptotes using Modal Residue Solution

In order to confirm that the asymptotes of the wave solution are correct, another modelling technique is used to determine the transfer functions and their dereverberated solutions. The modal residue solution uses a Rayleigh-Ritz solution of a Bernoulli-Euler beam [17], assuming the modes of a pinned-pinned beam to be $\sin\left(\frac{n\pi x}{l}\right)$, where n is the mode number and l is the length of the beam [4].

The modal solution for the transfer function from point actuator to point sensor centered on a pinned-pinned beam is

$$\frac{y_p}{u_p} = \sum_{n=1}^{\infty} \frac{-2\sin^2\left(\frac{n\pi}{2}\right)}{lEI(k^4 - k_n^4)} \tag{2.48}$$

where the natural wavenumber is $k_n^2 = \sqrt{\frac{m\omega_n^2}{EI}}$.

To determine the dereverberated transfer function, the contributions of each mode is reduced to that of an asymptotic Bode plot.

$$\frac{y_p}{u_p} = \sum_{n=1}^{\infty} \begin{cases} \dfrac{2\sin^2\left(\dfrac{n\pi}{2}\right)}{lEIk_n^4} & k \leq k_n \\ \dfrac{-2\sin^2\left(\dfrac{n\pi}{2}\right)}{lEIk^4} & k \geq k_n \end{cases} \tag{2.49}$$

Approximately 1000 of these dereverberated modes are summed to generate the modal solution dereverberated transfer function. This solution compares favorably to the asymptotic wave solution in Figure 2.16; the low frequency asymptote is nearly exact and the high frequency asymptote is very close.

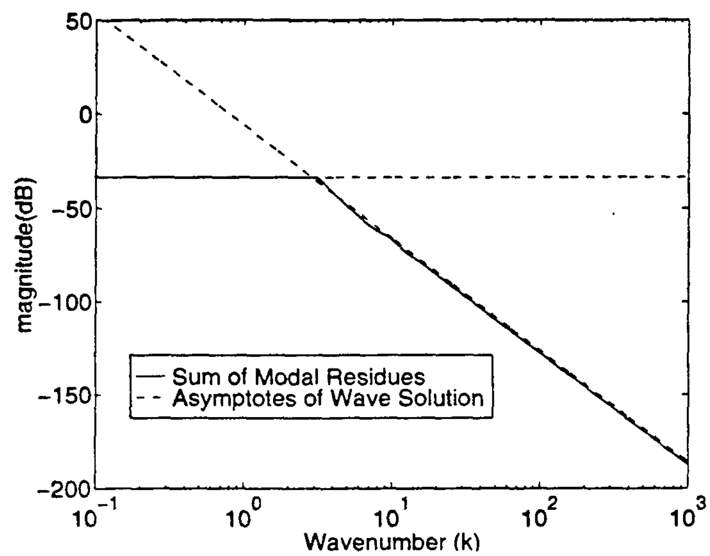

Figure 2.16: Modal Residue Solution vs. Dereverberated Wave Model for a Point Actuator-Sensor Pair Centered on a Pinned-Pinned Beam

The method for finding the dereverberated transfer functions for the shaped actuator-sensor pairs is the same as for the point actuator-sensor pair. The modal solution of the transfer function for a rectangular actuator and sensor centered on a pinned-pinned beam is

$$\frac{y_r}{u_r} = \sum_{n=1}^{\infty} \frac{8\pi^2 n^2 \left(\cos^2\left(\frac{n\pi}{2}\right) - 1\right)\left(\cos^2\left(\frac{n\pi l_a}{2l}\right) - 1\right)}{l^3 EI(k^4 - k_n^4)} \tag{2.50}$$

The modal solution for the triangular actuator to sensor transfer function is

$$\frac{y_t}{u_t} = \sum_{n=1}^{\infty} \frac{-8\left(\cos^2\left(\frac{n\pi}{2}\right) - 1\right)\left(\cos\left(\frac{n\pi l_a}{2l}\right) - 1\right)^2}{lEI(k^4 - k_n^4)} \tag{2.51}$$

The modal solution of the transfer function for the quadratic actuator-sensor pair is

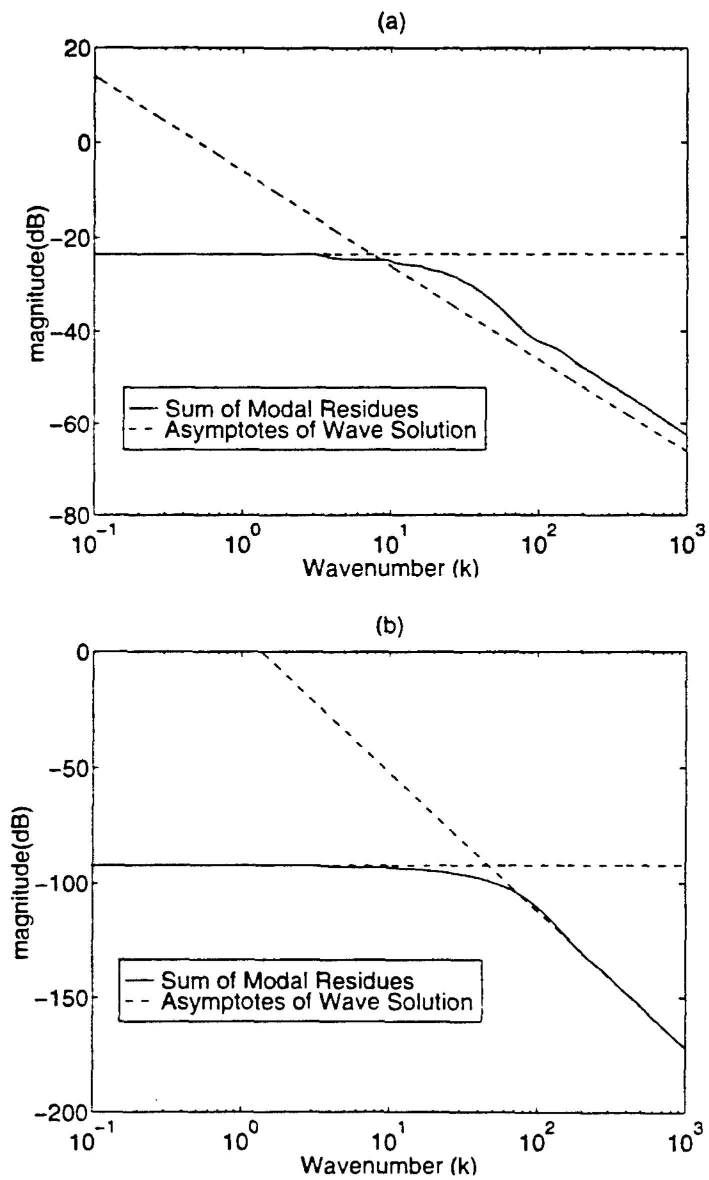

Figure 2.17: Modal Residue Solution and Dereverberated Wave Solution where $l_a = 6.67\%l$ on Pinned-Pinned Beam (a) Rectangular (b) Triangular

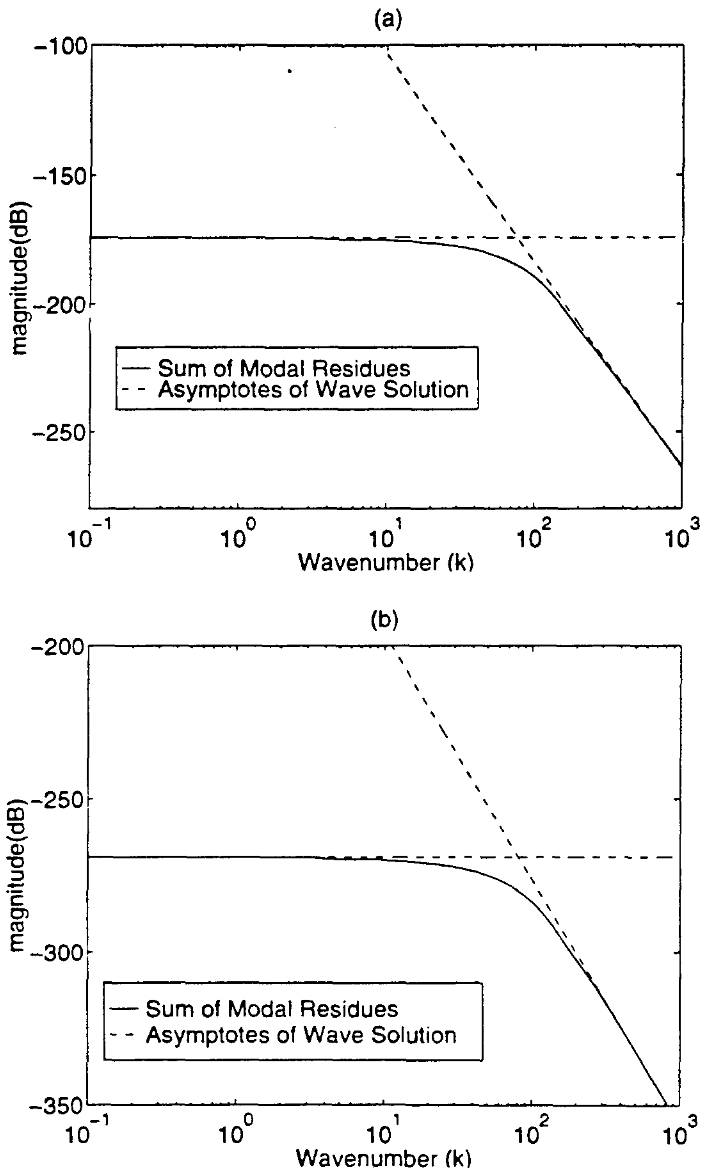

Figure 2.18: Modal Residue Solution and Dereverberated Wave Solution where $l_a = 6.67\%l$ on Pinned-Pinned Beam (a) Quadratic (b) Cubic

$$\frac{y_q}{u_q} = \sum_{n=1}^{\infty} \frac{-8l\left(\cos^2\left(\frac{n\pi}{2}\right)-1\right)\left(\cos^2\left(\frac{n\pi l_a}{2l}\right)+4\cos^2\left(\frac{n\pi l_a}{4l}\right)+4\sin\left(\frac{n\pi l_a}{4l}\right)\sin\left(\frac{n\pi l_a}{2l}\right)-5\right)}{n^2\pi^2 EI(k^4-k_n^4)} \tag{2.52}$$

The modal solution of the transfer function for the cubic actuator-sensor pair is

$$\frac{y_c}{u_c} = \sum_{n=1}^{\infty} \frac{8l^3\left(\cos^2\left(\frac{n\pi}{2}\right)-1\right)\left(2\cos\left(\frac{3n\pi l_a}{8l}\right)-\cos\left(\frac{n\pi l_a}{2l}\right)-2\cos\left(\frac{n\pi l_a}{8l}\right)+1\right)^2}{n^4\pi^4 EI(k^4-k_n^4)} \tag{2.53}$$

The dereverberated modal transfer functions of the shaped actuator-sensor pairs are determined using the same algorithm as the point actuator-sensor pair. These transfer functions are compared to the asymptotic wave solution in Figures 2.17 and 2.18.

These four plots show that the two solution methods match very well at low frequency. At high frequency, the correlation of the modal solution asymptote to the wave solution asymptote increases as the actuator-sensor shape increases in complexity. While the correlation of the asymptotes for the simpler shapes is not as precise as the more complex shapes, these results are accurate enough to confirm the results of the wave solutions.

2.3.3 Asymptotes for Various End Conditions

Table 2.2 summarizes the low frequency and high frequency asymptotes for different shaped actuator-sensor pairs on a pinned-pinned beam. The value for the low frequency asymptote of the point actuator to sensor transfer function corresponds to actuator-sensor placement at the center of the beam. The asymptotes for the shaped actuator-sensor pairs are independent of their placement on the beam. Table 2.3 and Table 2.4 summarize the same information for cantilevered and free-free

Table 2.2: Low and High Frequency Asymptotes for a Pinned-Pinned Beam

Shape	Low	High
Point	$\frac{l^3}{48EI}$	$\frac{1}{2EIk^3}$
Rectangular	$\frac{l_a}{EI}$	$\frac{1}{2EIk}$
Triangular	$\frac{l_a^3}{12EI}$	$\frac{5}{2EIk^3}$

Table 2.3: Low and High Frequency Asymptotes for a Cantilevered Beam

Shape	Low	High
Point	$\frac{l^3}{24EI}$	$\frac{1}{4EIk^3}$
Rectangular	$\frac{l_a}{EI}$	$\frac{1}{2EIk}$
Triangular	$\frac{l_a^3}{12EI}$	$\frac{5}{2EIk^3}$

end conditions.

From these three tables, it is evident that for a point actuator-sensor pair, the low frequency asymptote is dependent upon beam location and beam end conditions, which is due to a local beam stiffness effect. Discounting singularities, the high frequency asymptote is not dependent upon its location on the beam. However, it is dependent upon the specific beam end conditions due to the effects of evanescent

Table 2.4: Low and High Frequency Asymptotes for a Free-Free Beam

Shape	Low	High
Point	$\frac{1}{lEIk^4}$	$\frac{1}{4EIk^3}$
Rectangular	$\frac{l_a}{EI}$	$\frac{1}{2EIk}$
Triangular	$\frac{l_a^3}{12EI}$	$\frac{5}{2EIk^3}$

waves. The low frequency and high frequency asymptotes of all shaped actuator to sensor transfer functions are the same regardless of beam placement and end conditions, as long as there are no singularities and the end conditions are statically determinate.

2.4 Discussion

This chapter has discussed the modelling of Bernoulli-Euler beams with point and shaped actuator-sensor pairs. The dereverberated transfer functions for several cases were determined, and several insights were gained. First, it is possible to use different shapes of actuator-sensor pairs to shape the dereverberated transfer function of the plant. The rolloff of the point actuator-sensor pair is proportional to k^{-3}, the rolloff of the rectangular actuator-sensor pair is proportional to k^{-1}, the rolloff of the triangular actuator-sensor pair is proportional to k^{-3}, the rolloff of the quadratic actuator-sensor pair is proportional to k^{-4}, and the rolloff of the cubic actuator-sensor pair is also proportional to k^{-4}. Note, there is a limit of k^{-4} for rolloff that is obtainable. Also, as the shapes become more complex, the corner frequency at which the transfer function begins to roll off increases. There are also limitations which make shapes more complex than triangular difficult to manufacture. Additionally, the point actuator to sensor dereverberated transfer function changes depending upon the location of the actuator-sensor pair and the end conditions of the beam. The shaped actuator to sensor dereverberated transfer functions are the same regardless of its location on the beam and regardless of the beam end conditions, if those end conditions are statically determinate.

From these observations, general rules can be stated for any transfer function of

a collocated actuator-sensor pair on a beam. If the type of actuator-sensor pair is known, the rate of rolloff is known as well. When distributed shaped sensors are used, the intercept is known, and the crossover frequency can be estimated. It is not necessary to know the exact location of the actuator-sensor pair to understand behavior of the transfer function. Thus, an appropriate actuator-sensor pair can be chosen for certain plant transfer function characteristics. Finally, the benefits of using shapes more complex than triangular do not outweigh the associated costs. Therefore, they should not be considered.

Chapter 3

Analytical Models for Noncollocated Actuator-Sensor Pairs

In this chapter, transfer functions of point and shaped noncollocated actuator-sensor pairs on a Bernoulli-Euler beam are derived. As with collocated sensors and actuators, wave solutions are employed, and subsequently the underlying physics in these relations is examined. The characteristics of the dereverberated transfer functions are investigated, and the effect of noncollocation of actuator-sensor pairs is considered.

3.1 Wave Solution for Simple Transfer Functions

In order to obtain insight into the physical significance of the noncollocated actuator to sensor transfer functions, a few mathematically simple examples are solved. These include a point force actuator-sensor pair on an infinite, semi-infinite, and finite free-free beam, as well as a moment actuator-sensor pair on an infinite, semi-infinite, and finite free-free beam. The free-free end conditions are chosen for their similarity to the infinite and semi-infinite beams. These results are then compared to the collocated results found in Chapter 2.

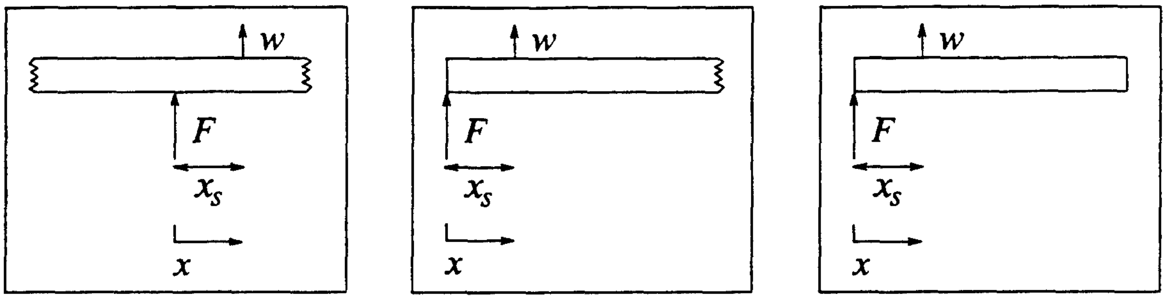

Figure 3.1: Noncollocated Point Actuator-Sensor Pairs on (a) Infinite, (b) Semi-infinite, (c) Finite beam

3.1.1 Point Actuator and Sensor

The behavior of a noncollocated point actuator-sensor pair on an infinite, semi-infinite, and finite free-free beam is determined using the solution method in Section 2.2. A point force and displacement measurement are used to model the point actuator-sensor pair; Figure 3.1 shows these three cases. The forcing function $F(x,t)$ is assumed to be of the form $f_0 \sin(\omega t)$. The variable x_s is the distance from the actuator to the sensor.

As in Section 2.2, the physical insights of the infinite and semi-infinite cases come from the sensor output, and the physical insights of the finite beam are obtained from the actuator to sensor transfer function.

The sensor output (displacement) for the infinite case is

$$
\begin{aligned}
y_{\text{pin}} &= w(x_s,t) \\
y_{\text{pin}} &= \begin{cases} \dfrac{f_0}{4EIk^3}\left[\cos(\omega t + kx_s) + e^{kx_s}\sin(\omega t)\right], & x \le 0 \\ -\dfrac{f_0}{4EIk^3}\left[\cos(\omega t - kx_s) + e^{-kx_s}\sin(\omega t)\right], & x \ge 0 \end{cases}
\end{aligned}
\tag{3.1}
$$

where y_{pin} is the output of a point sensor on an infinite beam, where the actuator and sensor are noncollocated.

If $x_s = 0$, then Equation 3.1 is the collocated result found in Equation 2.14. The simplicity of the infinite solution is due to symmetry and the lack of reflecting waves. The sensor output clearly shows the effect of travelling waves and evanescent waves upon the beam.

The sensor output for the semi-infinite beam is

$$
\begin{aligned}
y_{\text{psn}} &= w(x_s, t) \\
y_{\text{psn}} &= -\frac{f_0}{2EIk^3}\left[\sin(\omega t - kx_s) + \cos(\omega t - kx_s) + e^{-kx_s}(\sin(\omega t) + \cos(\omega t))\right] \quad (3.2)
\end{aligned}
$$

where y_{psn} is the output of a point sensor on a semi-infinite beam, where the actuator and sensor are noncollocated.

Substituting $x_s = 0$ in Equation 3.2 confirms the collocated results of Equation 2.17. Since the input of the semi-infinite beam is at the left (finite) end, evanescent and travelling waves emanate only from the left end, and no reflecting waves exist. Equation 3.2 is more complicated than the infinite beam sensor output, but, the effect of the travelling waves and evanescent waves is easily discernible.

The actuator to sensor transfer function for the finite beam is

$$
\begin{aligned}
\frac{y_{\text{pfn}}}{u_{\text{p}}} &= \frac{w(x_s, t)}{F} \\
C &= \frac{1}{2EIk^3\left(\cos(kl)(e^{kl} + e^{-kl}) - 2\right)}
\end{aligned}
$$

$$\frac{y_{\mathrm{pfn}}}{u_{\mathrm{p}}} = C\Big[\cos(kx_s)(e^{kl}(\sin(kl) - \cos(kl)) + e^{-kl}(\sin(kl) + \cos(kl))$$
$$- \sin(kx_s)(e^{kl}(\sin(kl) + \cos(kl)) + e^{-kl}(-\sin(kl) + \cos(kl)) - 2)$$
$$+ e^{kx_s}(e^{-kl}(\sin(kl) + \cos(kl)) - 1)$$
$$+ e^{-kx_s}(e^{kl}(\sin(kl) - \cos(kl)) + 1)\Big] \quad (3.3)$$

where l is the beam length, and y_{pfn} is the output of a point sensor on a finite beam, when the actuator and sensor are noncollocated.

The finite beam has a very complicated solution because the it experiences reflecting and evanescent waves from both ends. Since the length is finite, there are no time dependent terms and the effect of travelling waves and evanescent waves is understood directly from the transfer function. Again, if $x_s = 0$ is substituted into Equation 3.3, then the transfer function simplifies to the simpler collocated transfer function found in Equation 2.18.

3.1.2 Transfer Function Relationship to a Pinned Boundary Condition

Consider the case of a collocated point actuator-sensor pair on a finite beam. A known relationship exists between the zeros of the actuator to sensor transfer function and the poles of the transfer function when a the actuator-sensor pair are replaced with a pinned boundary condition. This subsection investigates whether there is a similar relationship in the noncollocated case.

Two beams are pictured in Figure 3.2, the first was discussed Section 2.2.1, while the second beam was discussed in Section 3.1.1. From Equation 2.18 the transfer

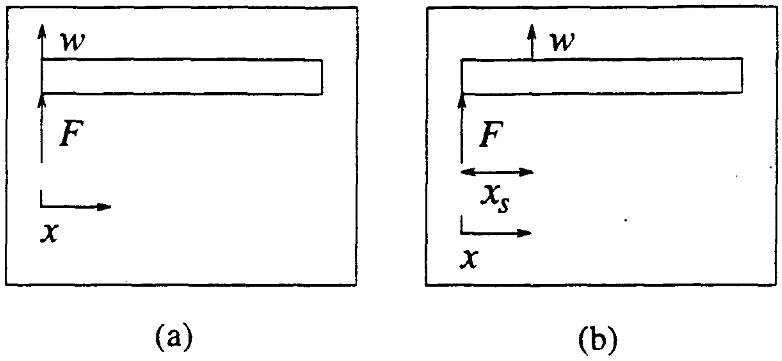

Figure 3.2: Free-Free Beams with (a) Collocated, (b) Noncollocated Point Actuator-Sensor Pairs

function for the collocated actuator-sensor pair in Figure 3.2(a) is

$$\frac{y_{\mathrm{pf}}}{u_{\mathrm{p}}} = -\frac{e^{kl}(\sin(kl) - \cos(kl)) + e^{-kl}(\sin(kl) + \cos(kl))}{EIk^3[\cos(kl)(e^{kl} + e^{-kl}) - 2]} \tag{3.4}$$

where l is the beam length.

The effect of high gain control on a collocated transfer function is now considered. A proportional controller, with gain $\mathcal{K}$, is included and the loop is closed. When $\mathcal{K} \to \infty$ the poles of the closed loop transfer function move to the open loop zeros, i.e. the zeros of Equation 3.4. The poles of the closed loop transfer function are now defined as the values of k where

$$0 = e^{kl}(\sin(kl) - \cos(kl)) + e^{-kl}(\sin(kl) + \cos(kl)) \tag{3.5}$$

This is the same equation which defines the poles of a beam with a free end at $x = l$ and a pin at $x = 0$, the position of the actuator-sensor pair in Figure 3.2(a). Thus as the gain of the controller increases, the location of the actuator-sensor pair becomes infinitely stiff.

The same procedure can be followed in the noncollocated case, Figure 3.2(b).

As $\mathcal{K} \to \infty$, the poles of the closed loop transfer function move to the zeros of Equation 3.3. The high gain closed loop poles are defined as the values of k where

$$\begin{aligned} 0 = \Big[& \cos(kx_s)(e^{kl}(\sin(kl) - \cos(kl)) + e^{-kl}(\sin(kl) + \cos(kl)) \\ & - \sin(kx_s)(e^{kl}(\sin(kl) + \cos(kl)) + e^{-kl}(-\sin(kl) + \cos(kl)) - 2) \\ & + e^{kx_s}(e^{-kl}(\sin(kl) + \cos(kl) - 1) \\ & + e^{-kx_s}(e^{kl}(\sin(kl) - \cos(kl) + 1)\Big] \end{aligned} \tag{3.6}$$

The poles of a system where the location of the actuator is pinned are the same as the poles in the collocated case, as in Equation 3.5. The poles of a system where the location of the sensor at x_s is pinned are defined as the values of k where

$$\begin{aligned} 0 = 2\cos(kl) & \Big[e^{-kl}\Big(e^{kx_s}\big(\sin(kx_s) - \cos(kx_s)\big) - \cos^2(kx_s)\Big) \\ & + e^{kl}\Big(e^{-kx_s}\big(\sin(kx_s) + \cos(kx_s)\big) + \cos^2(kx_s)\Big)\Big] \\ +2\sin(kl) & \Big[e^{-kl}\Big(e^{kx_s}\big(-\sin(kx_s) - \cos(kx_s) - \frac{1}{2}e^{kx_s}\big) - \cos(kx_s)\sin(kx_s) - \frac{1}{2}\Big) \\ & + e^{kl}\Big(e^{-kx_s}\big(\sin(kx_s) - \cos(kx_s) - \frac{1}{2}e^{-kx_s}\big) + \cos(kx_s)\sin(kx_s) - \frac{1}{2}\Big)\Big] \\ +2\cos(kl) & \Big[e^{kx_s} - e^{-kx_s}\Big] \\ +2\sin(kl) & \Big[-e^{kx_s} - e^{-kx_s}\Big] \end{aligned} \tag{3.7}$$

Table 3.1 lists k_{TF}, the values of k which are the zeros of the noncollocated actuator-sensor transfer function in Equation 3.6. Also listed is k_{ActPin}, the values of k which are the poles of the beam in Figure 3.2(b) with a pin at the location of the actuator, as in Equation 3.5. Finally, the table lists k_{SensPin}, the values of k which are the poles of the beam in Figure 3.2(b) with a pin at the location of the sensor, as in

Table 3.1: Values of k for Poles of Beams with Pinned Boundaries and Zeros of Noncollocated Point Actuator-Sensor Transfer Function

k_{TF}	k_{ActPin}	k_{SensPin}
4.592	3.926	4.706
8.611	7.068	7.225
12.703	10.210	9.737
16.698	13.352	13.314
20.633	16.493	17.031

Equation 3.7. From this table, it is obvious that neither a pin at the actuator, nor a pin at the sensor models the noncollocated system with high gain.

Another way to consider the noncollocated system is using the s-domain transfer function. It is obvious that at some high frequency the deflection of the beam at the point of the sensor will be opposite to direction of the force. Therefore, the s-domain transfer function must have nonminimum phase zeros. This implies that with high static gain, $\mathcal{K} \rightarrow \infty$, the system will go unstable. Thus, there is no simple boundary which replicates the poles of the noncollocated case, as there is in the collocated problem.

3.1.3 Moment Actuator and Slope Sensor

The behavior for a noncollocated moment actuator and slope sensor on an infinite, semi-infinite, and finite free-free beam is determined using the wave solution. A moment input and slope measurement are used to model the moment actuator-sensor pair; Figure 3.3 shows these three cases. The forcing function $M(x,t)$ is assumed to be of the form $m_0 \sin(\omega t)$. The dimension x_s is the distance from the actuator to the

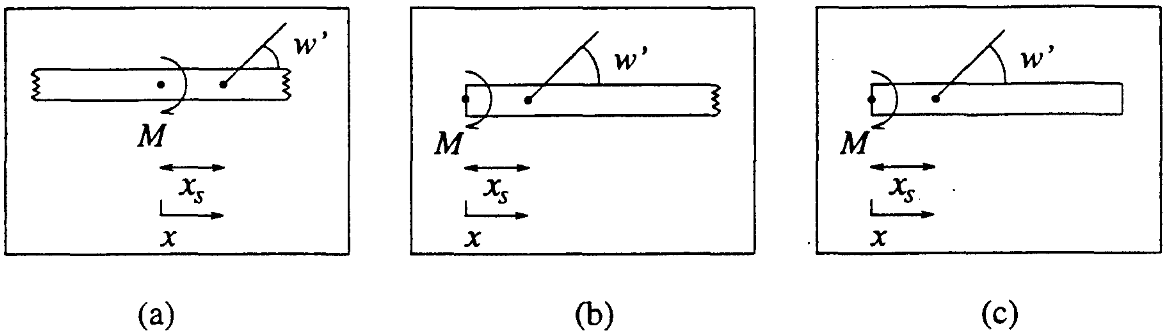

Figure 3.3: Noncollocated Moment Actuator and Slope Sensor on (a) Infinite, (b) Semi-infinite, (c) Finite beam

sensor. The sensor output for the infinite and semi-infinite cases and the actuator-sensor transfer function for the finite case are determined in the same manner as for the point actuator-sensor pair.

The slope sensor output for the infinite case is

$$\begin{aligned} y_{\text{min}} &= w'(x_s,t) \\ y_{\text{min}} &= \begin{cases} \frac{m_0}{4EIk}\left[-\cos(\omega t + kx_s) + e^{kx_s}\sin(\omega t)\right], & x_s \le 0 \\ \frac{m_0}{4EIk}\left[-\cos(\omega t - kx_s) + e^{-kx_s}\sin(\omega t)\right], & x_s \ge 0 \end{cases} \end{aligned} \tag{3.8}$$

where y_{min} is the output of the slope sensor when there is a *m*oment input on an *i*nfinite beam, where the actuator and sensor are *n*oncollocated.

Substituting $x_s = 0$ confirms the solution for the collocated case found in Equation 2.20. Again, the simplicity of the infinite solution is due to symmetry and the lack of reflecting waves. The slope sensor output clearly shows the effect of travelling waves and evanescent waves upon the beam.

The slope sensor output for the semi-infinite beam is

$$y_{\text{msn}} = w'(x_s,t)$$

$$y_{\mathrm{msn}} = \frac{m_0}{2EIk}\left[\cos(\omega t - kx_s) - \sin(\omega t - kx_s) + e^{-kx_s}(\cos(\omega t) - \sin(\omega t))\right] \quad (3.9)$$

Substituting $x_s = 0$ in Equation 3.9 confirms the collocated results of Equation 2.21. As before, evanescent and travelling waves emanate only from the left end, and no reflecting waves exist. Although the semi-infinite solution has more terms than the infinite solution, the travelling waves and evanescent waves are easily identified.

The actuator to sensor transfer function for the finite beam is

$$\begin{aligned} \frac{y_{\mathrm{mfn}}}{u_{\mathrm{m}}} &= \frac{w'(x_s, t)}{M} \\ D &= \frac{1}{2EIk\,(\cos(kl)(e^{2kl}+1) - 2e^{kl})} \end{aligned}$$

$$\begin{aligned} \frac{y_{\mathrm{mfn}}}{u_{\mathrm{m}}} = D\Big[& \cos(kx_s)((1-e^{2kl})\cos(kl) + (-1-e^{2kl})\sin(kl)) \\ & - \sin(kx_s)((e^{2kl}+1)\cos(kl) + (1-e^{2kl})\sin(kl) - 2e^{kl}) \\ & + e^{-kx_s}(-e^{2kl}(\sin(kl)+\cos(kl)) + e^{kl}) \\ & + e^{kx_s}(-\sin(kl) + \cos(kl) - e^{kl})\Big] \end{aligned} \quad (3.10)$$

The finite beam has the most complicated solution due to the reflecting and evanescent waves from both ends. Since the length is finite, the effect of travelling waves and evanescent waves is understood directly from the transfer function. Again, the transfer function simplifies to the collocated transfer function, Equation 2.22, when $x_s = 0$.

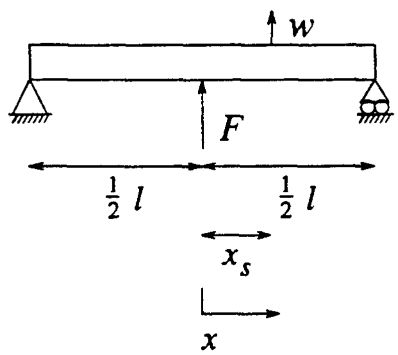

Figure 3.4: Noncollocated Point Actuator-Sensor Pair on a Pinned-Pinned Beam

3.2 Noncollocated Point Actuator-Sensor Pairs

In this section, the noncollocated point actuator-sensor transfer functions are considered. As in Chapter 2 the dereverberated transfer function determines the general behavior of the analytical transfer function. Knowing the dereverberated transfer function allows for an estimate of the crossover frequency and rate of rolloff of the analytical transfer function. The procedure of Section 2.3 is used to find the dereverberated transfer function for the noncollocated point actuator-sensor pair. The transfer function is then compared to the collocated case, and a quantitative measure of how the transfer function is affected by the noncollocation is discussed.

Figure 3.4 shows a pinned-pinned beam with a noncollocated point actuator-sensor pair, where the actuator is centered on the beam and the sensor is x_s from the actuator. The pinned end conditions are chosen due to the simplicity of the associated modeshapes. There are two transfer functions for this beam: x_s is positive, i.e. the sensor is to the right of the actuator, and x_s is negative, i.e. the sensor is to the left of the actuator.

The analytical actuator to sensor transfer function when $x_s \geq 0$ is

$$\begin{aligned} \frac{y_{\mathrm{pn}}}{u_{\mathrm{p}}} &= \frac{w(x_s, t)}{F} \\ G &= \frac{1}{4EIk^3\left(\cos(\frac{kl}{2})(e^{\frac{1}{2}kl} + e^{-\frac{1}{2}kl})\right)} \end{aligned} \tag{3.11}$$

$$\begin{aligned} \frac{y_{\mathrm{pn}}}{u_{\mathrm{p}}} = G\Bigg[& \cos(kx_s)\left(\sin\left(\frac{kl}{2}\right)\left(-e^{\frac{1}{2}kl} - e^{-\frac{1}{2}kl}\right)\right) \\ & + \sin(kx_s)\left(\cos\left(\frac{kl}{2}\right)\left(e^{\frac{1}{2}kl} + e^{-\frac{1}{2}kl}\right)\right) \\ & + \cos\left(\frac{kl}{2}\right)\left(e^{\frac{1}{2}kl}e^{-kx_s} - e^{-\frac{1}{2}kl}e^{kx_s}\right)\Bigg] \end{aligned} \tag{3.12}$$

When $x_s \leq 0$, the analytical transfer function is

$$\begin{aligned} \frac{y_{\mathrm{pn}}}{u_{\mathrm{p}}} = G\Bigg[& \cos(kx_s)\left(\sin\left(\frac{kl}{2}\right)\left(-e^{\frac{1}{2}kl} - e^{-\frac{1}{2}kl}\right)\right) \\ & + \sin(kx_s)\left(\cos\left(\frac{kl}{2}\right)\left(-e^{\frac{1}{2}kl} - e^{-\frac{1}{2}kl}\right)\right) \\ & + \cos\left(\frac{kl}{2}\right)\left(e^{\frac{1}{2}kl}e^{kx_s} - e^{-\frac{1}{2}kl}e^{-kx_s}\right)\Bigg] \end{aligned} \tag{3.13}$$

Substituting $x = 0$ into these two equations results in Equation 2.29, the collocated transfer function.

Table 3.2 shows the different values of the asymptotes of the dereverberated transfer function when the actuator is placed at different points on the beam and x_s is positive. Table 3.3 shows the different values of the asymptotes of the dereverberated transfer function when the actuator is placed at different points on the beam and x_s is negative. $\mathcal{T}_{\mathrm{RtLow}}$ and $\mathcal{T}_{\mathrm{RtHigh}}$ are the asymptotes when x_s is positive, and $\mathcal{T}_{\mathrm{LtLow}}$ and $\mathcal{T}_{\mathrm{LtHigh}}$ are the asymptotes when x_s is negative. Note that if $x_s = 0$, then the value

Table 3.2: Low and High Frequency Asymptotes for Different Placement of Point Actuator and Noncollocated Point Sensor; x_s Is Positive

Position	$\mathcal{T}_{\text{RtLow}}$	$\mathcal{T}_{\text{RtHigh}}$
$\frac{l}{2}$	$\frac{l^3+4x_s^3-6lx_s^2}{48EI}$	$\frac{1}{4EIk^3}$
$\frac{l}{4}$	$\frac{9l^3+24l^2x_s-72lx_s^2+32x_s^3}{768EI}$	$\frac{1}{4EIk^3}$
$\frac{l}{10}$	$\frac{81l^3-1350lx_s^2+500x_s^3+720l^2x_s}{30000EI}$	$\frac{1}{4EIk^3}$
$\frac{l}{25}$	$\frac{1152l^3+15625x_s^3+27600l^2x_s-45000lx_s^3}{2343750EI}$	$\frac{1}{4EIk^3}$

Table 3.3: Low and High Frequency Asymptotes for Different Placement of Point Actuator and Noncollocated Point Sensor; x_s Is Negative

Position	$\mathcal{T}_{\text{LtLow}}$	$\mathcal{T}_{\text{LtHigh}}$
$\frac{l}{2}$	$\frac{l^3-4x_s^3-6lx_s^2}{48EI}$	$\frac{1}{4EIk^3}$
$\frac{l}{4}$	$\frac{3l^3+8l^2x_s-24lx_s^2+32x_s^3}{256EI}$	$\frac{1}{4EIk^3}$
$\frac{l}{10}$	$\frac{-27l^3-450lx_s^2+1500x_s^3+240l^2x_s}{10000EI}$	$\frac{1}{4EIk^3}$
$\frac{l}{25}$	$\frac{192l^3+62500x_s^3+4600^2x_s-7496lx_s^3}{390625EI}$	$\frac{1}{4EIk^3}$

of the low asymptote is equal to the collocated low asymptote found in Table 2.1.

The high frequency asymptote is $\mathcal{T}_{\text{High}} = \frac{1}{4EIk^3}$ for the noncollocated case regardless of actuator position, which is *lower* than the high frequency asymptote for the collocated case, $\mathcal{T}_{\text{High}} = \frac{1}{2EIk^3}$. This small shift down occurs due to the effect of the evanescent waves between the actuator and sensor.

Two facts about the noncollocated point actuator-sensor pair are notable: the first is that the point actuator-sensor pair, regardless of their proximity to each other, will roll off as a function of k^{-3}. Second, only in the case of analytically perfect collocation

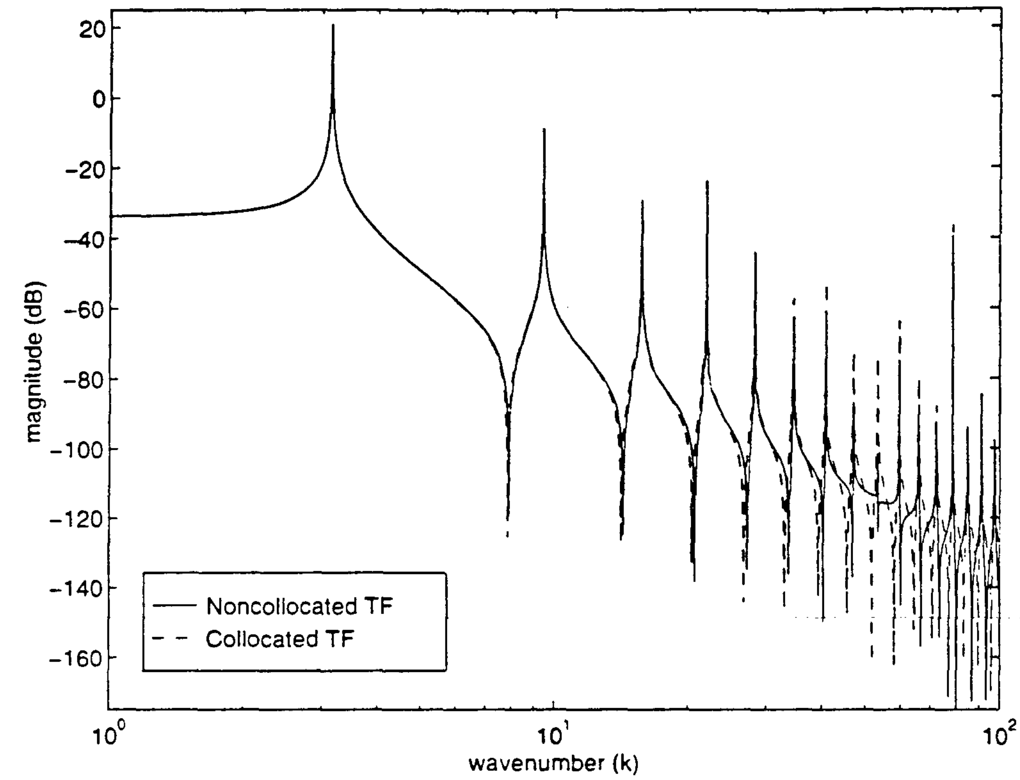

Figure 3.5: Transfer Functions for Collocated and Noncollocated Point Actuator-Sensor Pairs on a Pinned-Pinned Beam

is $\mathcal{T}_{\text{High}} = \frac{1}{2EIk^3}$. Even an infinitesimal degree of noncollocation will cause the change to $\mathcal{T}_{\text{High}} = \frac{1}{4EIk^3}$.

Figure 3.5 shows the analytical transfer functions of a collocated point actuator-sensor pair centered on a pinned-pinned beam and a noncollocated point actuator-sensor pair with the actuator at the center and the sensor is offset by 3% of the beam length, i.e. $x_s = 0.03l$. Note how the two match very closely until the noncollocated transfer function loses a zero at $k \approx 50$. This is the wavenumber of noncollocation,i.e. $k_{\text{non}} \approx 50$, where the wavenumber is sufficiently large that the deflection at the location of the sensor and the deflection at the location of the actuator have opposite signs. This is shown in Figure 3.6, where $\times$ is the position of the actuator and $\circ$ is

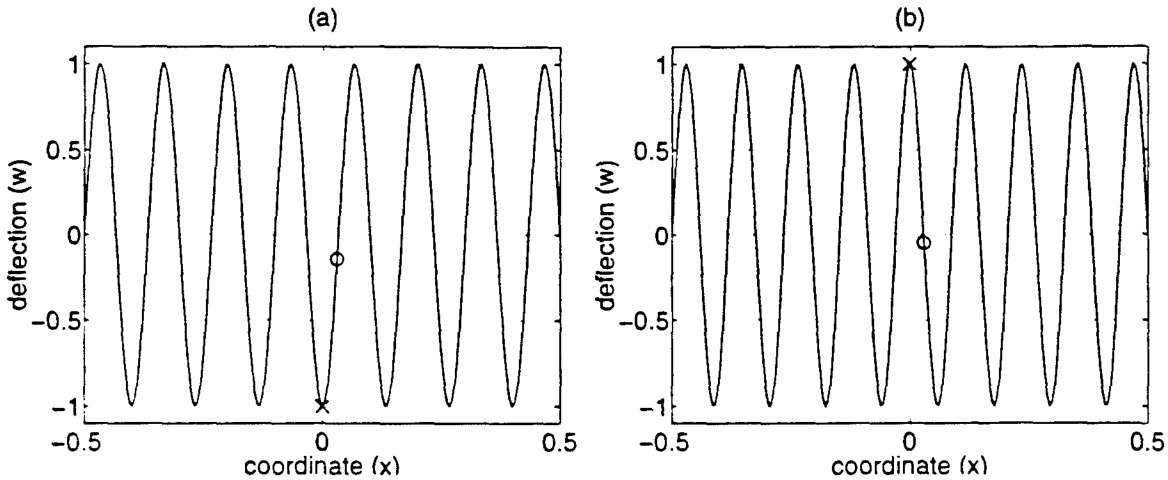

Figure 3.6: Pinned-Pinned Modeshapes for Beam of Length $l = 1$ (a) 15th Mode and (b) 17th Mode

the position of the sensor.

Also, when the actuator is in the center of a pinned-pinned beam, symmetry allows for an analytical expression relating the wavenumber of noncollocation, k_{non}, and the distance from the actuator to the sensor, x_s.

$$k_{\text{non}} = \frac{\pi}{2|x_s|} \tag{3.14}$$

For the preceding example, where $x_s = 0.03l$, the wavenumber of noncollocation is $k_{\text{non}} \approx 52.36$, which correlates with Figure 3.5.

Thus, at the wavenumber of noncollocation the transfer function has its first missing zero, and the high frequency asymptote changes from the collocated value to the noncollocated value. Figure 3.7 illustrates this point with the noncollocated transfer function of Figure 3.5 with the low asymptote, collocated high asymptote, and noncollocated high asymptote.

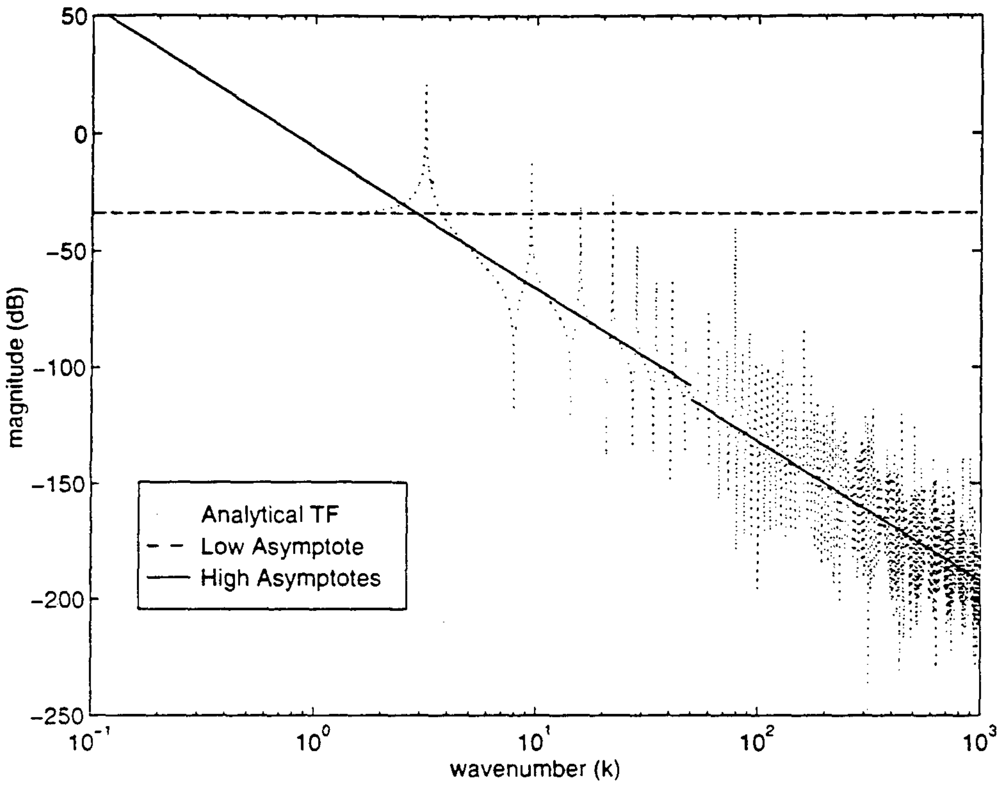

Figure 3.7: Analytical and Dereverberated Transfer Functions for Noncollocated Point Actuator-Sensor Pair on a Pinned-Pinned Beam

3.3 Noncollocated Shaped Actuator-Sensor Pairs

In this section, noncollocated transfer functions for rectangular and triangular actuator-sensor pairs are considered. The aspect of noncollocation is limited to a sensor of different length than the actuator; the centroid of the actuator-sensor pair remains collocated. Two cases are considered for each shape: in the first the sensor is shorter than the actuator, and in the second the sensor is longer than the actuator. The dereverberated transfer functions for both shapes are determined and compared to the collocated results of Chapter 2. Also, an investigation is conducted to determine the most reasonable and best performing actuator and sensor lengths.

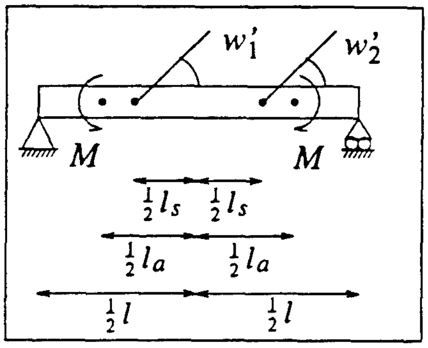

(a)

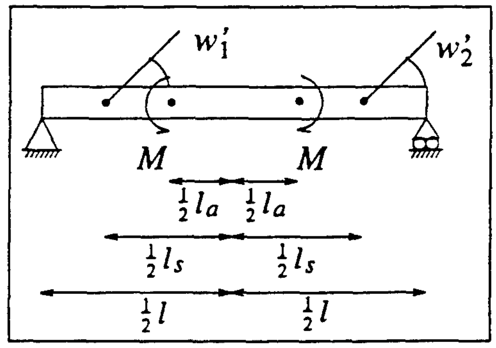

(b)

Figure 3.8: Noncollocated Rectangular Actuator-Sensor Pair (a) Sensor Shorter than Actuator (b) Sensor Longer than Actuator

Table 3.4: Low and High Frequency Asymptotes for Noncollocated Rectangular Actuator-Sensor Pairs on a Pinned-Pinned Beam

	$\mathcal{T}_{\text{RLow}}$	$\mathcal{T}_{\text{RHigh}}$
$l_s < l_a$	$\frac{l_s}{EI}$	$\frac{1}{EIk}$
$l_s > l_a$	$\frac{l_a}{EI}$	$\frac{1}{EIk}$

3.3.1 Rectangular Actuator-Sensor Pairs

Figure 3.8(a) shows a rectangular actuator-sensor pair where the sensor is shorter than the actuator, and Figure 3.8(b) shows a rectangular actuator-sensor pair where the sensor is longer than the actuator. The duality of the actuator-sensor pair is such that if $l_a = x$ and $l_s = y$, the transfer function is identical when $l_a = y$ and $l_s = x$.

The procedure of Section 2.3 is used to find the dereverberated transfer function for the noncollocated rectangular actuator-sensor pair. The dereverberated transfer function is determined for both cases shown in Figure 3.8 and for varying actuator placement. Table 3.4 shows the values of the low and high frequency asymptotes when the sensor is longer than the actuator and when the sensor is shorter than the

actuator. These asymptotes hold regardless of the position of the actuator on the pinned-pinned beam.

Note that if $l_s = l_a$, then the value of the low asymptote is equal to the collocated low asymptote in Equation 2.37. Also, the noncollocated low asymptote is actually controlled by the smaller of the two dimensions l_s and l_a. The most important observation, however, is that for a rectangular actuator-sensor pair, regardless of the placement on the beam or their relative size, the rolloff will be a function of k^{-1}.

The contrast in the noncollocated rectangular actuator-sensor pair is of the same form as the point case; there is a difference in high frequency asymptotes between the collocated and noncollocated cases. The high frequency asymptote for the noncollocated case is $\mathcal{T}_{\mathrm{RNHigh}} = \frac{1}{EIk}$ regardless of actuator position or sensor size, while the high frequency asymptote for the collocated case is $\mathcal{T}_{\mathrm{RHigh}} = \frac{1}{2EIk}$. This means that the noncollocated transfer function actually shifts *upward*, unlike the case of the noncollocated point actuator-sensor pair. The magnitude lowering effect from the evanescent waves is not as strong as the magnitude rising effect due to the numerous missing zeros in the transfer function. Therefore, the transfer function shifts upward.

Since the transfer function follows the noncollocated high asymptote due to the occurrence of many missing zeros, a very noncollocated case will show the shift upward more effectively. For visual purposes, an extreme case is shown in Figure 3.9, where the actuator is centered on the beam and $l_s = 0.5l$ and $l_a = 0.05l$.

In an effort to quantify the effects of length noncollocation on the transfer function of a rectangular actuator-sensor pair on a pinned-pinned beam, Figure 3.10 shows the pole-zero patterns when $l_a = 0.2l$ and the value of l_s varies such that the ratio of $l_s : l_a$ is the value on the horizontal axis. Figure 3.11 is a similar plot; however, $l_a = 0.4l$ in this case. These plots show no consistent, quantifiable change in the pole-zero spacing

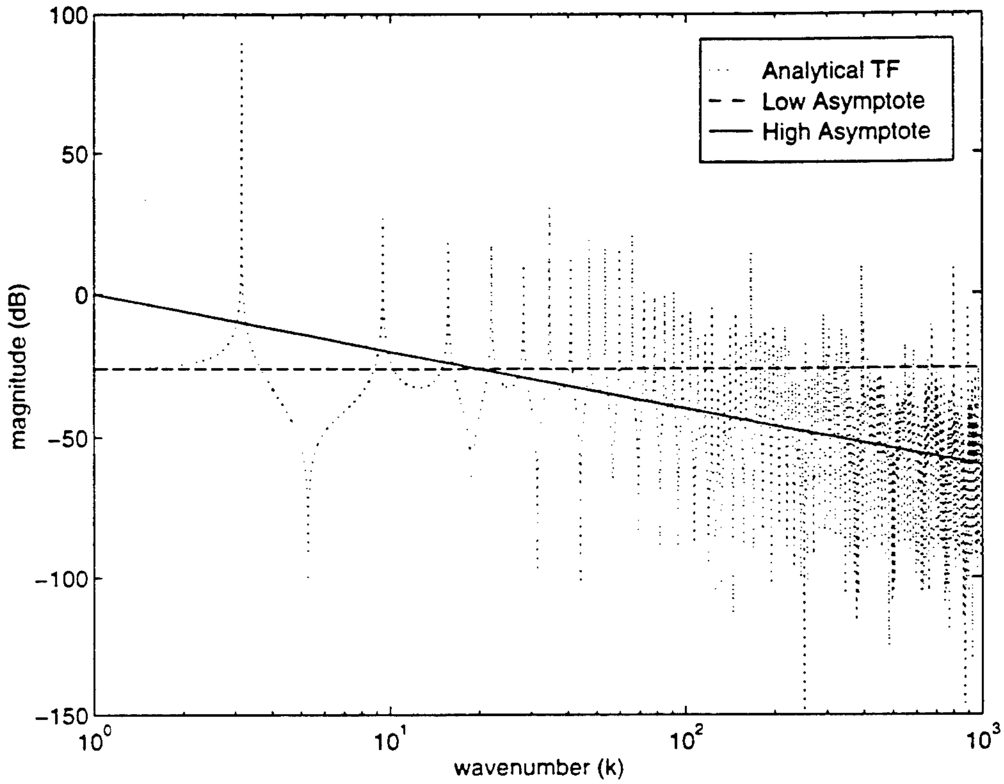

Figure 3.9: Analytical and Dereverberated Transfer Functions for Noncollocated Rectangular Actuator-Sensor Pair on a Pinned-Pinned Beam; $l_s = 0.5l$, $l_a = 0.05l$

with a small difference in the sensor length. However, both of these plots show that a missing zero occurs fairly early when the actuator and sensor are not of the same dimension. As the difference between length of actuator and sensor increases, the wavenumber of the first missing zero in the noncollocated transfer function decreases. The rule of thumb stated in Equation 3.14 can be used as a rough estimate for the wavenumber of noncollocation. However, the rule is not as accurate as it is for a point actuator-sensor pair. This implies that there is little room for error in manufacturing if an actual rectangular actuator-sensor pair is expected to produce a collocated transfer function to a reasonably high frequency.

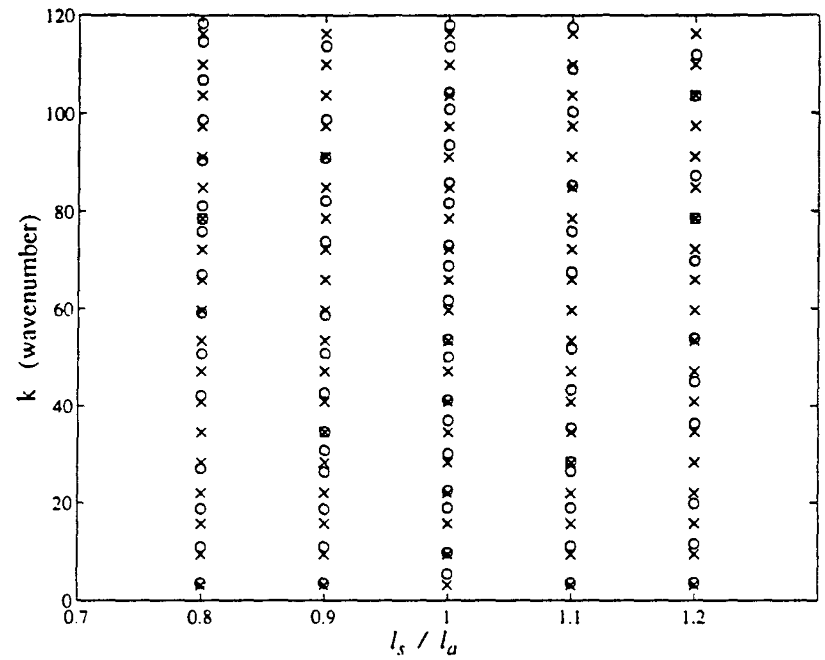

Figure 3.10: Pole-Zero Spacing for Rectangular Actuator to Sensor Transfer Functions; $l_a = 0.2$

3.3.2 Triangular Actuator-Sensor Pairs

The steps followed to analyze the noncollocated rectangular actuator-sensor pair are now used to analyze the noncollocated triangular actuator-sensor case. Figure 3.12(a) shows a triangular actuator-sensor pair where the sensor is shorter than the actuator, and Figure 3.12(b) shows a triangular actuator-sensor pair where the sensor is longer than the actuator. As in the rectangular case, the duality of the triangular actuator-sensor pair is such that if $l_a = x$ and $l_s = y$, the transfer function is identical when $l_a = y$ and $l_s = x$.

As before, the procedure of Section 2.3 is used to find the dereverberated transfer function for the noncollocated triangular actuator-sensor pair. The dereverberated

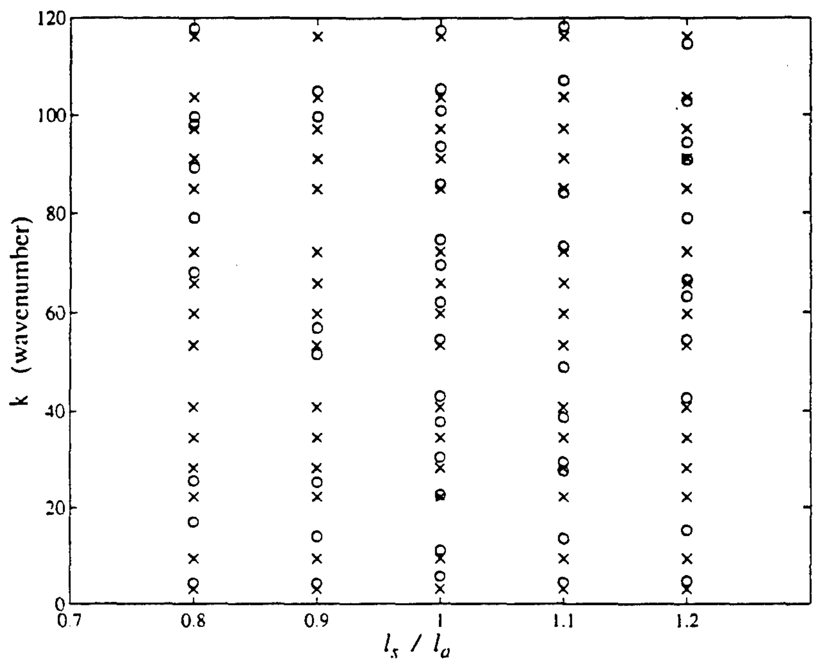

Figure 3.11: Pole-Zero Spacing for Rectangular Actuator to Sensor Transfer Functions; $l_a = 0.4$

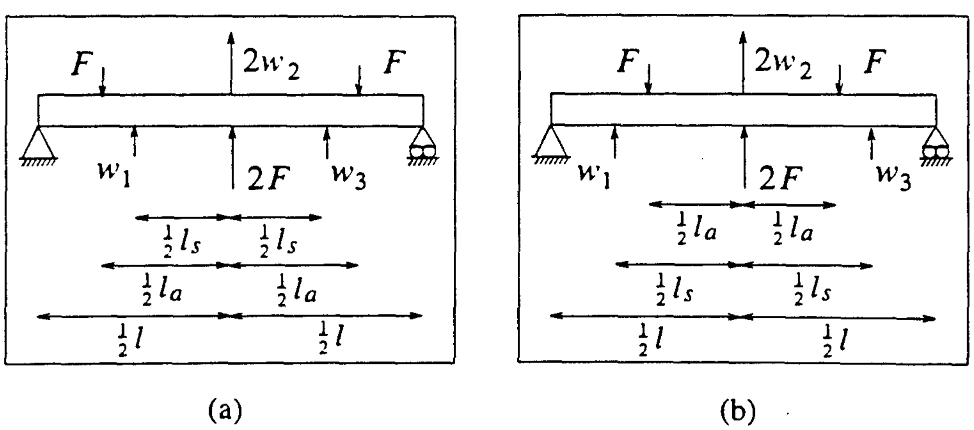

Figure 3.12: Noncollocated Triangular Actuator-Sensor Pair (a) Sensor Shorter than Actuator (b) Sensor Longer than Actuator

Table 3.5: Low and High Frequency Asymptotes for Noncollocated Triangular Actuator-Sensor Pairs on a Pinned-Pinned Beam

	$\mathcal{T}_{\text{TLow}}$	$\mathcal{T}_{\text{THigh}}$
$l_s < l_a$	$\frac{l_s^2(l_s - 3l_a)}{24EI}$	$\frac{1}{EIk^3}$
$l_s > l_a$	$\frac{l_a^2(l_a - 3l_s)}{24EI}$	$\frac{1}{EIk^3}$

transfer function is determined for the two cases shown in Figure 3.12 and for varying actuator placement. Table 3.5 shows the values of the analytical dereverberated asymptotes when the sensor is longer than the actuator and when the sensor is shorter than the actuator. Barring any singularities, the asymptotes in this table are independent of the position of the actuator on the pinned-pinned beam.

It is observed from this table that when $l_s = l_a$, the value of the low frequency asymptote is equal to the collocated low frequency asymptote, as in Equation 2.40. As in the rectangular case, the noncollocated low asymptote is actually dominated by the smaller of l_s and l_a. Also, the rolloff of a triangular actuator-sensor pair, regardless of their placement on the beam or their relative size, will roll off as a function of k^{-3}.

The high frequency asymptote for the noncollocated triangular actuator-sensor pair is $\mathcal{T}_{\text{RNHigh}} = \frac{1}{EIk^3}$, regardless of actuator position or sensor size. The high frequency asymptote for the collocated case is $\mathcal{T}_{\text{RHigh}} = \frac{5}{2EIk^3}$. Figure 3.13 shows the transfer function and dereverberated asymptotes for a noncollocated triangular actuator-sensor pair on a pinned-pinned beam where the actuator is centered on a pinned-pinned beam, $l_a = 0.2l$, and $l_s = 0.4l$.

The high asymptote *drops* by a factor of 2.5 in comparison to the collocated case, yet in the rectangular case, the noncollocated high frequency asymptote was higher than the collocated high frequency asymptote. This magnitude lowering effect is

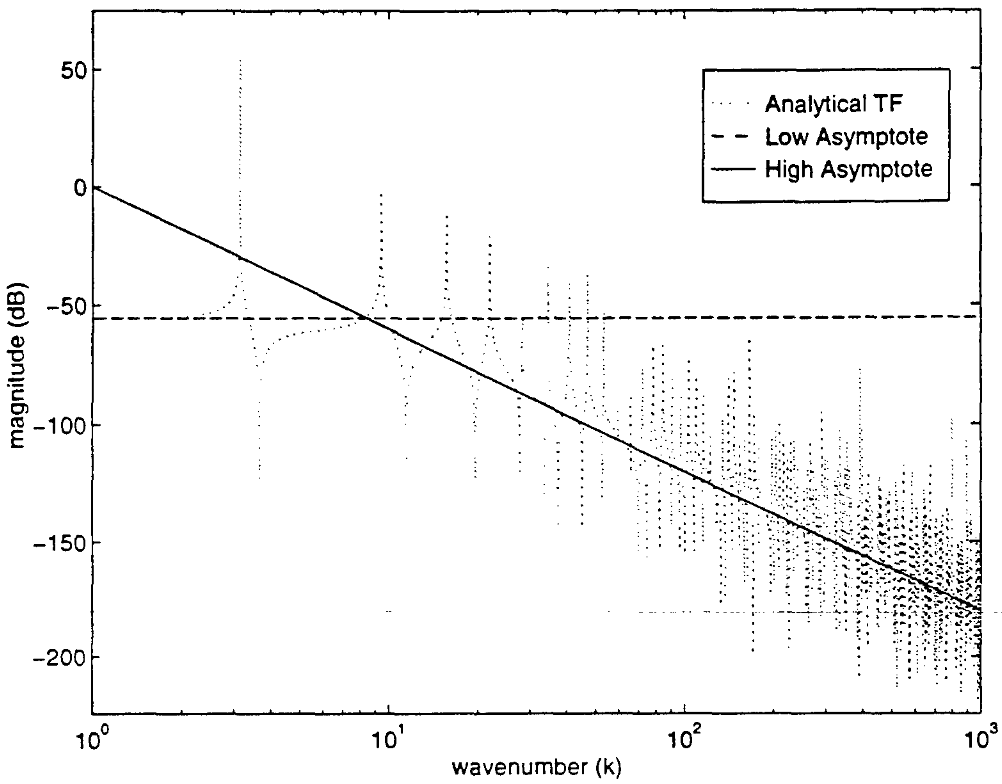

Figure 3.13: Analytical and Dereverberated Transfer Functions for Noncollocated Triangular Actuator-Sensor Pair on a Pinned-Pinned Beam

due to the evanescent waves across the actuator-sensor pair and the fact that, for length noncollocation, the triangular actuator to sensor transfer function maintains an interlaced pole-zero pattern.

To quantify the effects of length noncollocation on the transfer function for a triangular actuator-sensor pair on a pinned-pinned beam, Figure 3.14 shows the pole-zero patterns when $l_a = 0.2l$ and the value of l_s varies such that the ratio of $l_s : l_a$ is the value on the horizontal axis. Unlike the rectangular case, there seems to be a pattern in the pole-zero spacing. As the length of the sensor increases, the wavenumber at which the zero first nears the frequency of the next pole decreases. For example,

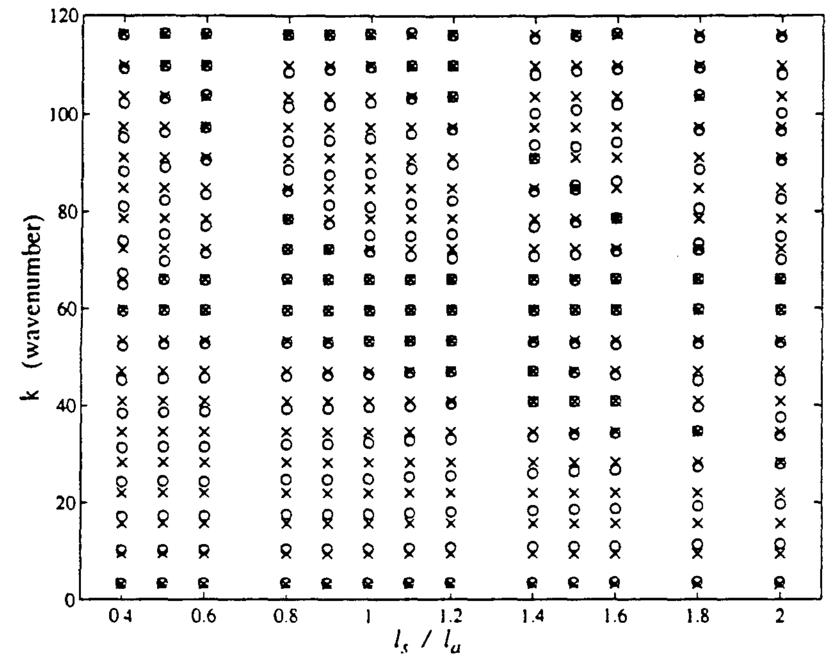

Figure 3.14: Pole-Zero Spacing for Triangular Actuator to Sensor Transfer Functions; $l_a = 0.2$

when $\frac{l_s}{l_a} = 1$, this occurs near $k = 50$, while for $\frac{l_s}{l_a} = 1.4$, this occurs near $k = 40$.

Figure 3.14 also implies that an actuator-sensor pair can be designed to have close zero-pole spacing at specific wavenumbers. Figure 3.15 demonstrates this by plotting a collocated actuator to sensor transfer function, where $l_a = l_s = 0.2l$, and a noncollocated transfer function, where $l_a = 0.2l$ and $l_s = 0.3l$. The static response of the two transfer functions is normalized to 0 dB in order to see the magnitude reduction of the noncollocated transfer function. In addition to this decrease in magnitude due to noncollocation, it is possible to see the close zero-pole spacing between $k = 40$ and $k = 70$. If damping were added to these closely spaced modes, the transfer function would lose even more magnitude.

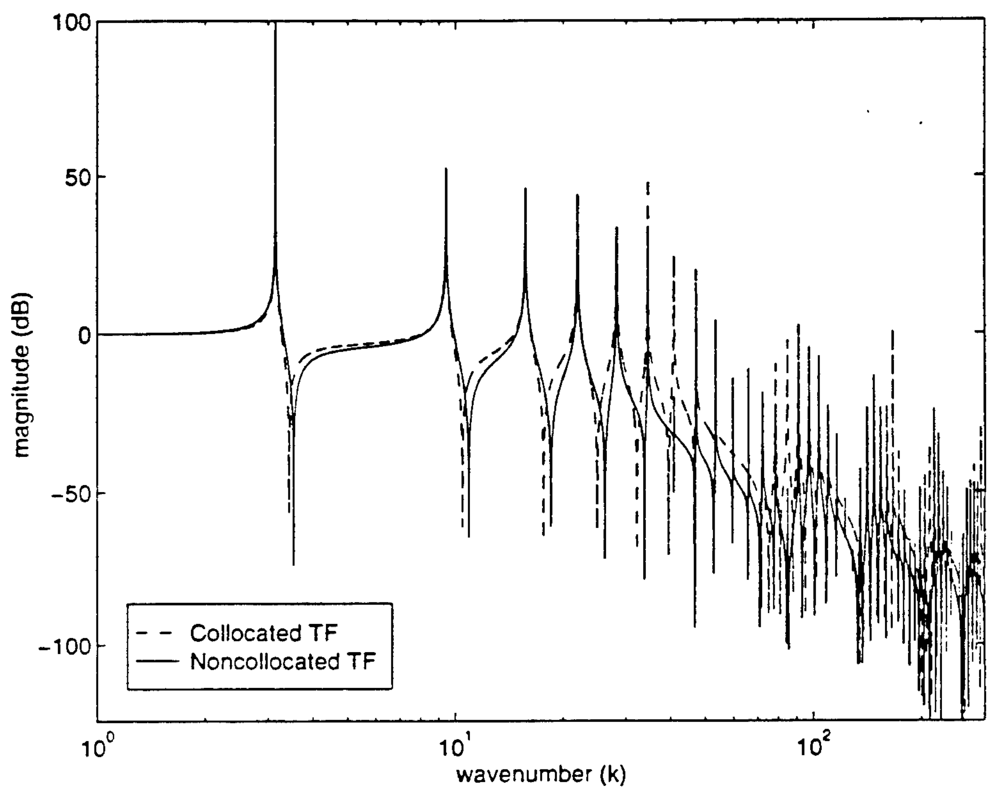

Figure 3.15: Collocated and Noncollocated Transfer Function for Triangular Actuator-Sensor Pair on Pinned-Pinned Beam

The alternating pole-zero pattern is usually associated with a collocated actuator to sensor transfer function, while a missing zero is usually associated with a noncollocated actuator-sensor pair. However, in the case of a triangular actuator-sensor pair, if the centroid remains collocated and the lengths are different, an alternating pole-zero pattern will remain, regardless of the difference in length. When the strain across the beam is $\cos(kx)$, the output of the triangular sensor, in relation to the point at the center, is $\frac{\sin^2(k)}{k^2}$. This function is shown in Figure 3.16. Thus, the shape of the window requires the sign of the input to be the same as the sign of the output. This means that there will be no sign changes in the modal residues of the transfer functions, which implies that there is an alternating pole-zero pattern, regardless of

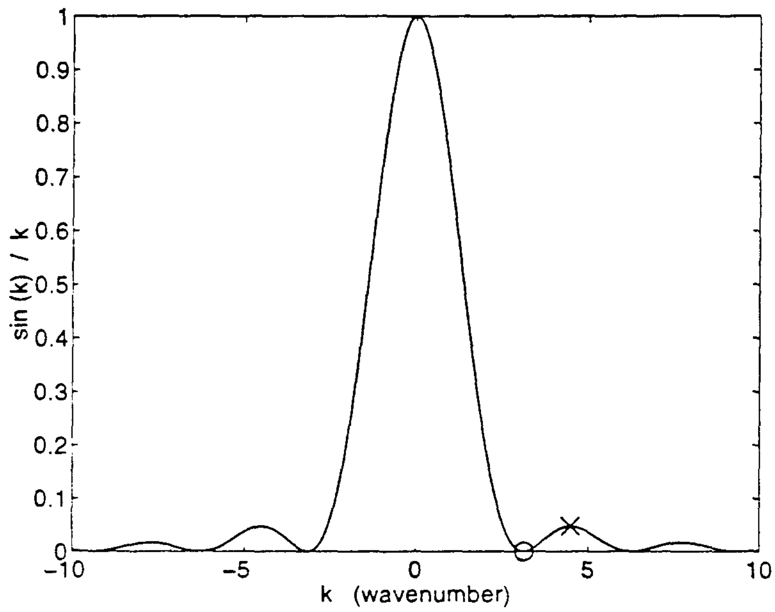

Figure 3.16: Function for Triangular Sensor and Actuator Output

the difference in length between actuator and sensor.

Therefore, an investigation can be held to determine the best size of sensor and actuator. Using Figure 3.16 as a guide, the most effective difference in length for the actuator-sensor pair would use the local minimum of the sensor, designated with by o, to be at the local maximum of the actuator, designated with an by $\times$. This should allow for several near pole-zero cancellations in the transfer function, which, when damping is added, would minimize the magnitude contribution of these modes. The first local minimum can be found by setting the function equal to zero and solving it.

$$\begin{aligned} 0 &= \frac{\sin^2(k_1)}{k_1^2} \\ k_1 &= \pi \end{aligned} \tag{3.15}$$

The first local maximum is found by solving the equation

$$\begin{aligned} 0 &= \frac{d}{dk_2}\frac{\sin^2(k_2)}{k_2^2} \\ k_2 &= \tan(k_2) \\ k_2 &= 4.4934 \end{aligned} \tag{3.16}$$

This implies that for the most effective results, the ratio is

$$\frac{l_s}{l_a} = \frac{k_2}{k_1} = 1.43 \tag{3.17}$$

Figure 3.14 confirms this, since the pole-zero spacing at $\frac{l_s}{l_a} = 1.4$ has five near pole-zero cancellations. At $\frac{l_s}{l_a} = 1.5$, the spacing between the eighth zero and the ninth pole is increased. Also, as the length of the sensor nears twice the length of the actuator, the spacing increases, and the large band of near pole-zero cancellations splits. At this point, adding damping will not be as effective. Finally, it should be noted that as the actuator becomes a smaller percentage of the beam length, the close pole-zero spacing occurs at a higher wavenumber, which means that the property of close pole-zero spacing becomes less useful.

3.4 Discussion

This chapter has discussed the modelling of noncollocated point, rectangular, and triangular actuator-sensor pairs on pinned-pinned Bernoulli-Euler beams. The dereverberated transfer functions for each pair were determined and compared to the collocated case. In each case, the high frequency rolloff was shown to be of the same power of k as the corresponding collocated case. This implies that regardless of beam

end conditions, collocation or length noncollocation, the transfer function rolloff in k is known by the type of actuator-sensor pair.

Different actuator-sensor pairs were shown to impact different design parameters. A relation was found between the wavenumber of noncollocation and the distance between point actuator and point sensor. It was also shown that the point actuator to sensor transfer function follows the noncollocated high frequency asymptote after the first missing zero in the transfer function.

The rectangular actuator-sensor is very sensitive to length noncollocation. With very little percentage difference in actuator and sensor length, a missing zero appears in the transfer function. Also, there is an increase in the noncollocated high frequency asymptote which is accounted for by the numerous missing zeros in the noncollocated transfer functions.

Finally, the noncollocated triangular actuator-sensor pair was compared to the collocated pair. There are no missing zeros in the length noncollocated triangular actuator to sensor transfer function, which allows for use of the noncollocated transfer function to obtain a small amount of additional gain margin without phase loss. If the ratio $\frac{l_s}{l_a} = 1.43$, then there will be a region of near pole-zero cancellations within the transfer function. If damping is added to the transfer function, then at the wavenumber of the near pole-zero cancellation, there will be little response, and additional gain margin can be obtained. This analysis can be used to determine the best design for an actuator-sensor pair to be placed upon a real structure.

Chapter 4

Collocated Shaped Actuator-Sensor Pairs in Realistic Geometries

The transfer functions derived in Chapter 2 showed the analytical results for a Bernoulli-Euler beam with modelled actuator inputs and sensor outputs. However, these models eliminated the effects of the finite thickness of the actuators and sensors, as well as the finite widths of the beam and the actuators. This chapter investigates the transfer functions for a rectangular actuator-sensor pair and a triangular actuator-sensor pair when these effects are included.

4.1 Rectangular Actuator-Sensor Pair

This section examines the influence of applying a rectangular piezoceramic actuator-sensor pair to a cantilevered steel beam. Various models are generated to determine the different effects of increased actuator thickness and of finite beam width upon the actuator to sensor transfer function.

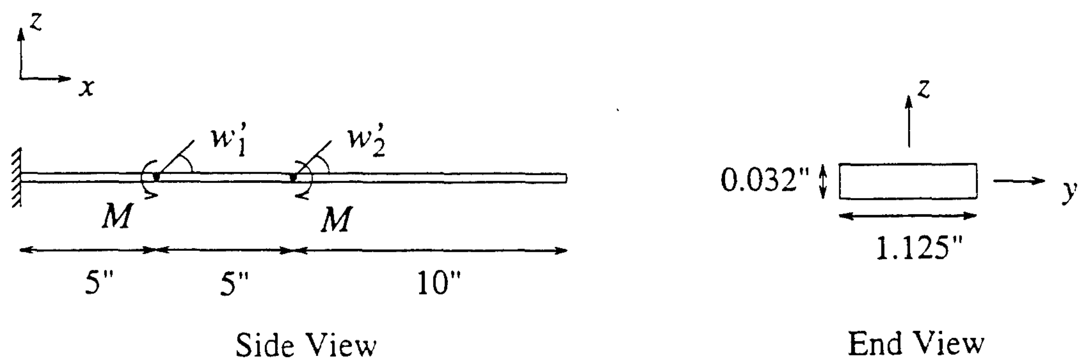

Figure 4.1: Cantilevered Steel Beam with Rectangular Actuator-Sensor Pair of Zero Thickness

4.1.1 Analytical Wave Model

First, the analytical transfer function is found for the example beam using the wave solution technique of Section 2.2.3. The analytical dereverberated transfer function is then determined using the results in Equation 2.37 and Equation 2.38. Figure 4.1 is a diagram of the steel, cantilever beam that is 20 inches long, 1.125 inches wide, and 0.032 inches thick. In metric units, this is 508mm×28.575mm×0.8128mm. The modulus of elasticity for steel is $E_s = 2.05 \times 10^{11}\mathrm{N/m^2}$ and the density is $\rho_s = 7860\mathrm{kg/m^3}$. Figure 4.2 shows the analytical transfer function and dereverberated asymptotes for this case. Note the magnitude of the transfer function has units of rad/N-m.

This solution technique neglects the mass and stiffness of the actuator and the finite width of the beam and actuator. Also, since this analytical model includes no damping, the actual magnitude of the transfer function at the frequencies of the poles is ∞ dB, and the actual magnitude of the transfer function at the frequencies of the zeros is $-\infty$ dB. The poles and zeros shown in Figure 4.2 appear to have finite

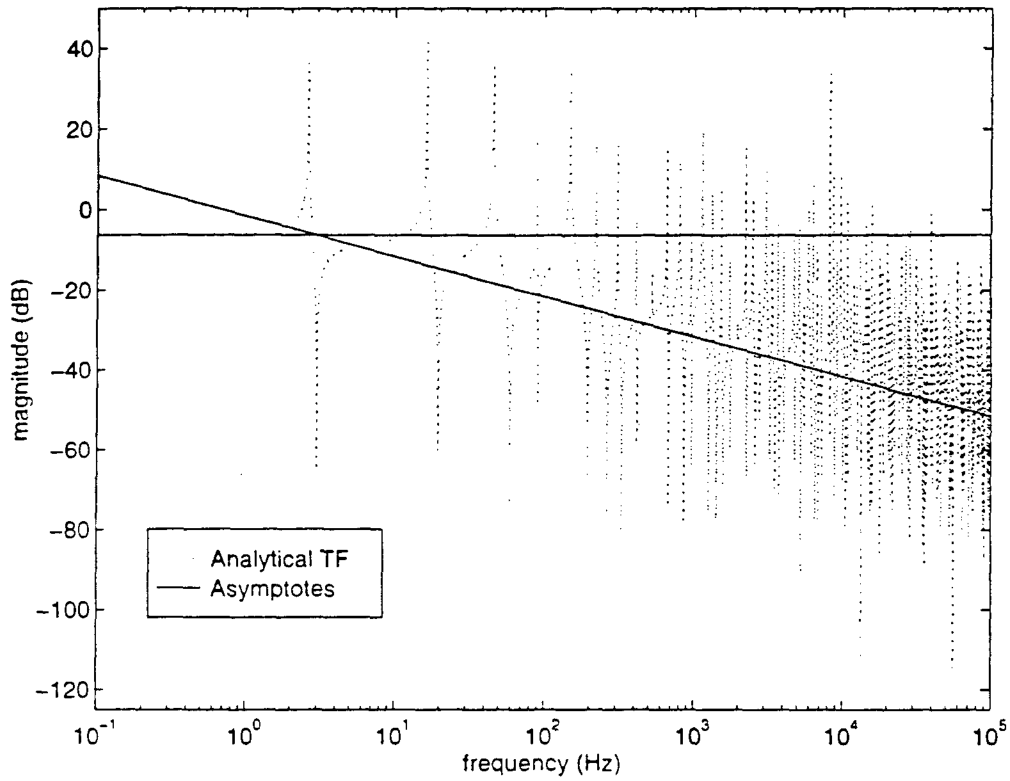

Figure 4.2: Analytical and Dereverberated Transfer Functions for Rectangular Actuator-Sensor Pair on Cantilevered Beam

magnitudes because Matlab^{TM}, the software package used in constructing the figure, evaluates the transfer function at discrete points.

4.1.2 Finite Element Models Using 2-D Beam Elements

As mentioned before, the analytical wave solution neglects actuator mass and stiffness, as well as the finite width of a real beam and actuator. In this section, two-dimensional finite element models are used to determine more accurate models which would match the transfer function of an actual beam. The ANSYS program is chosen to create the finite element models, since the program has the ability to directly model three-

dimensional piezoelectric elements.

The first step to improve upon the analytical model is adding a small amount of damping to the transfer function, such that the magnitudes of the peaks of the transfer function can be compared to each other. A finite element model of the beam in Figure 4.1 is created in ANSYS using two-node, two-dimensional, elastic, symmetric beam elements. The modes of this beam are determined and placed into a state space model, one percent of critical modal damping is added ($\zeta = 0.01$), and the transfer function is generated. Figure 4.3 compares the damped finite element transfer function and the analytical transfer function. These two transfer functions apparently plot exactly except for the magnitudes of the poles and zeros. The transfer function from the finite element model gives insight into the relative magnitudes of the finite peaks of the transfer function, as well as determining a better estimate of the final reverberant crossover frequency.

To find the dereverberated transfer function for the finite element model, the model is critically damped, $\zeta = \frac{\sqrt{2}}{2}$, and the transfer function is determined. This transfer function is then compared to the asymptotes of the analytical dereverberated transfer function found in Equations 2.37 and 2.38. Figure 4.4 shows these two dereverberated transfer functions. The two transfer functions compare favorably, and the fidelity of the finite element model is again confirmed.

Next, the finite thickness of the actuator-sensor pair is included in the model. The piezoceramic actuator is composed of PZT-5A, and the sensor is made of Polyvinylidine Fluoride (PVDF). The modulus of elasticity of the PZT-5A piezoceramic actuator is $E_p = 6.098 \times 10^{10}\mathrm{N/m^2}$ and the density is $\rho_p = 7500\mathrm{kg/m^3}$. The mass and stiffness of the PVDF have very little effect, so they are neglected. This model is shown in Figure 4.5.

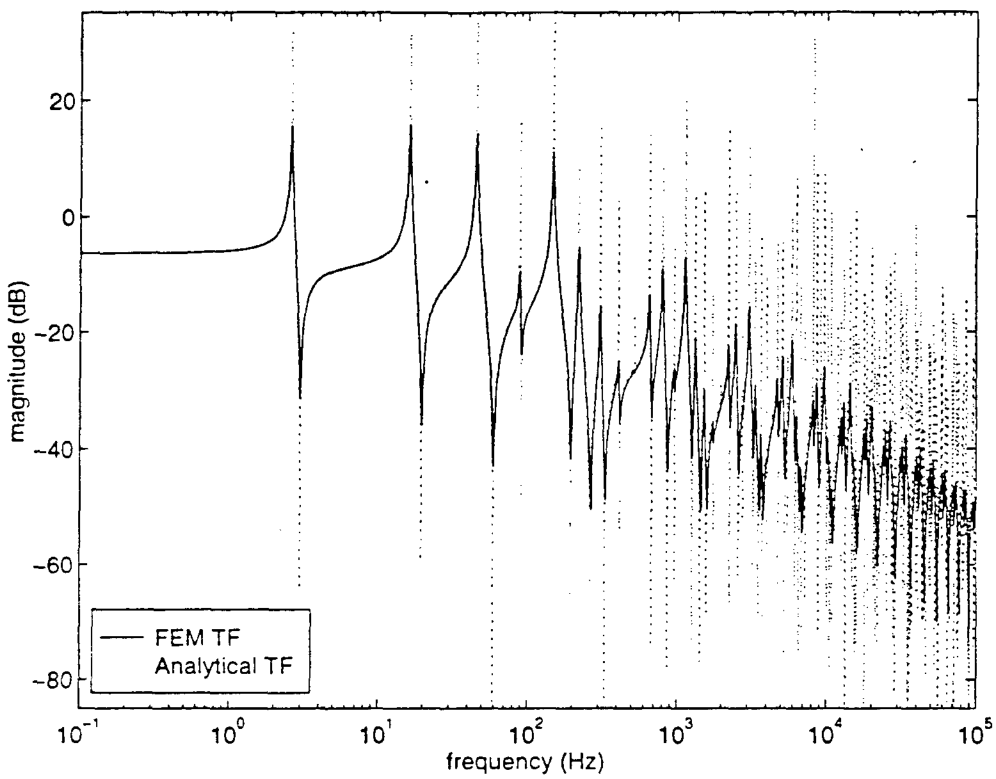

Figure 4.3: Transfer Functions for Rectangular Actuator-Sensor Pair on Cantilevered Beam: Analytical with No Damping, and 2D FE Model with 1% Modal Damping

To maintain symmetry about the beam, a representative actuator thickness is placed on the top and the bottom of the beam. In order to incorporate this thickness, two beam elements types are included within the finite element model. One element type has the properties of the steel beam, as in the first finite element model. The second element type includes the mass and stiffness of the PZT-5A actuators on the top and the bottom of the beam. These two element types are given the proper dimensions, and together they are used to create the finite element model. The transfer function is then found using the previously described technique, and 1% modal damping is added.

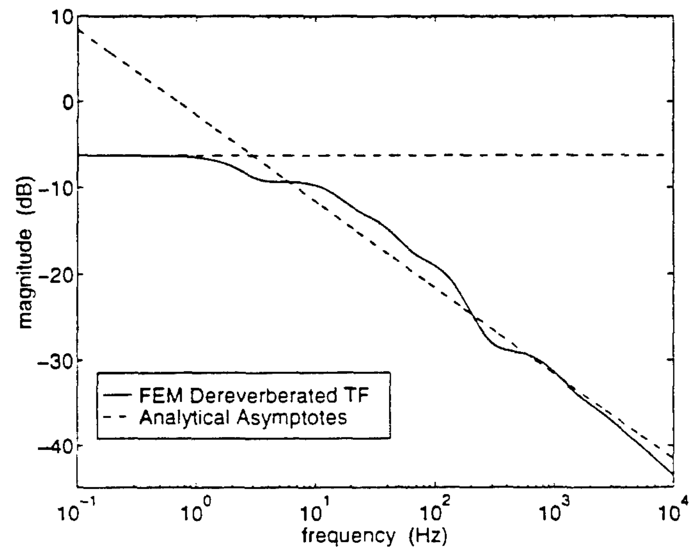

Figure 4.4: Dereverberated Rectangular Actuator to Sensor Transfer Functions for 2D FE Model of Cantilevered Beam with 1% Damping and Analytical Model

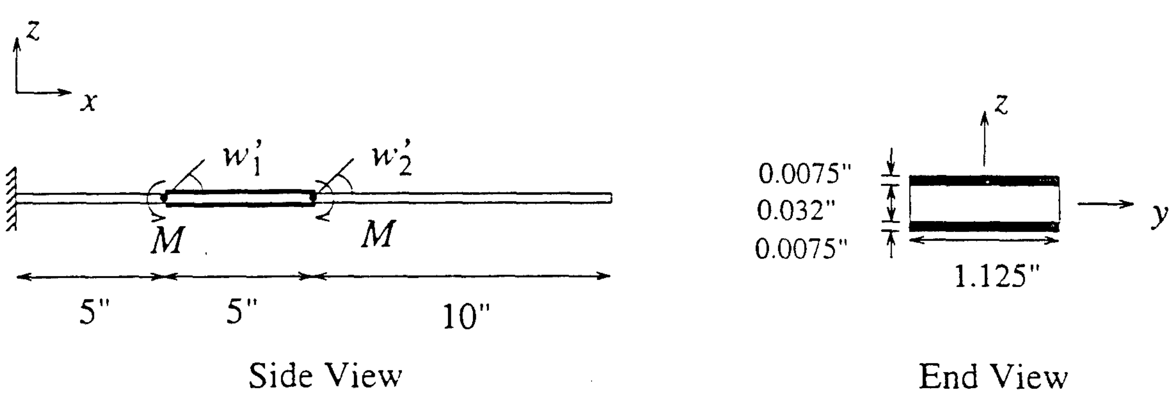

Figure 4.5: Cantilevered Steel Beam with Finite Thickness of Rectangular Actuator

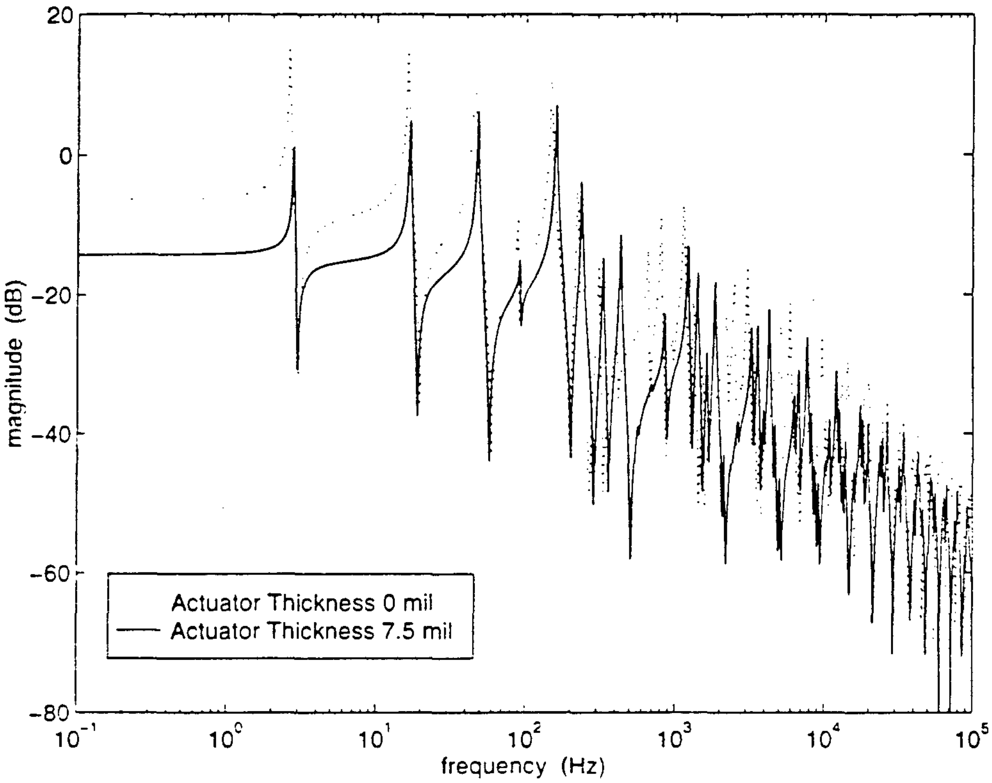

Figure 4.6: Transfer Functions for FE Model with Zero Rectangular Actuator Thickness and with Rectangular Actuator Thickness of 7.5 mil on a Cantilevered Beam

Figure 4.6 is a plot of the actuator to sensor transfer functions of the finite element model without the actuator thickness and the finite element model with the actuator thickness. Note how the increased thickness of the actuator causes the frequencies of the poles to increase, indicating that the stiffness perturbation is more significant than the mass perturbation.

Thus, the question arises: what is the effect of increased actuator thickness upon the actuator to sensor transfer function? Figure 4.7 addresses this question by plotting the dereverberated transfer functions when the actuator thickness on each side of the beam is 0 mils, 7.5 mils, and 15 mils. This plot shows that as the thickness increases,

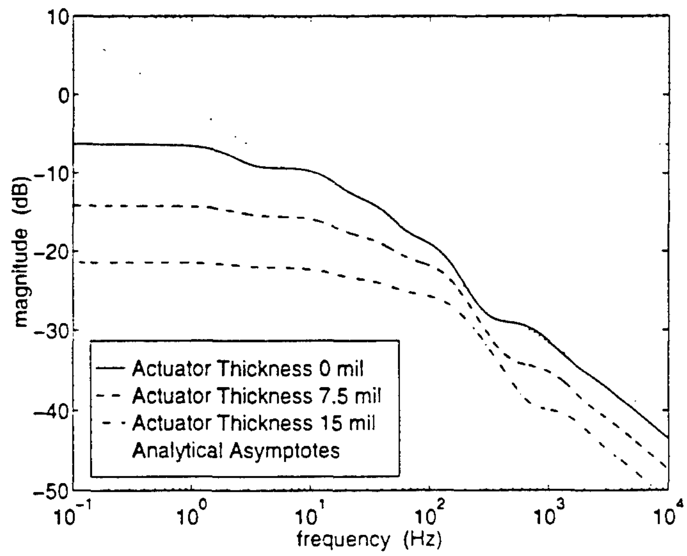

Figure 4.7: Analytical Asymptotes and Dereverberated Transfer Functions for Varying Rectangular Actuator Thickness on Cantilever Beam: 0 mil, 7.5 mil, 15 mil

the beam stiffness increases and the static gain decreases. The transfer function is still rolling off at -10 dB/decade at high frequencies. However, as the actuator thickness increases, the frequency at which the transfer function begins to rolloff increases as well.

To explain this theoretically, the stiffness of the actuator can be modelled as strain feedback. As the gain $\mathcal{K}$ is increased, the frequencies of the closed loop poles move to the frequencies where the undamped open loop zeros cross 0 dB. At very low frequencies, the poles do not move much because they are already very close to the zeros. As the frequency increases, the pole-zero spacing of the open loop transfer function increases, so that the finite actuator thickness has a greater effect. However, at high frequencies, the open loop transfer function has rolled off such that the undamped open loop zeros never cross 0 dB, so the finite thickness does not affect these modes. This means that as the actuator thickness increases, the pole-zero

Figure 4.8: Finite Element Mesh of the Top View of Cantilevered, Steel Beam with Rectangular Actuator

spacing of the transfer function only changes within a small bandwidth near crossover, and the pole-zero spacing does not change at very low or very high frequencies.

4.1.3 Finite Element Model Using 3D Brick Elements

The finite element models presented in the previous subsection improve upon the analytical wave model by adding damping and finite actuator thickness. However, they ignore a major factor in the transfer function that would influence actual behavior in the laboratory: the finite width of the beam and the actuators. In order to model these effects, a finite element model is developed which is composed of three-dimensional,eight-node, brick solid elements, and three-dimensional, eight-node, brick elements with electromechanical coupling. The solid elements are used to model the beam, and the coupled elements are used to model the PZT-5A actuators. The side view and end view of this beam are the same as in Figure 4.5. The beam dimensions are 20 inches$\times$ 1.125 inches$\times$ 0.032 inches. Since this model is three-dimensional, there is now a top and bottom view, which are the same due to the symmetry of the beam. A top view of the finite element mesh of the beam is shown in Figure 4.8. The cantilevered end is on the left, and the actuator is on the portion of the beam which has the finer mesh. The dimensions of the PZT-5A actuators are 5 inches $\times$ 0.75 inches $\times$ 0.0075 inches.

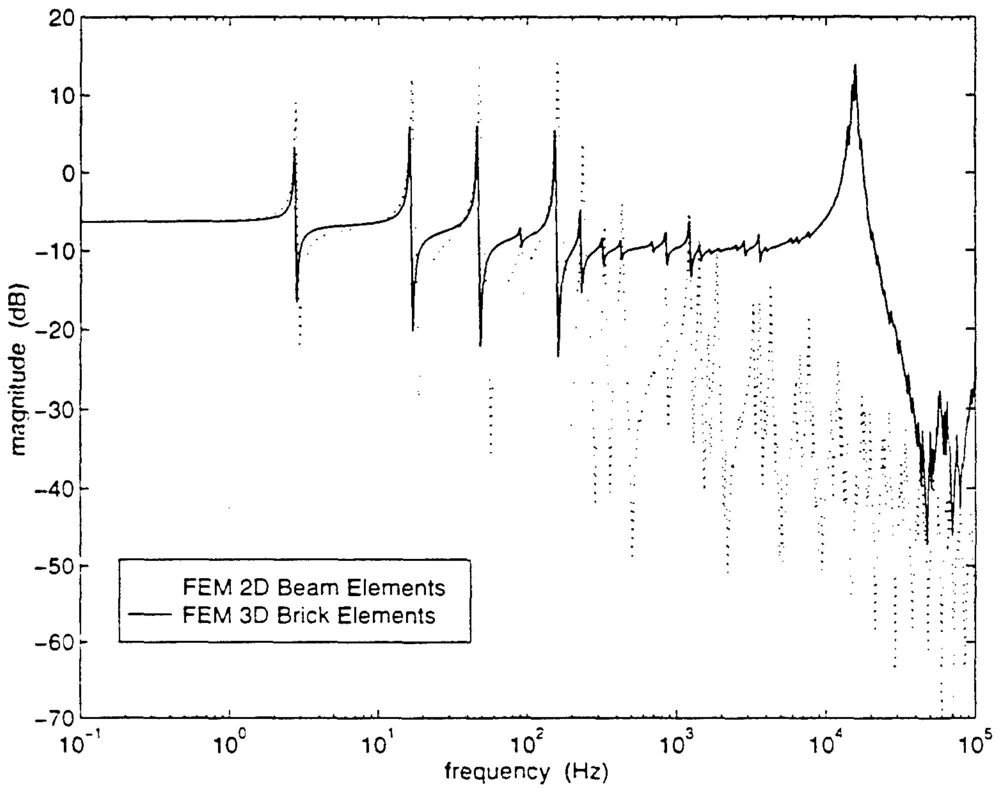

Figure 4.9: Rectangular Actuator to Sensor Transfer Functions for 2D FE Model with Finite Actuator Thickness and for 3D FE Model

To obtain the transfer function, a state space representation of the model is created. The modal frequencies are placed into the A matrix, the voltage output of the actuators is placed into the B and C matrices, 1% modal damping is added, and the transfer function is calculated. Figure 4.9 plots the transfer function of the finite element model using two-dimensional beam elements and an actuator thickness of 7.5 mils, as shown in Figure 4.5, and the transfer function of the finite element model using three-dimensional brick elements. The output of the 3D model, whose units are V/V, is normalized to the output of the 2D model. The frequencies of the low frequency poles and zeros match fairly well, although they are not exactly the same. This could be related to the fact that, in the three-dimensional model the width of

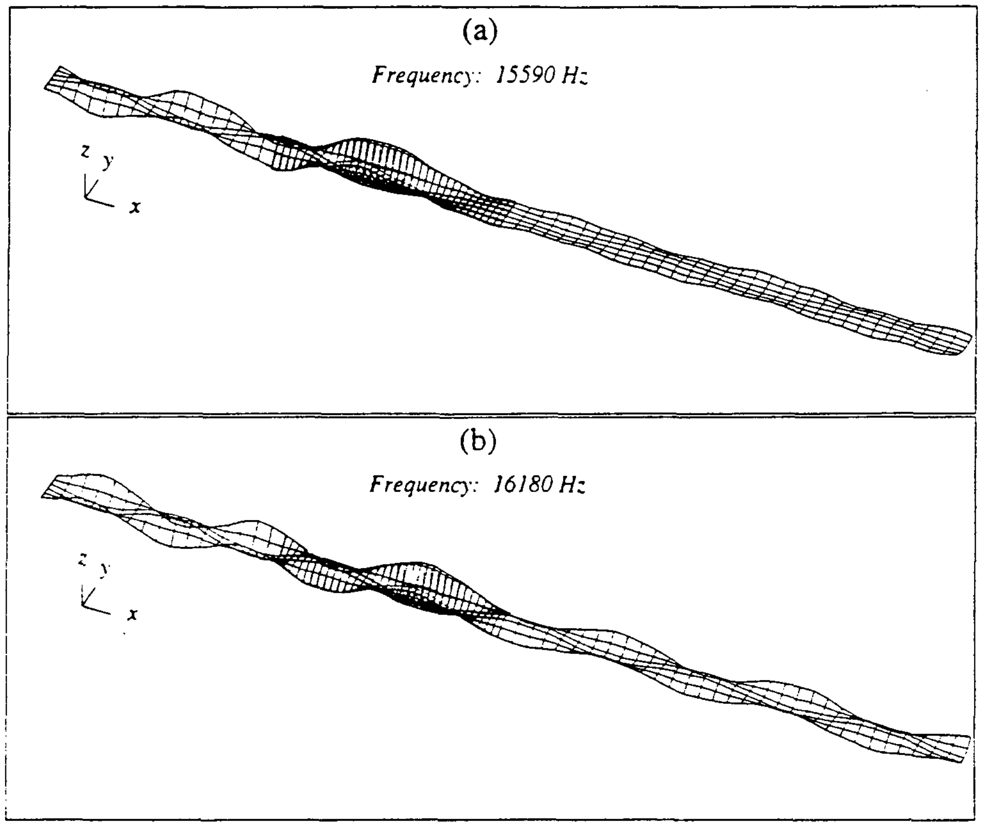

Figure 4.10: Three-Dimensional Modeshapes near 16000 Hz of Cantilever Beam with Rectangular Actuator-Sensor Pair

the actuator is not the same as the width of the beam, whereas the two-dimensional beam assumed a uniform cross-section in the portion of the beam covered by the actuator.

From this plot, it is obvious that including the width of the beam has a profound effect upon the transfer function. The rolloff of the transfer function for the three-dimensional beam occurs after 20,000 Hz, rather than after 200 Hz in that of the two-dimensional beam. There is also a high magnitude resonance in the transfer function for the three-dimensional beam near 16000 Hz. This resonance is caused by several modes exhibiting bending across the width of the beam. Figure 4.10 shows

a few of the mode shapes of the beam near 16000 Hz. It is this family of modes, which exhibits bending across the width of the beam and has high strain coupling to the actuator and sensor, which causes the high magnitude response in the transfer function. Therefore, if this experiment were performed in a laboratory, one would expect the magnitude of these modes to delay the rolloff of the transfer function by two decades.

4.2 Triangular Actuator-Sensor Pair

This section compares the analytical wave solution, two-dimensional finite element solutions and three-dimensional finite element solution for a cantilevered beam with a triangular actuator-sensor pair. Damping, finite actuator thickness, and finite beam and actuator width are included in the models to determine their effects upon the actuator to sensor transfer function. A transfer function from experimental data is then compared to these models.

4.2.1 Analytical Wave Model

The analytical transfer function for the cantilevered steel beam with a triangular actuator-sensor pair is determined using the solution algorithm of Section 2.2.4. The asymptotic dereverberated transfer function is found from Equations 2.40 and 2.41. A diagram of this cantilevered steel beam with the applied triangular actuator-sensor pair is in Figure 4.11. Figure 4.12 plots the analytical transfer function and its dereverberated asymptotes.

Since the finite thickness of the actuator and the finite width of the beam are not

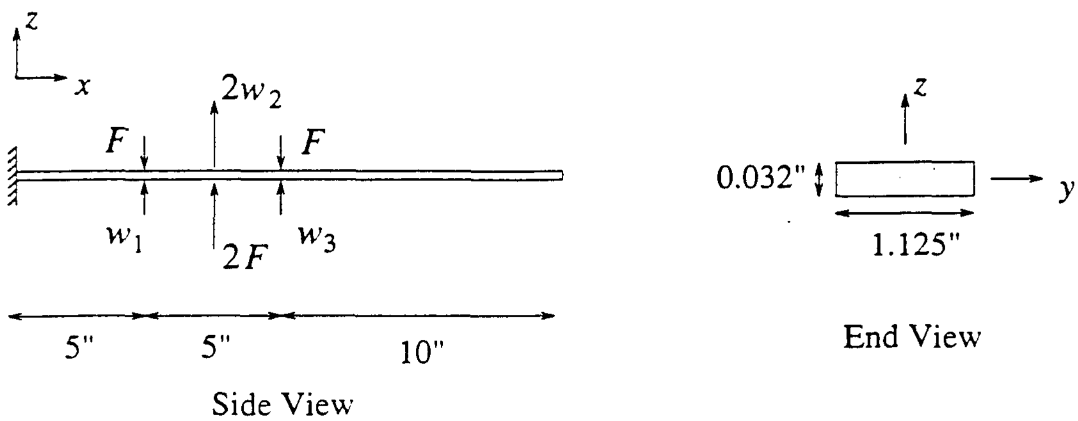

Figure 4.11: Cantilevered Steel Beam with Triangular Actuator-Sensor Pair of Zero Thickness

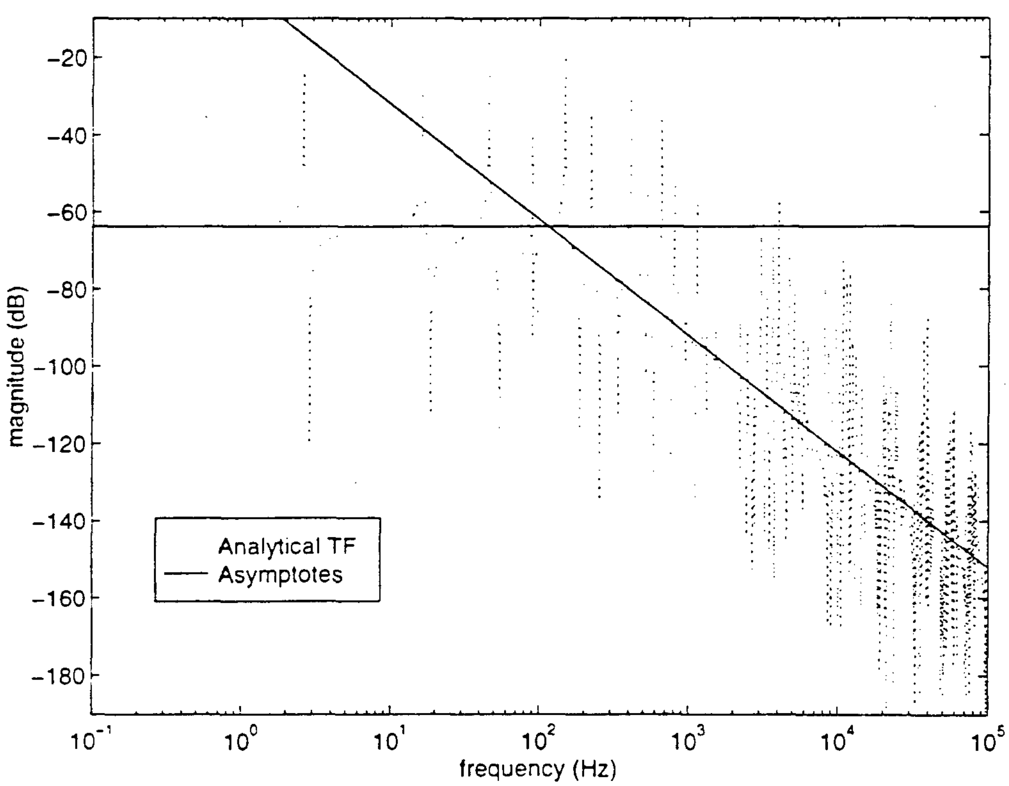

Figure 4.12: Analytical and Dereverberated Transfer Functions for Triangular Actuator-Sensor Pair on a Cantilevered Beam with Realistic Geometry

included in this model, this model will not match with any experimental data. As in the case of rectangular actuator-sensor pair, finite element models will be used to improve upon this model.

4.2.2 Two-Dimensional Finite Element Models

A finite element model of the beam in Figure 4.11 is generated using two-dimensional elastic beam elements. The modes of this beam are determined and placed into a state space model, and the transfer function is generated. Figure 4.13 shows the damped transfer function and the analytical transfer function. In the case of the triangular actuator-sensor pair, the units of the magnitude of the transfer function are m/N. However, Figure 4.13 plots the magnitude of the transfer function in decibels. As in the case of the rectangular actuator-sensor pair, these two transfer functions apparently plot exactly except for the magnitudes of the poles and zeros. Now, with the transfer function generated from the finite element model, a better estimate of the magnitude response for the individual modes and the final reverberant crossover frequency are known. Note that the crossover frequency of the dereverberated transfer function remains the same. Also, when this small amount of damping is added, above 1000 Hz, many pole-zero pairs nearly disappear due to high modal overlap.

As in the rectangular case, the dereverberated transfer function for the finite element model is determined by adding critical damping to the model, and solving for the transfer function. This transfer function is then compared to the asymptotes of the analytical dereverberated transfer function, Equations 2.40 and 2.41. Figure 4.14 shows these two dereverberated transfer functions, which match well, but not as well as the corresponding plot for the rectangular actuator-sensor pair.

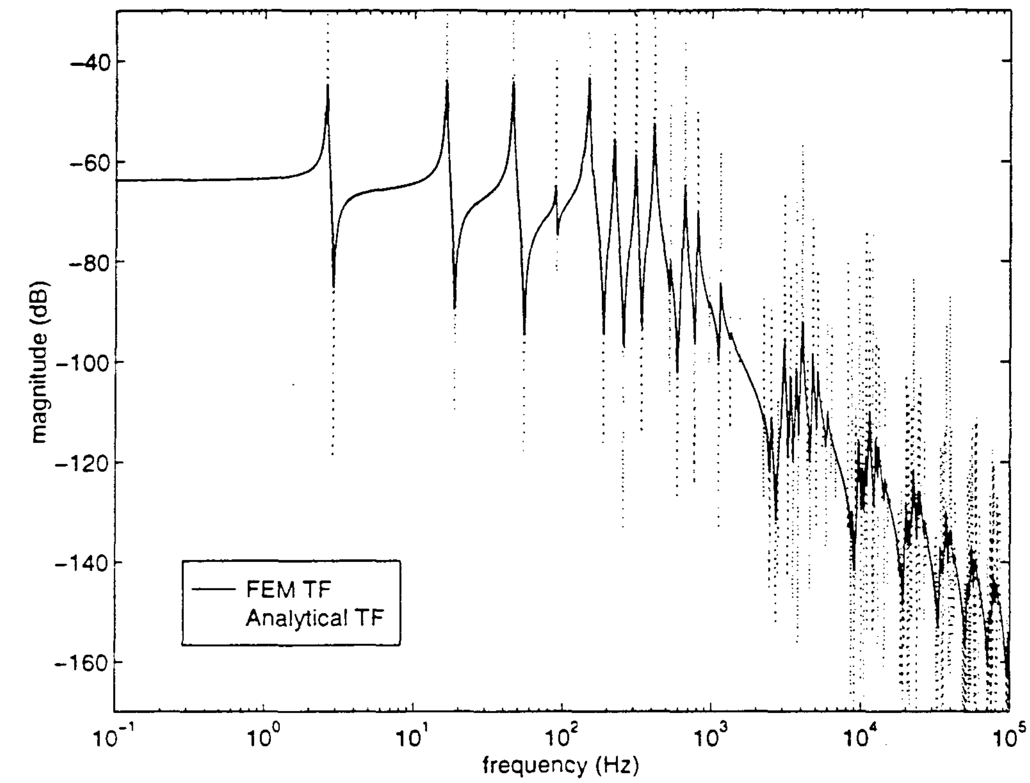

Figure 4.13: Transfer Functions for Triangular Actuator-Sensor Pair on Cantilevered Beam: Analytical with No Damping, and 2D FE Model with 1% Damping

The finite thickness of the actuator is next to be included in the model, as shown in Figure 4.15. In order to incorporate this triangular actuator thickness, two types of beam elements are included within the finite element model. The first element type has the properties of the steel beam, as in the previous finite element model. The second element is a two-node, two-dimensional, tapered, symmetric, elastic beam, which includes the thickness of the PZT-5A actuators on the top and the bottom of the beam. These two element types are given the proper dimensions and are used to create the finite element model. The transfer function is then found as in Section 4.1.

Figure 4.16 plots the triangular actuator to sensor transfer functions of the finite

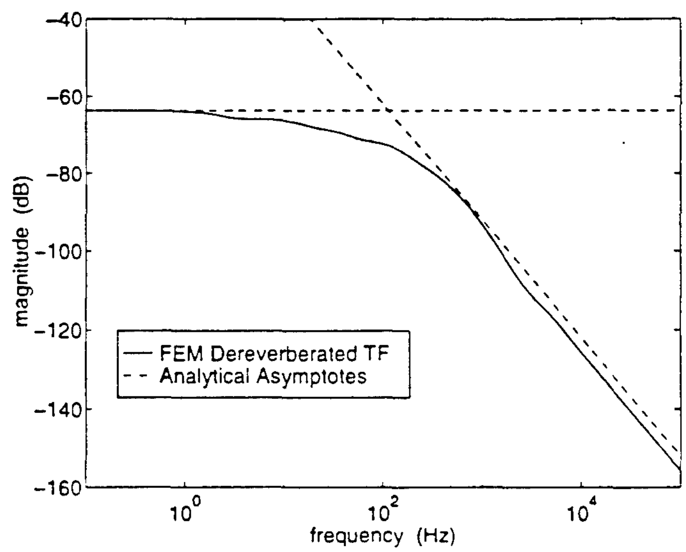

Figure 4.14: Dereverberated Triangular Actuator to Sensor Transfer Functions for 2D FE Model with 1% Damping and Analytical Model

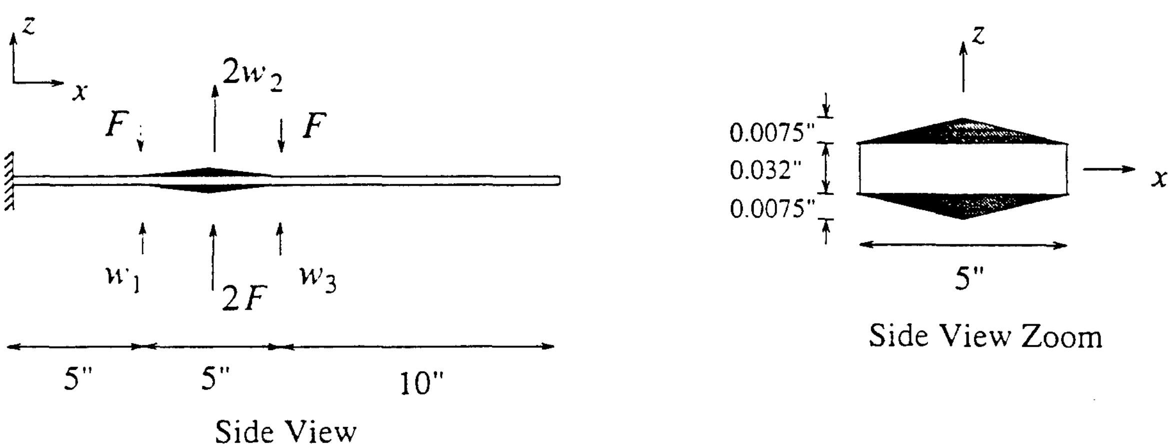

Figure 4.15: Cantilevered Steel Beam with Finite Thickness of Rectangular Actuator

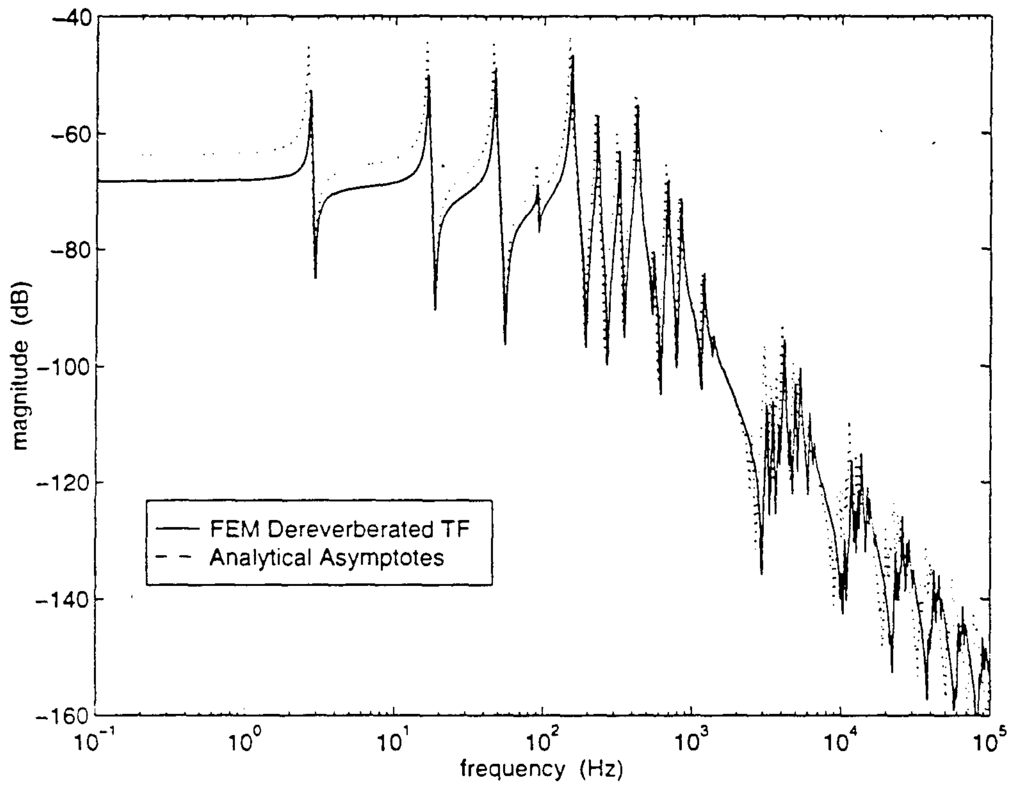

Figure 4.16: Transfer Functions for FE Model with Zero Triangular Actuator Thickness and with Triangular Actuator Thickness of 7.5 mil

element model without the actuator thickness, from Figure 4.11, and the finite element model with the actuator thickness, from Figure 4.15. Note how the increased mass and stiffness of the beam cause the frequencies of the poles to increase. This is same effect as in the rectangular actuator-sensor case. As the thickness of the actuator increases, the beam stiffness increases and the static gain decreases. Figure 4.17 plots the dereverberated asymptotes of the wave model and the dereverberated transfer function for the actuator being 0 mils, 7.5 mils, and 15 mils at its thickest point. As this plot shows, the transfer function is still rolling off at -30 dB/decade. However, as the thickness increases, the frequency at which it begins to rolloff increases slightly, but not as much as in the case of the rectangular actuator-sensor pair of Figure 4.7.

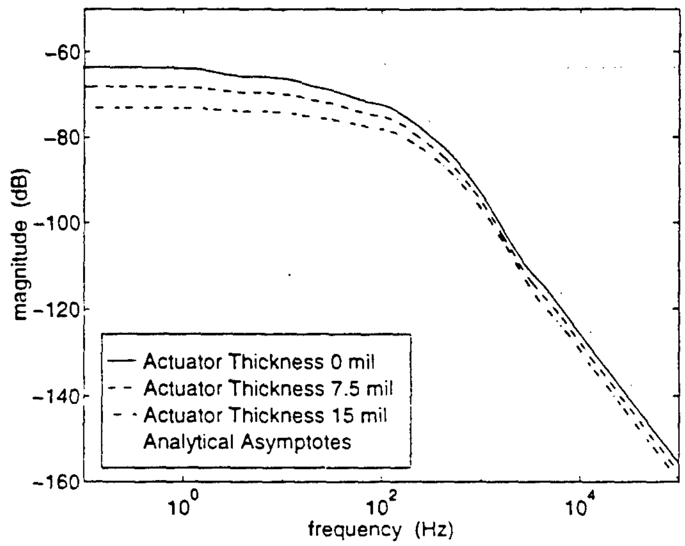

Figure 4.17: Analytical Asymptotes and Dereverberated Transfer Functions for Varying Actuator Thickness on a Cantilever Beam: 0 mil, 7.5 mil, 15 mil

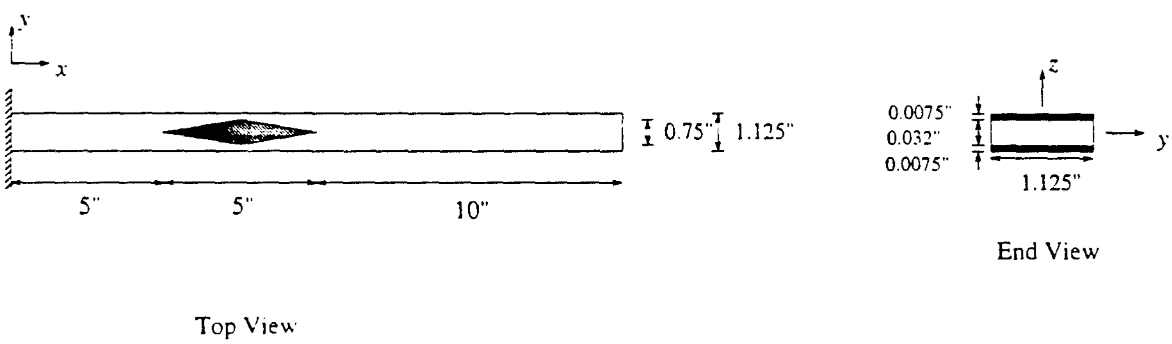

Figure 4.18: Top and End View of Three-Dimensional Steel Beam with Triangular Actuator-Sensor Pairs

4.2.3 Three-Dimensional Finite Element Models

In Section 4.1 it was shown that including the finite width of the beam in a finite model has a large effect upon transfer function. Now, a three-dimensional brick model of the cantilevered beam with triangular actuators and sensors is developed using the same element types as in the rectangular case.

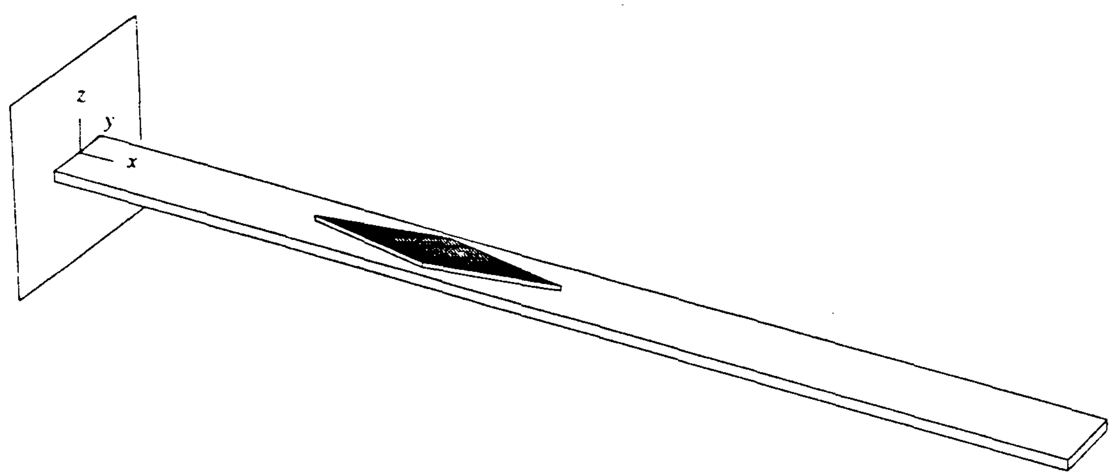

Figure 4.19: Three-Dimensional Perspective of Steel Beam with Triangular Actuator-Sensor Pairs

Figure 4.18 is a schematic of the top and end views of the three-dimensional beam with triangular actuator-sensor pairs. In the three-dimensional case, the triangular shape is obtained by shaping the width of the actuator; the thickness is a constant 7.5 mils. The symmetry of the beam is maintained by including two triangles which are symmetric about the center of the beam in the shape of the actuator. Also, there is an actuator-sensor pair on the top and the bottom of the beam. Figure 4.19 gives a three-dimensional perspective of the entire beam, where the thickness of the beam and the actuator are exaggerated.

To obtain the actuator to sensor transfer function for this beam, the natural modes of the beam are calculated by the finite element software. Then a state space representation of the model is developed as in the rectangular case, and the transfer function is calculated.

Figure 4.20 compares the transfer function of the two-dimensional finite element model with a finite actuator thickness in Figure 4.16 and the transfer function of the

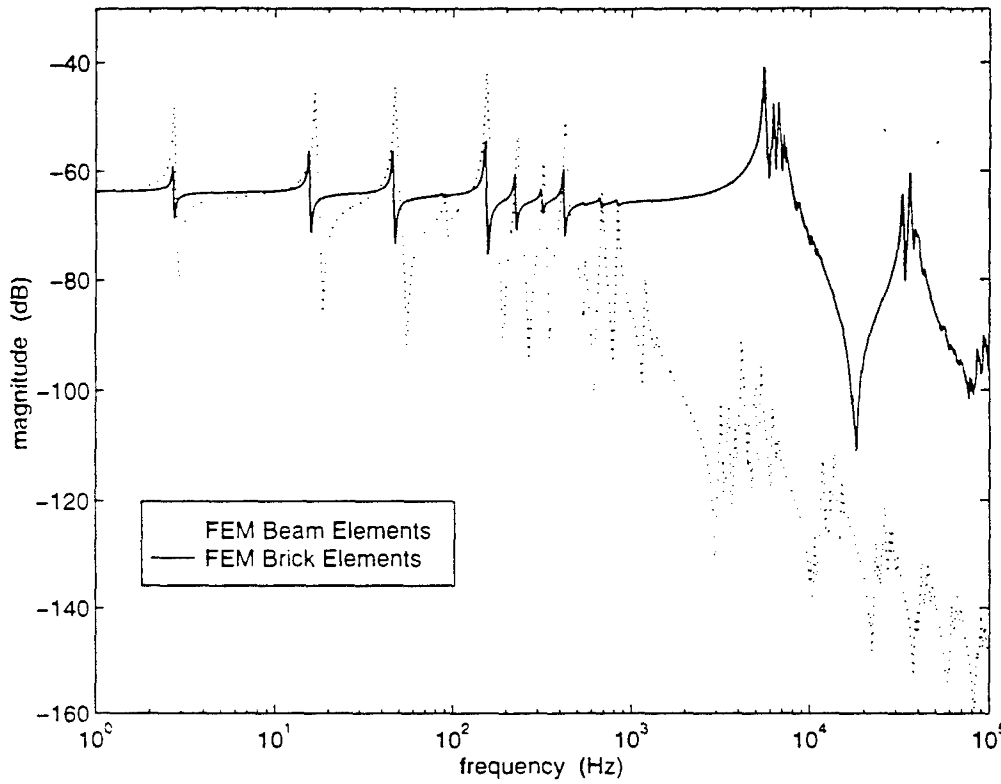

Figure 4.20: Triangular Actuator to Sensor Transfer Functions for 2D FE Model with Finite Actuator Thickness and for 3D FE Model

three-dimensional finite element model. The output of the 3D model, whose units are V/V, is normalized to the output of the 2D model. The transfer function of the three-dimensional beam shows the impact of the transverse bending modes, similar to Figure 4.9. However, the frequency range at which the transverse bending modes take effect is lower for the triangular case. Also, a second resonance in the transfer function delays some of the rolloff after the first group. These resonances are caused by families of first and third transverse bending modes in the beam. Figure 4.21 shows a few of these mode shapes.

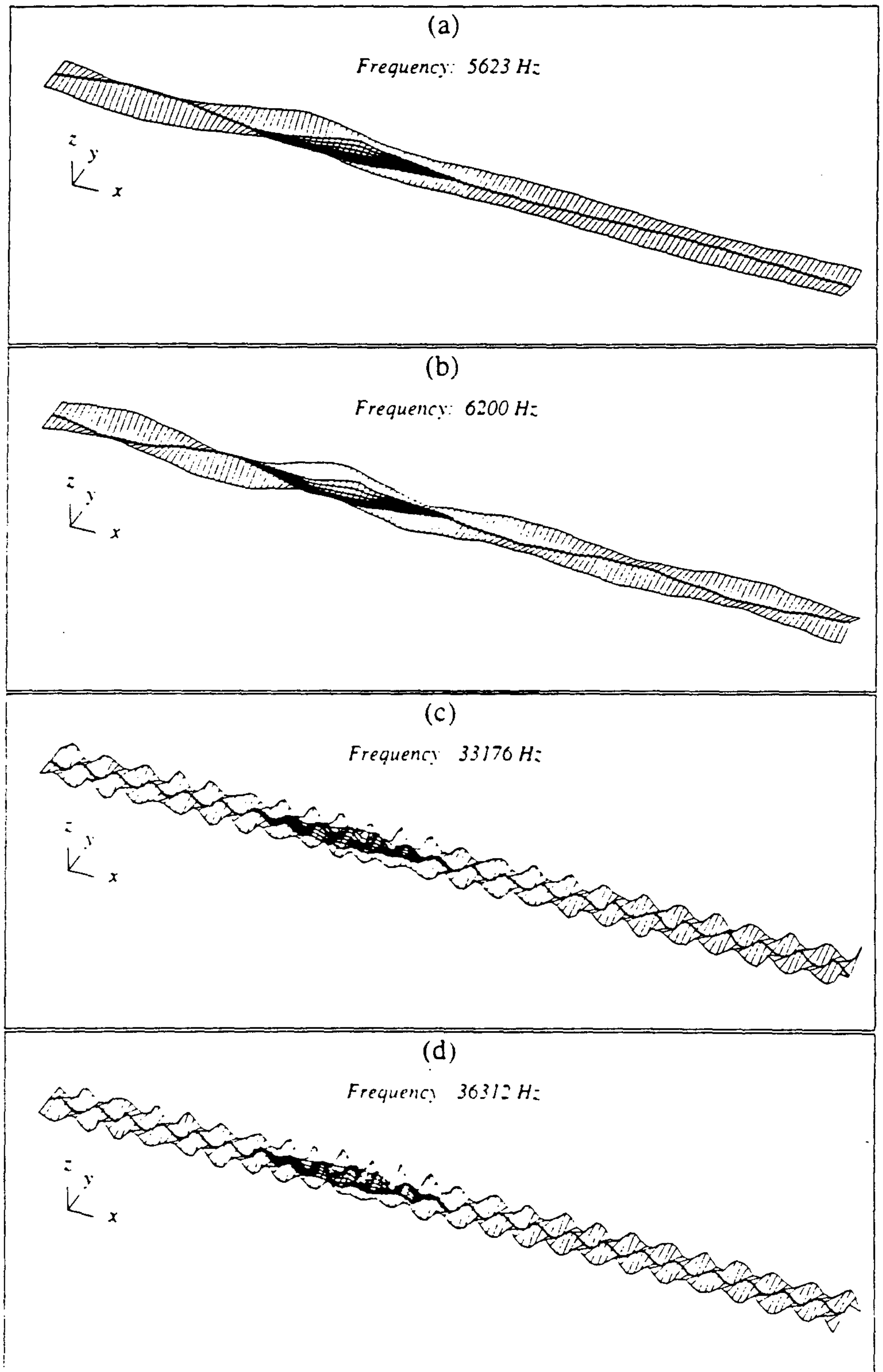

Figure 4.21: Modeshapes of Cantilever Beam with Triangular Actuator-Sensor Pair Showing First and Third Mode Transverse Bending

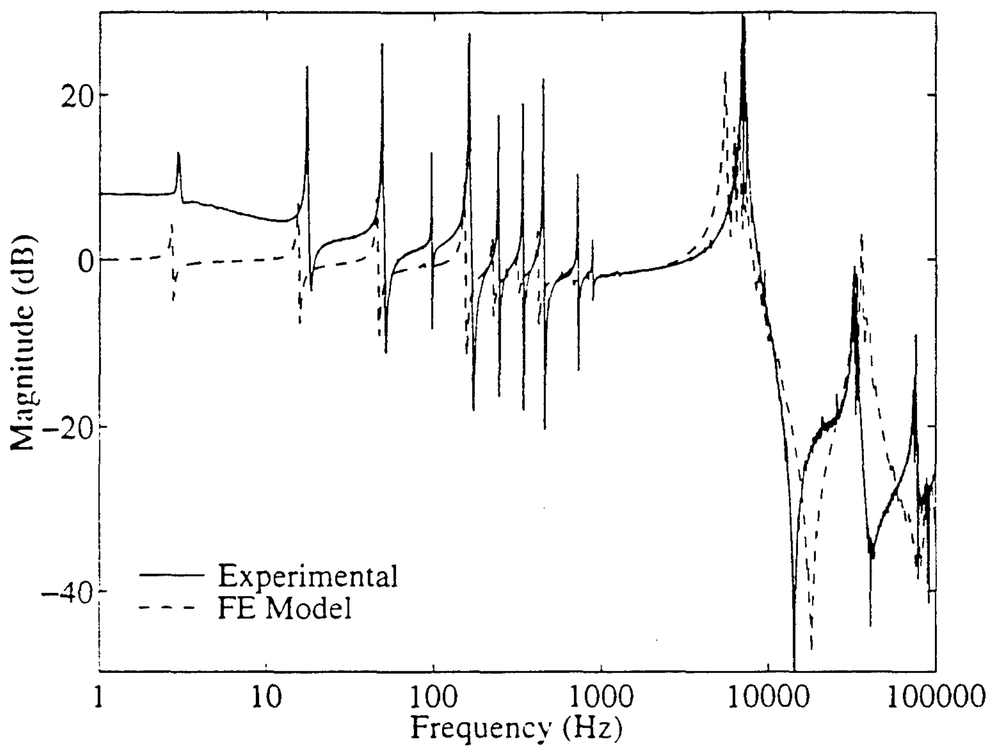

Figure 4.22: Experimental Transfer Function and FE Model Transfer Function

4.2.4 Experimental Results

In order to confirm this analysis an experiment was conducted in the laboratory using a beam matching the dimensions and properties of that pictured in Figure 4.18. The actuator to sensor transfer function was recorded, and in Figure 4.22 the experimental data is compared to the transfer function generated from the three-dimensional finite element model. The static gains of both transfer functions have been normalized such that the two transfer functions match at 1000 Hz.

Overall, the experimental data correlates very well with the finite element model. At low frequency, there is a small gain error due to laboratory inconsistencies, such as thermal effects, to which the PVDF sensor is particularly sensitive. Additionally, the coherence of the data at low frequency is poor due to noise in the system. At very

high frequencies, the correlation between transfer functions is low due to increasing inaccuracies when nearing the limit of the finite element model. Regardless of these small errors, the message is clear: the finite width of the beam, the actuator, and the sensor lead to a large response in the transfer function above the frequency of the rolloff predicted by the two-dimensional transfer function. This large response is due to higher frequency transverse bending modes.

4.3 Discussion

This chapter discussed various models generated to improve upon the original Bernoulli-Euler analytical models generated in Chapter 2. While adding damping and finite actuator thickness to the model improved its accuracy, the most accurate model was obtained when the finite width of the beam and the actuator-sensor pair were included. In this case, the rolloff due to the lengthwise bending modes still occurs, however, the magnitude of the response to the transverse bending modes is strong enough to delay that rolloff.

A current field of research is the use of interdigitated electrodes on piezoceramic actuators and sensors, which would allow for uniaxial actuation and sensing. This means that an actuator would excite only the longitudinal bending strain, and the sensor would only measure the longitudinal bending strain. If such an actuator-sensor pair were used on this beam, the response to the transverse bending strain could be lessened, and the rolloff due to the longitudinal bending stain would reappear.

To investigate this possibility of decreasing the response to the transverse bending modes, a new finite element model is created. This model has the same dimensions and properties as in Figure 4.18, except for one: the electromechanical constant which

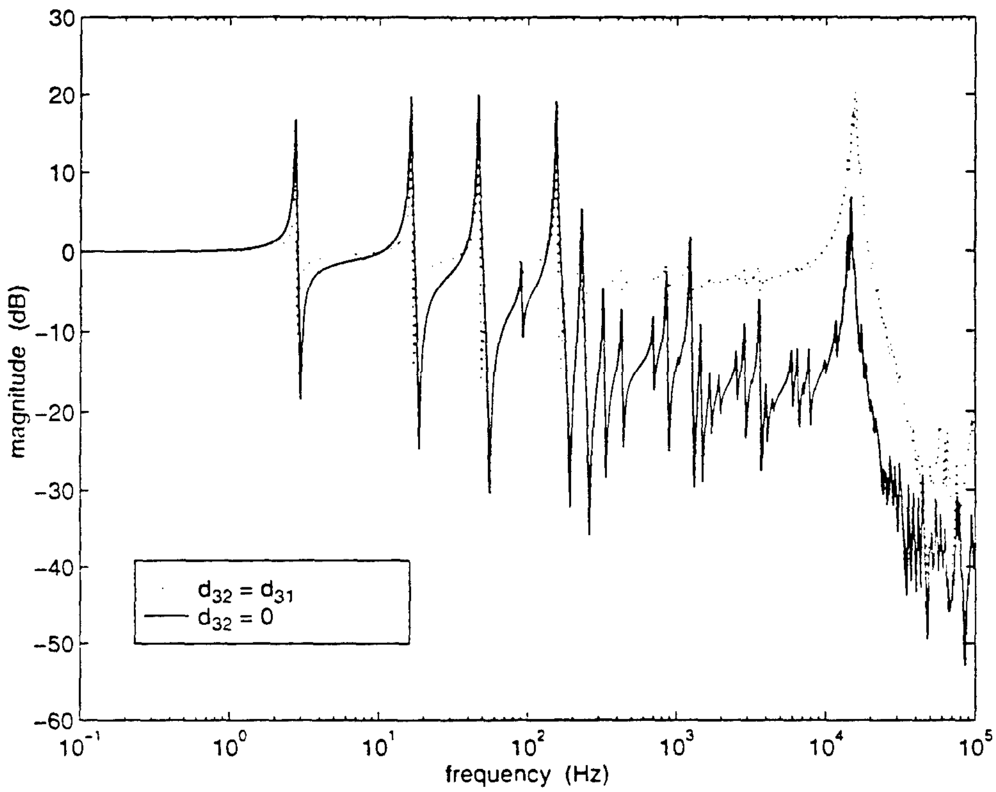

Figure 4.23: Transfer Function for FE Model of Rectangular Actuator-Sensor Pair with d_{32} is Active and Inactive

couples the modal strain of the transverse bending modes and the voltage, d_{32}, is set to zero. A new state space model is determined, and the transfer function is calculated.

Figure 4.23 compares the rectangular actuator to sensor transfer functions where d_{32} is active and inactive, i.e. when the actuator and sensor are piezoelectrically isotropic, $d_{32} = d_{31}$, and piezoelectrically anisotropic, $d_{32} = 0$. These two transfer functions are normalized such that the static response is 0 dB. The transfer function is exhibiting some of the rolloff due to the longitudinal bending modes. The response to the transverse waves is not zero when $d_{32} = 0$, however, the magnitude of the response has dropped significantly as compared to the magnitude of the transfer function when $d_{32} = d_{31}$. This magnitude reduction is approximately 20 dB, which is about a factor

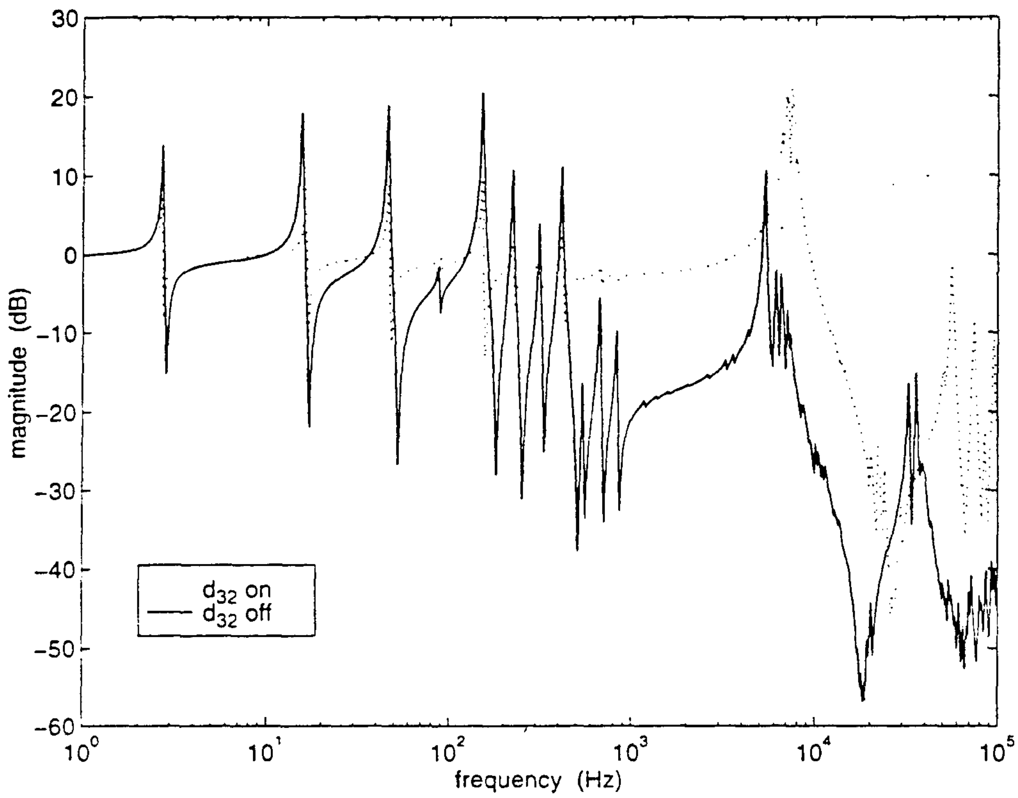

Figure 4.24: Transfer Function for FE Model of Triangular Actuator-Sensor Pair with d_{32} is Active and Inactive

of 10. Poisson's ratio for steel is $\nu = 0.33$, and $\nu^2 = 0.1089$, which is one-tenth of the previous coupling. It is evident that the magnitude reduction is related to the Poisson ratio of the beam, since the transverse strain associated with transverse bending is still sensed and actuated by the $d31$ piezoelectric effects.

Figure 4.24 compares the transfer functions for the triangular pair where the actuator and sensor are sensitive to transverse bending waves and are not sensitive to these waves. The effect of setting $d_{32} = 0$ in the triangular case is similar to that of the rectangular case. Therefore, in both the rectangular and triangular cases it is possible to retain some of the rolloff of the transfer function for the Bernoulli-Euler beam by further tailoring the actuator-sensor pair to the task.

Chapter 5

Conclusions

5.1 Analytical Models for Collocated Actuator-Sensor Pairs

It was shown in Chapter 2 that wave models can be used to determine analytical expressions for the magnitude of actuator to sensor transfer functions for Bernoulli-Euler beams. The analytical dereverberated transfer function is composed of low and high frequency asymptotes, which are determined by taking the limits of the analytical transfer function as $k \to 0$ and $k \to \infty$.

The high frequency transfer function for a point actuator-sensor pair always rolls off as a function of k^{-3}. The exact solution for the low frequency asymptote depends upon the location of the actuator-sensor pair on the beam and the beam end conditions. The exact solution for the high frequency asymptote is only dependent upon the beam end conditions.

The high frequency transfer function for a rectangular actuator-sensor pair always rolls off as a function of k^{-1}, while the transfer function for a triangular pair always rolls off as a function of k^{-3}. The exact solutions for the dereverberated transfer

functions of the rectangular and triangular pairs are not dependent upon actuator-sensor location or the beam end conditions.

At first glance, the analytical transfer function for actuator-sensor pairs whose shapes are more complex than a triangular, e.g. quadratic and cubic, appear to rolloff with slopes steeper than k^{-4}. However, further investigation revealed implicit factors of k in the numerator of the analytical transfer function, which causes it to roll off as a function of k^{-4}, whenever the shape is more complex than triangular. Due to manufacturing difficulties and diminishing returns in rolloff, shapes more complex than triangular are deemed impractical, and no further investigation was conducted.

In addition to the wave solution, a modal residue solution were used to determine the dereverberated transfer functions for several actuator-sensor pairs on a pinned-pinned beam. These solutions produced results which more closely matched the analytical asymptotes as the actuator and sensor shapes increased in complexity. However, when end conditions other than pinned-pinned are used, the assumed mode shape becomes complicated, and the solution becomes difficult to generate due to numerical instabilities.

5.2 Analytical Models for Noncollocated Actuator-Sensor Pairs

In Chapter 3, wave modelling was used to determine the transfer functions for noncollocated point, rectangular, and triangular actuator-sensor pairs on pinned-pinned beams. Only noncollocation due to a difference in length were considered for the shaped actuator-sensor pairs.

The transfer function for the noncollocated point actuator-sensor pair will rolloff as a function of k^{-3}, regardless of the distance between the actuator and sensor. Only in analytically perfect collocated conditions will the transfer function follow the collocated high frequency asymptote. Even with a slight noncollocation, the transfer function will eventually follow the *lower* noncollocated asymptote. The asymptote is lower because the rolloff effect of the evanescent waves is stronger than the rollup effect of the missing zeros in the transfer function.

The transfer function becomes noncollocated at the wavenumber where the deformation of the beam at the position of the actuator is the opposite sign of that of the position of the sensor. A general rule of thumb for wavenumber of noncollocation is

$$k_{\mathrm{non}} = \frac{\pi}{2|x_s|} \tag{5.1}$$

where k_{non} is the wavenumber of noncollocation and x_s is the distance between the actuator and sensor.

It is known that for a collocated point actuator-sensor pair, the zeros of the transfer function are the same as the poles of the transfer function for the same beam with a pinned boundary at the position of the actuator-sensor pair. Analysis showed that, in the case of a noncollocated point actuator-sensor pair, the zeros of the transfer function cannot be replicated by the poles due to any simple boundary condition.

In the case of the noncollocated rectangular actuator-sensor pair, the transfer function will always rolloff as a function of k^{-1}, regardless of the difference in actuator and sensor lengths. However, in the rectangular case, the noncollocated asymptote is actually *higher* than the collocated asymptote. The asymptote is higher because the missing zeros have a greater effect on the magnitude than the evanescent waves.

The rule of thumb in Equation 5.1 can be used as a rough estimate for the wavenumber of noncollocation, where $x_s = l_s - l_a$. As the difference in length of actuator and length of sensor increases, the wavenumber of the first missing zero decreases. This implies that there is little room for manufacturing error if a collocated transfer function is desired using a rectangular actuator-sensor pair.

The actuator to sensor transfer function for the triangular pair will always rolloff as a function of k^{-3}, regardless of the difference in length between the actuator and sensor. The noncollocated transfer function follows an asymptote which is *lower* than the collocated asymptote. This is a result of two factors: there are no missing zeros in the noncollocated transfer function to increase the magnitude, and the evanescent waves cause a magnitude decrease in the transfer function.

These properties make it possible to improve the rolloff characteristics of the transfer function. By following the rule

$$\frac{l_s}{l_a} = 1.43 \tag{5.2}$$

where l_s is the length of the sensor and l_a is the length of the actuator, the region of near pole-zero cancellations in the transfer function can be maximized. Thus, a small amount of additional rolloff can be gained, and reverberant modal responses in this range of wavenumber are minimized.

5.3 2D and 3D Solutions for Collocated Shaped Actuator-Sensor Pairs

Chapter 4 showed that finite element models could be used to add realistic effects to the beam model that were not included in the wave models. Such effects include damping, finite actuator thickness, and finite beam width. The general results of adding these effects is the same for both the rectangular and triangular actuator-sensor pair.

The transfer function created from the two dimensional finite element models match the wave solution extremely well. Once this correlation is established, the finite element model can be used to add damping and finite actuator thickness to the system. As the thickness of the actuator increases, the transfer function decreases in magnitude due to the increased stiffness. Also, the frequency at which the dereverberated transfer function rolls off increases as the actuator thickness increases. However, the slope of the high frequency rolloff remains the same regardless of actuator thickness.

The transfer functions generated from the three dimensional finite element models show the problems associated with high frequency transverse bending modes. Since the actuators impose transverse strain, the sensor observes transverse strain, and there is a Poisson coupling between longitudinal bending modes and transverse bending modes, a large response occurs in the transfer function due to the transverse modes. This large response causes the response due to the transverse modes to mask the rolloff associated with the longitudinal bending modes.

If the actuator and sensor are designed such that the actuator imposes no transverse strain and the sensor observes no transverse strain ($d_{32} = 0$ for both the actuator

and sensor), only the Poisson coupling remains. This will reduce the transfer function response to the transverse bending modes by about 20 dB, and some of the rolloff associated with the Bernoulli-Euler bending can be recovered.

References

[1] Andersson, M. S. and Crawley, E. F., "Discrete Shaped Strain Sensors for Intelligent Structures," *Proceedings, 33rd AIAA/ASME/ASCE/AHS Structures, Structural Dynamics, and Materials Conference*, Dallas, TX, April 13–15 1992, pp. 566–576. AIAA paper No. 92-2046.

[2] Andersson, M. S., *Spatially Filtering Strain Sensors for Structural Shape Estimation of Intelligent Structures*, Master's thesis, Massachusetts Institute of Technology, Feb. 1993. Space Engineering Research Center Report #3-93.

[3] Aubrun, J. N., "Theory of the Control of Structures by Low-Authority Controllers," *AIAA Journal of Guidance and Control*, Vol. 3, No. 5, 1980, pp. 444–451.

[4] Blevins, R. D., *Formulas for Natural Frequency and Mode Shape*, Van Nostrand Reinhold, New York, NY, 1979.

[5] Burke, S. E., Hubbard, J. E. Jr., and Meyer, J. E., "Colocation: Design Constraints for Distributed and Discrete Transducers," *Proceedings, 13th Biennial Conference on Mechanical Vibration and Noise*, Miami, Florida, September 22-25 1991, pp. 75–81. DE Vol. 34.

[6] Chattopadhyay, A. and Seeley, C. E., "A Multiobjective Design Optimization Procedure for Control of Structures Using Piezoelectric Materials," *Journal of Intelligent Material Systems and Structures*, Vol. 5, No. 5, 1994, pp. 403–411.

[7] Clark, R. L. and Fuller, C. R., "Modal Sensing of Efficient Acoustic Radiators with Polyvinylidene Fluoride Distribued Sensors in Active Structural Acoustic

Control Approaches," *The Journal of the Acoustical Society of America*, Vol. 91, No. 6, 1992, pp. 3321–3329.

[8] Crawley, E. F. and Anderson, E. H., "Detailed Models of Piezoceramic Actuation of Beams," *Journal of Intelligent Material Systems and Structures*, Vol. 1, No. 1, Jan. 1990, pp. 4–25.

[9] Crawley, E. F. and de Luis, J., "Use of Piezoelectric Actuators as Elements of Intelligent Structures," *AIAA Journal*, No. 10, Oct. 1987, pp. 1373–1385. AIAA Paper 86-0878.

[10] de Luis, J. and Crawley, E. F., *The Use of Piezo-Ceramics as Distributed Actuators in Flexible Space Structures*, Master's thesis, Massachusetts Institute of Technology, Aug. 1985. Space Systems Laboratory Report #20-85.

[11] Hagood, N. W., Chung, W. H., and von Flotow, A., "Modelling of Piezoelectric Actuator Dynamics for Active Structural Control," *Journal of Intelligent Material Systems and Structures*, July 1990, pp. 327–354.

[12] Hall, S. R., Crawley, E. F., How, J., and Ward, B., "A Hierarchic Control Architecture for Intelligent Structures," *AIAA Journal of Guidance, Control, and Dynamics*, Vol. 14, No. 3, May–June 1991.

[13] Lester, H. C. and Lefebvre, S., "Piezoelectric Actuator Models for Active Sound and Vibration Control of Cylinders," *Journal of Intelligent Material Systems and Structures*, Vol. 4, No. 3, 1993, pp. 295–306.

[14] Lu, L. Y., Utku, S., and K., W. B., "On the Placement of Active Members in Adaptive Truss Structures for Vibration Control," *Smart Materials and Structures*, Vol. 1, No. 1, 1992, pp. 8–23.

[15] Lu, L. Y., Utku, S., and K., W. B., "Vibration Suppression for Large Scale Adaptive Truss Structures Using Direct Output Feedback Control," *Journal of Intelligent Material Systems and Structures*, Vol. 4, No. 3, 1993, pp. 385–397.

[16] MacMartin, D. G. and Hall, S. R., *A Stochastic Approach to Broadband Control of Parametrically Uncertain Structures*, Ph.D. thesis, Massachusetts Institute of Technology, May 1992. Department of Aeronautics and Astronautics, Space Engineering Research Center Report #5-92.

[17] Meirovitch, L., *Analytical Methods in Vibrations*, Macmillan, New York, NY, 1967.

[18] Miller, D. W. and von Flotow, A., "A Travelling Wave Approach to Power Flow in Structural Networks," *Journal of Sound and Vibration*, Vol. 128, No. 1, 1989, pp. 145–162.

[19] Sullivan, J. M., Hubbard, Jr., J. E., and Burke, S. E., "Modeling Approach for Two-Dimensional Distributed Transducers of Arbitrary Spatial Distribution," *Proceedings, Proceedings of the SPIE Conference on Smart Structures and Intelligent Systems*, Albuquerque, NM, Feb. 1993.

[20] Zhou, S., Liang, C., and Rogers, C. A., "Integration and Design of Piezoelectric Patch Actuators," *Journal of Intelligent Material Systems and Structures*, Vol. 6, No. 1, 1995, pp. 125–133.

Appendix A

Transfer Functions for Collocated Actuator-Sensor Pairs

This Appendix is a listing of some representative transfer functions that were derived for the completion of this work. For all of the following transfer functions listed, the actuator is centered on the beam.

A.1 Transfer Functions for Point Actuator-Sensor Pairs

Collocated point actuator-sensor pair on a pinned-pinned beam, which is the same as Equation 2.29:

$$\frac{y_p}{u_p} = -\frac{e^{\frac{1}{2}kl}\left(\sin(\frac{kl}{2}) - \cos(\frac{kl}{2})\right) + e^{-\frac{1}{2}kl}\left(\sin(\frac{kl}{2}) + \cos(\frac{kl}{2})\right)}{4EIk^3\cos(\frac{kl}{2})\left(e^{\frac{1}{2}kl} + e^{-\frac{1}{2}kl}\right)} \tag{A.1}$$

Collocated point actuator-sensor pair on a free-free beam:

$$\frac{y_p}{u_p} = \frac{\cos(\frac{kl}{2})\left(e^{\frac{1}{2}kl} + e^{-\frac{1}{2}kl}\right) + 2}{2EIk^3\left[e^{\frac{1}{2}kl}\left(\sin(\frac{kl}{2}) + \cos(\frac{kl}{2})\right) + e^{-\frac{1}{2}kl}\left(\sin(\frac{kl}{2}) - \cos(\frac{kl}{2})\right)\right]} \tag{A.2}$$

Collocated point actuator-sensor pair on a cantilevered beam:

$$\frac{y_p}{u_p} = \frac{\cos(\frac{kl}{2})\left[\cos(\frac{kl}{2})\left(e^{kl} - e^{-kl}\right) - \sin(\frac{kl}{2})\left(e^{kl} + e^{-kl} + 2\right)\right]}{2EIk^3\left[\left(2\cos^2(\frac{kl}{2}) - 1\right)\left(e^{kl} + e^{-kl}\right) + 2\right]} \tag{A.3}$$

Noncollocated point actuator-sensor pair on a pinned-pinned beam for negative x_s:

$$\frac{y_p}{u_p} = \frac{\left(e^{\frac{1}{2}kl} + e^{-\frac{1}{2}kl}\right)\left[\cos(kx_s)\sin(\frac{kl}{2}) - \sin(kx_s)\cos(\frac{kl}{2})\right] + \cos(\frac{kl}{2})\left(e^{\frac{1}{2}kl}e^{kx_s} - e^{-\frac{1}{2}kl}e^{-kx_s}\right)}{4EIk^3\cos(\frac{kl}{2})\left(e^{\frac{1}{2}kl} + e^{-\frac{1}{2}kl}\right)} \tag{A.4}$$

for positive x_s:

$$\frac{y_p}{u_p} = \frac{\left(e^{\frac{1}{2}kl} + e^{-\frac{1}{2}kl}\right)\left[\cos(kx_s)\sin(\frac{kl}{2}) + \sin(kx_s)\cos(\frac{kl}{2})\right] + \cos(\frac{kl}{2})\left(e^{\frac{1}{2}kl}e^{-kx_s} - e^{-\frac{1}{2}kl}e^{kx_s}\right)}{4EIk^3\cos(\frac{kl}{2})\left(e^{\frac{1}{2}kl} + e^{-\frac{1}{2}kl}\right)} \tag{A.5}$$

Noncollocated point actuator-sensor pair on a cantilevered beam for negative x_s:

$$\begin{aligned} C_1 = \Big[& 2\sin(kx_s)\left[\sin(\tfrac{kl}{2})\left(e^{-\frac{1}{2}kl} - e^{\frac{1}{2}kl}\right) - \cos(\tfrac{kl}{2})\left(e^{-\frac{1}{2}kl} + e^{\frac{1}{2}kl}\right) + \left(\tfrac{1}{2} - \cos^2(\tfrac{kl}{2})\right)\left(e^{kl} + e^{-kl}\right) - 1\right] \\ & + \cos(kx_s)\left[2\sin(\tfrac{kl}{2})\cos(\tfrac{kl}{2})\left(-e^{kl} - e^{-kl}\right) + e^{kl} - e^{-kl}\right] \\ & + e^{-kx_s}\left[\sin(\tfrac{kl}{2})\left(e^{\frac{1}{2}kl} - e^{-\frac{1}{2}kl} - 2\cos(\tfrac{kl}{2})\right) - \cos(\tfrac{kl}{2})\left(e^{-\frac{1}{2}kl} + e^{\frac{1}{2}kl} + 2e^{-kl}\cos(\tfrac{kl}{2})\right) + e^{-kl} - 1\right] \\ & + e^{kx_s}\left[\sin(\tfrac{kl}{2})\left(e^{-\frac{1}{2}kl} - e^{\frac{1}{2}kl} - 2\cos(\tfrac{kl}{2})\right) + \cos(\tfrac{kl}{2})\left(e^{-\frac{1}{2}kl} + e^{\frac{1}{2}kl} + 2e^{kl}\cos(\tfrac{kl}{2})\right) - e^{kl} + 1\right]\Big] \end{aligned}$$

$$\frac{y_p}{u_p} = \frac{C_1}{4EIk^3\left[\left(2\cos^2(\frac{kl}{2}) - 1\right)\left(e^{kl} + e^{-kl}\right) + 2\right]} \tag{A.6}$$

for positive x_s:

$$
\begin{aligned}
C_2 = \Bigg[& 2\sin(kx_s)\Big[\sin(\tfrac{kl}{2})\big(e^{-\frac{1}{2}kl}-e^{\frac{1}{2}kl}\big)-\cos(\tfrac{kl}{2})\big(e^{-\frac{1}{2}kl}+e^{\frac{1}{2}kl}\big)+\big(\cos^2(\tfrac{kl}{2})-\tfrac{1}{2}\big)\big(e^{kl}+e^{-kl}\big)+1\Big] \\
& +\cos(kx_s)\Big[2\sin(\tfrac{kl}{2})\cos(\tfrac{kl}{2})\big(-e^{kl}-e^{-kl}\big)+e^{kl}-e^{-kl}\Big] \\
& +e^{-kx_s}\Big[\sin(\tfrac{kl}{2})\big(e^{\frac{1}{2}kl}-e^{-\frac{1}{2}kl}-2\cos(\tfrac{kl}{2})\big)-\cos(\tfrac{kl}{2})\big(e^{-\frac{1}{2}kl}+e^{\frac{1}{2}kl}-2e^{kl}\cos(\tfrac{kl}{2})\big)-e^{kl}+1\Big] \\
& +e^{kx_s}\Big[\sin(\tfrac{kl}{2})\big(e^{-\frac{1}{2}kl}-e^{\frac{1}{2}kl}-2\cos(\tfrac{kl}{2})\big)-\cos(\tfrac{kl}{2})\big(e^{-\frac{1}{2}kl}-e^{\frac{1}{2}kl}+2e^{-kl}\cos(\tfrac{kl}{2})\big)+e^{-kl}-1\Big]\Bigg]
\end{aligned}
$$

$$
\frac{y_p}{u_p} = \frac{C_2}{4EIk^3\left[\left(2\cos^2(\frac{kl}{2})-1\right)\left(e^{kl}+e^{-kl}\right)+2\right]} \tag{A.7}
$$

A.2 Transfer Functions for Rectangular Actuator-Sensor Pairs

Collocated rectangular actuator-sensor pair on a pinned-pinned beam:

$$
\begin{aligned}
C_3 = \Bigg[& \cos(\tfrac{kl}{2})\Big[e^{\frac{1}{2}kl}\left(e^{-kl_a}-2\cos(\tfrac{kl_a}{2})\sin(\tfrac{kl_a}{2})-1\right)-e^{-\frac{1}{2}kl}\left(e^{kl_a}+2\cos(\tfrac{kl_a}{2})\sin(\tfrac{kl_a}{2})-1\right)\Big] \\
& +2\sin(\tfrac{kl}{2})\left(\cos^2(\tfrac{kl_a}{2})-1\right)\left(e^{\frac{1}{2}kl}+e^{-\frac{1}{2}kl}\right)\Bigg]
\end{aligned}
$$

$$
\frac{y_r}{u_r} = \frac{C_3}{2EIk\cos(\frac{kl}{2})\left(e^{\frac{1}{2}kl}+e^{-\frac{1}{2}kl}\right)} \tag{A.8}
$$

Collocated rectangular actuator-sensor pair on a free-free beam:

$$
\begin{aligned}
C_4 = \Bigg[& \cos(\tfrac{kl}{2})\ \Big[e^{\frac{1}{2}kl}\left(e^{-kl_a}-2\cos(\tfrac{kl_a}{2})\sin(\tfrac{kl_a}{2})-2\cos^2(\tfrac{kl_a}{2})+1\right) \\
& \qquad + e^{-\frac{1}{2}kl}\left(e^{kl_a}+2\cos^2(\tfrac{kl_a}{2})-2\cos(\tfrac{kl_a}{2})\sin(\tfrac{kl_a}{2})+1\right)\Big] \\
& +\sin(\tfrac{kl}{2})\Big[e^{\frac{1}{2}kl}\left(e^{-kl_a}-2\cos(\tfrac{kl_a}{2})\sin(\tfrac{kl_a}{2})-2\cos^2(\tfrac{kl_a}{2})-3\right) \\
& \qquad + e^{-\frac{1}{2}kl}\left(-e^{kl_a}-2\cos^2(\tfrac{kl_a}{2})-2\cos(\tfrac{kl_a}{2})\sin(\tfrac{kl_a}{2})+3\right)\Big] \\
& +4\sin(\tfrac{kl_a}{2})\left(e^{-\frac{1}{2}kl_a}-e^{\frac{1}{2}kl_a}\right)\Bigg]
\end{aligned}
$$

$$\frac{y_r}{u_r} = \frac{C_4}{2EIk\left[\cos(\frac{kl}{2})\left(e^{\frac{1}{2}kl} - e^{-\frac{1}{2}kl}\right) + \sin(\frac{kl}{2})\left(e^{\frac{1}{2}kl} + e^{-\frac{1}{2}kl}\right)\right]} \tag{A.9}$$

Collocated rectangular actuator-sensor pair on a cantilevered beam:

$$\begin{aligned} C_5 =\; & 2\cos(\tfrac{kl}{2})\sin(\tfrac{kl}{2})\left[\left(2\cos^2(\tfrac{kl_a}{2}) - 1\right)\left(e^{kl} + e^{-kl}\right) - e^{kl_a} - e^{-kl_a} + 2\right] \\ & + 2\cos(\tfrac{kl_a}{2})\sin(\tfrac{kl_a}{2})\left[\left(1 - 2\cos^2(\tfrac{kl}{2})\right)\left(e^{kl} + e^{-kl}\right) - 2\right] \\ & + 2\cos^2(\tfrac{kl}{2})\left[e^{-kl}\left(1 - e^{kl_a}\right) - e^{kl}\left(1 - e^{-kl_a}\right)\right] \\ & + \left(2\cos^2(\tfrac{kl_a}{2}) - e^{-kl_a} - 3\right)\left(e^{-kl} - e^{kl}\right) + e^{-kl_a} - e^{kl_a} \end{aligned}$$

$$\frac{y_r}{u_r} = \frac{C_5}{2EIk\left[\left(2\cos^2(\frac{kl}{2}) - 1\right)\left(e^{kl} + e^{-kl}\right) + 2\right]} \tag{A.10}$$

Noncollocated rectangular actuator-sensor pair on a pinned-pinned beam, where the sensor is shorter than the actuator:

$$\begin{aligned} C_6 =\; & -2\sin(\tfrac{kl_s}{2})\left[\left(e^{\frac{1}{2}kl} + e^{-\frac{1}{2}kl}\right)\left(\sin(\tfrac{kl}{2})\sin(\tfrac{kl_a}{2}) + \cos(\tfrac{kl}{2})\cos(\tfrac{kl_a}{2})\right)\right] \\ & + \cos(\tfrac{kl}{2})\left[\left(e^{-\frac{1}{2}kl_s} - e^{\frac{1}{2}kl_s}\right)\left(e^{\frac{1}{2}kl}e^{-\frac{1}{2}kl_a} + e^{-\frac{1}{2}kl}e^{\frac{1}{2}kl_a}\right)\right] \end{aligned}$$

$$\frac{y_r}{u_r} = \frac{C_6}{2EIk\cos(\frac{kl}{2})\left(e^{\frac{1}{2}kl} + e^{-\frac{1}{2}kl}\right)} \tag{A.11}$$

When the sensor is longer than the actuator:

$$\begin{aligned} C_7 =\; & -2\sin(\tfrac{kl_a}{2})\left[\left(e^{\frac{1}{2}kl} + e^{-\frac{1}{2}kl}\right)\left(\sin(\tfrac{kl}{2})\sin(\tfrac{kl_s}{2}) + \cos(\tfrac{kl}{2})\cos(\tfrac{kl_s}{2})\right)\right] \\ & + \cos(\tfrac{kl}{2})\left[\left(e^{-\frac{1}{2}kl_a} - e^{\frac{1}{2}kl_a}\right)\left(e^{\frac{1}{2}kl}e^{-\frac{1}{2}kl_s} + e^{-\frac{1}{2}kl}e^{\frac{1}{2}kl_s}\right)\right] \end{aligned}$$

$$\frac{y_r}{u_r} = \frac{C_7}{2EIk\cos(\frac{kl}{2})\left(e^{\frac{1}{2}kl} + e^{-\frac{1}{2}kl}\right)} \tag{A.12}$$

A.3 Transfer Functions for Triangular Actuator-Sensor Pairs

Collocated triangular actuator-sensor pair on a pinned-pinned beam: -

$$
\begin{aligned}
C_8 = {} & 2\sin(\tfrac{kl}{2})\left[\left(e^{kl}+1\right)\left(2\cos(\tfrac{kl_a}{2})-1\right)+e^{kl}\cos^2(\tfrac{kl_a}{2})\right] \\
& +\cos(\tfrac{kl}{2})\left[2\sin(\tfrac{kl_a}{2})\left(\cos(\tfrac{kl_a}{2})-2\right)\left(e^{kl}+1\right)+e^{kl}\left(e^{-kl_a}-4e^{-\frac{1}{2}kl_a}+3\right)-e^{kl_a}+4e^{\frac{1}{2}kl_a}-3\right]
\end{aligned}
$$

$$
\frac{y_t}{u_t}=\frac{C_8}{2EIk^3\cos(\frac{kl}{2})\,(e^{kl}+1)} \tag{A.13}
$$

Collocated triangular actuator-sensor pair on a free-free beam:

$$
\begin{aligned}
C_9 = {} & \sin(\tfrac{kl}{2})\Big[2\cos(\tfrac{kl_a}{2})\left(\cos(\tfrac{kl_a}{2})-2\right)\left(1-e^{kl}\right) \\
& \quad +2\sin(\tfrac{kl_a}{2})\left(\cos(\tfrac{kl_a}{2})-2\right)\left(1+e^{kl}\right) \\
& \quad +e^{kl}\left(e^{-kl_a}-4e^{-\frac{1}{2}kl_a}+1\right)-e^{kl_a}+4e^{\frac{1}{2}kl_a}-1\Big] \\
& +\cos(\tfrac{kl}{2})\Big[2\cos(\tfrac{kl_a}{2})\left(\cos(\tfrac{kl_a}{2})-2\right)\left(e^{kl}+1\right) \\
& \quad +2\sin(\tfrac{kl_a}{2})\left(\cos(\tfrac{kl_a}{2})-2\right)\left(e^{kl}-1\right) \\
& \quad +e^{kl}\left(e^{-kl_a}-4e^{-\frac{1}{2}kl_a}+5\right)+e^{kl_a}-4e^{\frac{1}{2}kl_a}+5\Big] \\
& +4e^{\frac{1}{2}kl}\left(1-\cos(\tfrac{kl_a}{2})\right)\left(2-e^{-\frac{1}{2}kl_a}-e^{\frac{1}{2}kl_a}\right)
\end{aligned}
$$

$$
\frac{y_t}{u_t}=\frac{C_9}{2EIk^3\left(\cos(\frac{kl}{2})\,(e^{kl}-1)+\sin(\frac{kl}{2})\,(e^{kl}+1)\right)} \tag{A.14}
$$

Collocated triangular actuator-sensor pair on a cantilevered beam:

$$\begin{aligned} C_{10} = {} & 2\cos(\tfrac{kl}{2})\sin(\tfrac{kl}{2})\left[e^{kl}\left(4e^{\frac{1}{2}kl_a}+4e^{-\frac{1}{2}kl_a}-e^{-kl_a}-e^{kl_a}-6\right)+2\cos(\tfrac{kl_a}{2})\left(e^{2kl}+1\right)\left(2-\cos(\tfrac{kl_a}{2})\right)\right] \\ & + 2\cos(\tfrac{kl_a}{2})\sin(\tfrac{kl_a}{2})\left[\left(2\cos^2(\tfrac{kl}{2})-1\right)\left(e^{2kl}+1\right)-2e^{kl}\right] \\ & + 2\cos^2(\tfrac{kl}{2})\left[e^{2kl}\left(e^{-kl_a}-4e^{-\frac{1}{2}kl_a}-\sin(\tfrac{kl_a}{2})+3\right)-e^{kl_a}+4e^{\frac{1}{2}kl_a}-\sin(\tfrac{kl_a}{2})-3\right] \\ & + 2\cos(\tfrac{kl_a}{2})\left(2-\cos(\tfrac{kl_a}{2})\right)\left(e^{2kl}+1\right)+4\sin(\tfrac{kl_a}{2})\left(e^{2kl}-2e^{kl}+1\right) \\ & + e^{-kl}\left(4e^{\frac{1}{2}kl_a}-4e^{-\frac{1}{2}kl_a}+e^{-kl_a}-e^{kl_a}\right)+e^{2kl}\left(4e^{-\frac{1}{2}kl_a}-e^{-kl_a}-1\right)-4e^{\frac{1}{2}kl_a}+e^{kl_a}+1 \end{aligned}$$

$$\frac{y_t}{u_t} = \frac{C_{10}}{2EIk^3\left[2e^{kl}+\left(2\cos^2(\frac{kl}{2})-1\right)\left(e^{2kl}+1\right)\right]} \qquad \text{(A.15)}$$

Noncollocated triangular actuator-sensor pair on a pinned-pinned beam, where sensor is shorter than actuator:

$$\begin{aligned} C_{11} = {} & 2\sin(\tfrac{kl}{2})\left(e^{kl}+1\right)\left(1-\cos(\tfrac{kl_s}{2})\right)\left(\cos(\tfrac{kl_a}{2})-1\right) \\ & + \cos(\tfrac{kl}{2})\Big[2\left(e^{kl}+1\right)\left(\sin(\tfrac{kl_a}{2})\cos(\tfrac{kl_s}{2})-\sin(\tfrac{kl_s}{2})-\sin(\tfrac{kl_a}{2})\right) \\ & \qquad + \left(e^{-\frac{1}{2}kl_a}e^{kl}-e^{-\frac{1}{2}kl_a}\right)\left(e^{\frac{1}{2}kl_s}+e^{-\frac{1}{2}kl_s}-2\right) \\ & \qquad + 2\left(e^{kl}\left(1-e^{-\frac{1}{2}kl_s}\right)+e^{\frac{1}{2}kl_s}-1\right)\Big] \end{aligned}$$

$$\frac{y_t}{u_t} = \frac{C_{11}}{2EIk^3\cos(\frac{kl}{2})\left(e^{kl}+1\right)} \qquad \text{(A.16)}$$

When the sensor is longer than the actuator:

$$\begin{aligned} C_{12} = {} & 2\sin(\tfrac{kl}{2})\left(e^{kl}+1\right)\left(1-\cos(\tfrac{kl_s}{2})\right)\left(\cos(\tfrac{kl_a}{2})-1\right) \\ & + \cos(\tfrac{kl}{2})\Big[2\left(e^{kl}+1\right)\left(\sin(\tfrac{kl_s}{2})\cos(\tfrac{kl_a}{2})-\sin(\tfrac{kl_s}{2})-\sin(\tfrac{kl_a}{2})\right) \\ & \qquad + \left(e^{-\frac{1}{2}kl_s}e^{kl}-e^{-\frac{1}{2}kl_s}\right)\left(e^{\frac{1}{2}kl_a}+e^{-\frac{1}{2}kl_a}-2\right) \\ & \qquad + 2\left(e^{kl}\left(1-e^{-\frac{1}{2}kl_a}\right)+e^{\frac{1}{2}kl_a}-1\right)\Big] \end{aligned}$$

$$\frac{y_t}{u_t} = \frac{C_{12}}{2EIk^3\cos(\frac{kl}{2})(e^{kl}+1)} \tag{A.17}$$

A.4 Transfer Function for Quadratic Actuator-Sensor Pair

Collocated quadratic actuator-sensor pair on a pinned-pinned beam:

$$\begin{aligned}
C_{13} = {} & 2\sin(\tfrac{kl}{2})\left(e^{kl}+1\right)\left(5 - 4\cos^2(\tfrac{kl_a}{4}) - \cos^2(\tfrac{kl_a}{2}) - \sin(\tfrac{kl_a}{4})\sin(\tfrac{kl_a}{2})\right) \\
& + \cos(\tfrac{kl}{2})\Big[2\left(e^{kl}+1\right)\left(4\sin(\tfrac{kl_a}{4})\cos(\tfrac{kl_a}{4}) + \sin(\tfrac{kl_a}{2})\cos(\tfrac{kl_a}{2}) - 4\sin(\tfrac{kl_a}{4})\cos(\tfrac{kl_a}{2})\right) \\
& \quad + e^{kl}\left(5 - 2kl_a + 4e^{-\frac{3}{4}kl_a} - 4e^{-\frac{1}{4}kl_a} - 4e^{-\frac{1}{2}kl_a} - e^{-kl_a}\right) \\
& \quad - 5 - 2kl_a - 4e^{\frac{3}{4}kl_a} + 4e^{\frac{1}{4}kl_a} + 4e^{\frac{1}{2}kl_a} + e^{kl_a}\Big]
\end{aligned} \tag{A.18}$$

$$\frac{y_q}{u_q} = \frac{C_{13}}{2EIk^5\cos(\frac{kl}{2})(e^{kl}+1)} \tag{A.19}$$

A.5 Cubic Actuator to Sensor Transfer Function

Collocated cubic actuator-sensor pair on a pinned-pinned beam:

$$\begin{aligned}
C_{14} = {} & 192\sin(\tfrac{kl}{2})\Big[\left(e^{kl}+1\right)\left(\cos(\tfrac{kl_a}{2})\left(2 - \cos(\tfrac{kl_a}{2})\right) - 1\right) \\
& \quad + 4\cos(\tfrac{3kl_a}{8})\left(\cos(\tfrac{kl_a}{2}) - \cos(\tfrac{3kl_a}{8}) - 1\right) \\
& \quad + 4\cos(\tfrac{kl_a}{8})\left(2\cos(\tfrac{3kl_a}{8}) - \cos(\tfrac{kl_a}{2}) - \cos(\tfrac{kl_a}{8}) + 1\right)\Big] \\
& + \cos(\tfrac{kl}{2})\Big[192\left(e^{kl}+1\right)\Big[\sin(\tfrac{kl_a}{2})\left(\cos(\tfrac{kl_a}{2}) - 4\cos(\tfrac{3kl_a}{8}) + 4\cos(\tfrac{kl_a}{8}) - 2\right) \\
& \qquad + 4\sin(\tfrac{kl_a}{8})\left(\cos(\tfrac{kl_a}{8}) - 1\right) \\
& \qquad + 4\sin(\tfrac{3kl_a}{8})\left(\cos(\tfrac{3kl_a}{8}) - 2\cos(\tfrac{kl_a}{8}) + 1\right)\Big] \\
& \quad + 96\Big[e^{kl}\Big(e^{-kl_a} + 12e^{-\frac{3}{8}kl_a} + 4e^{-\frac{3}{4}kl_a} - 4e^{-\frac{7}{8}kl_a} + 4e^{-\frac{5}{8}kl_a} \\
& \qquad - 12e^{-\frac{1}{8}kl_a} - 4e^{-\frac{1}{4}kl_a} - 12e^{-\frac{1}{2}kl_a} + 11\Big)
\end{aligned}$$

$$-e^{kl_a}-12e^{\frac{3}{8}kl_a}-4e^{\frac{3}{4}kl_a}+4e^{\frac{7}{8}kl_a}-4e^{\frac{5}{8}kl_a}$$

$$+12e^{\frac{1}{8}kl_a}+4e^{\frac{1}{4}kl_a}+12e^{\frac{1}{2}kl_a}-11\Big]$$

$$+\ k^3 l_a^3\left(e^{kl}+1\right)\Big)\Big]$$

$$\frac{y_c}{u_c}=\frac{C_{14}}{192EIk^7\cos(\frac{kl}{2})(e^{kl}+1)} \tag{A.20}$$